Two-Color Photoionization Experiments with Ultrashort Light Pulses on Small Atomic Systems

Dissertation

zur Erlangung des Doktorgrades
an der Fakultät für Mathematik, Informatik und Naturwissenschaften
Fachbereich Physik
der Universität Hamburg

vorgelegt von

Amir Jones Rafipoor

Hamburg
2017

Gutachter der Dissertation	Dr. Michael Meyer Prof. Dr. Klaus Sengstock
Gutachter der Disputation	Dr. Michael Meyer Prof. Dr. Klaus Sengstock Prof. Dr. Markus Drescher Dr. Michael Martins Prof. Dr. Daniela Pfannkuche
Datum der Disputation	May 2017
Vorsitzende des Prüfungsausschusses	Prof. Dr. Daniela Pfannkuche
Vorsitzender des Promotionsausschusses	Prof. Dr. Wolfgang Hansen
Dekan der Fakultät für Mathematik, Informatik und Naturwissenschaften	Prof. Dr. Heinrich Graener

Abstract

The photoionization of atoms can reveal invaluable information about their underlying electronic structure and dynamics. For decades, such studies at synchrotron light sources and with optical lasers have substantially contributed to our today's knowledge of nature's fundamental building blocks. With the advent of ultrashort and ultraintense X-ray pulses generated by free-electron lasers, new fields of science such as non-linear physics, ultrafast physical chemistry as well as ultrafast bio-chemistry have evolved. This thesis is dedicated to investigations of fundamental processes in non-linear light interaction with small atomic targets in the gas phase. Especially in two-color experiments with ultrashort extreme ultraviolet (XUV) and near infrared (NIR) laser pulses, the structure and dynamics of electrons can be studied in an unprecedented way by obtaining their spectra by means of different kinds of spectrometers. In particular the study of the electrons' angular distributions and their dependences on the intensity of a dressing laser field opens the door for e.g. polarization dependent partial wave analysis studies. In the laboratory these type of experiments can be realized using XUV pulses generated by the process of high order harmonic generation (HHG). Such a set-up has been built up during this thesis. Using the world's first circularly polarized, ultraintense FEL, FERMI in Italy, oriented ion-electron pairs were created and probed by superimposed NIR pulses of co- or counter-rotating helicities. Using this method, the obtained circular dichroism was used to determine the actual degree of circular polarization at the experimental endstation LDM at FERMI. Further aspects of the underlying light-matter interaction with particular interest in the dependence of the circular dichroism on the NIR intensity are discussed in this thesis. As concluding chapter, a two-color multi-photon ionization experiment on the intensity dependence of a dichroic AC Stark shift will be presented.

Kurzfassung

Die Photoionisation von Atomen kann einzigartige Informationen über die elektronische Struktur und die Dynamik der Elektronen bereitstellen. Seit Jahrzehnten tragen derartige Studien mit Synchrotronstrahlungsquellen und optischen Lasern substanziell zu unserem Wissen über die fundamentalen Bausteine der Natur bei. Durch die kürzlich entstandene Verfügbarkeit von ultraintensiven und ultrakurzen Röntgenpulsen von Freie-Elektronen Lasern (FELs), haben sich neue Wissenschaftsfelder wie z.B. die Physik von nicht-linearen Prozessen sowie ultraschnelle Phänomene der physikalischen Chemie und der Biophysik entwickelt. Diese Doktorarbeit ist der Untersuchung von fundamentalen Prozessen in nicht-linearer Wechselwirkung von Licht mit Atomen in der Gasphase gewidmet. Speziell mit einer Zwei-Farben-Kombination aus ultraschnellen FEL-Pulsen im extrem-ultraviolett (XUV) und Laserpulsen im nahen Infrarotbereich (NIR), können Struktur und Dynamik von Elektronensystemen anhand von Spektralanalyse mit verschiedenen Spektrometertypen in einer neuartigen Weise studiert werden. Besonders die Untersuchung von Elektronenwinkelverteilungen und ihre Abhängigkeit von der Intensität des optischen Lasers öffnen z.B. neue Zugänge für eine polarisationsabhängige Erforschung der Partialwellenanalyse. Als laborbasierte Experimente können solche Untersuchungen mit ultrakurzen XUV-Pulsen durch die Generierung von hohen Harmonischen von optischer Laserstrahlung (HHG) realisiert werden. Eine derartige XUV-Laserquelle wurde im Rahmen dieser Arbeit aufgebaut. Der Großteil der Experimente wurde jedoch mit FERMI, dem weltweit ersten FEL, der zirkularpolarisierte Lichtpulse mit großer Intensität bereitstellen kann, durchgeführt. Mit dieser Strahlung wurden orientierte Ionen-Elektronenpaare erzeugen, die durch gleiche und entgegengesetzte Helizitäten eines überlappenden NIR Lasers untersucht werden können. Mit dieser Methode der Bestimmung des resultierenden Zirkulardichroismus wurde erstmalig der tatsächliche Polarisationsgrad von FERMI an der Experimentierstation LDM (Low Density Matter) gemessen. Weitere Aspekte der zirkulardichroischen Licht-Materie-Wechselwirkung im Hinblick auf resonante und nicht-resonante NIR-Intensitätsabhängigkeit werden im Rahmen dieser Arbeit diskutiert. Im abschließenden Kapitel wird in diesem Zusammenhang ein Experiment zu einer Zwei-Farben Multi-Photonen Ionisation und deren Intensitätsabhängigkeit bezüglich einer dichroischen AC-Stark Energieverschiebung in Heliumionen präsentiert.

List of Figures

1.1 Wiggler . . . 5
1.2 Micro-Bunching . . . 7
1.3 HGHG and SASE FEL . . . 8
1.4 Peak Brilliance . . . 9
1.5 Time-Resolved Pump-Probe . . . 10
1.6 Two-Color Experiments . . . 13

2.1 Single-Photon Ionization . . . 17
2.2 Photoionization Categories . . . 19
2.3 Multi-Photon Ionization . . . 21
2.4 Anistropy Parametrs in Photoionization with Linearly Polarized Light 23
2.5 Anistropy Parametrs in Photoionization with Circularly Polarized Light . . . 24
2.6 Angular Distribution of Photoelectrons $\beta_2^{\nu\nu'} = 2$ in Circularly Polarized Light . . . 25
2.7 Dichroism . . . 27
2.8 Two-Color ATI of Helium with Circularly Polarized Beams . . . 31

3.1 HHG Setup at SQS Laser Lab . . . 36
3.2 Gascell . . . 38
3.3 Mirror Chamber . . . 39
3.4 Experimental Chamber . . . 40
3.5 TOF Spectrometer . . . 41
3.6 VMI Spectrometer . . . 44
3.7 Delay Line PSD . . . 45
3.8 Three-Step Model . . . 47
3.9 HHG Spectrum . . . 51
3.10 Lens-Position Scan . . . 52
3.11 Gascell-Pressure Scan . . . 54
3.12 Laser-Intensity Scan . . . 55

4.1 Sideband . . . 60
4.2 Schematic of LDM Instrument . . . 62
4.3 Cross Correlation . . . 64
4.4 Two-Color Ionization of He . . . 66

4.5 Circular Dichroism in Sidebands 68

5.1 Single-Photon Ionization of He 70
5.2 VMI Raw Image 71
5.3 Formation of Sidebands 72
5.4 Two-Color ATI in He 73
5.5 VMI Signal Overlap 74
5.6 PAD in Low Intensity NIR Field 75
5.7 Sidebands in High Intensity NIR 77
5.8 Angle Resolved Yield of Sidebands 78
5.9 NIR Intensity Dependence of β_2 and β_4 80
5.10 CDAD in Low Intensity NIR 81
5.11 CDAD in Strong NIR Field 82

6.1 Sequential Ionization of He 86
6.2 He^+ Photoelectron Spectrum for Co- and Counter-Rotating XUV and NIR 89
6.3 He^+ PAD for Co- and Counter-Rotating XUV and NIR 90
6.4 Intensity Dependence of CD 91
6.5 Population of $He^+(1s)$ for Co- and Counter-Rotating XUV and NIR 92
6.6 Intensity Dependence of Hydrogen Ionization Probability 95

List of Tables

3.1 Cutoff 50

5.1 β-Parameter in Low Intensity NIR 76
5.2 β-Parameter in High Intensity NIR 79

Contents

1 Introduction **1**
- 1.1 Optical Laser Based Short Wavelength Radiation . . . 2
- 1.2 Accelerator Based Short Wavelength Radiation . . . 3
  - 1.2.1 Synchrotron Radiation . . . 3
  - 1.2.2 Free-Electron Lasers . . . 6
- 1.3 Time-Resolved Studies . . . 9
- 1.4 Non-Linear Studies . . . 11
  - 1.4.1 Non-Linear Processes in Single-Color Studies . . . 12
  - 1.4.2 Non-Linear Processes in Two-Color Studies . . . 12
- 1.5 Outline . . . 14

2 Theoretical Background **15**
- 2.1 Photoionization Processes in Atoms . . . 16
  - 2.1.1 Single-Photon Ionization . . . 16
  - 2.1.2 Multi-Photon Ionization . . . 18
- 2.2 Angular Distribution of Photoelectrons . . . 22
  - 2.2.1 Photoelectron Angular Distribution in a Linearly Polarized Light Field . . . 22
  - 2.2.2 Angular Distribution in a Circularly Polarized Light Field . 24
- 2.3 Dichroism in Photoionization . . . 26
  - 2.3.1 Circular Dichroism in Photoelectron Spectroscopy . . . 27
- 2.4 Time Dependent Strong Field Approximation . . . 29
- 2.5 The Perturbation Theory Approach in Sideband Formation . . . 30
- 2.6 Summary . . . 33

3 Experiments with High Order Harmonics **35**
- 3.1 Experimental Setup at the XFEL Laser Lab . . . 36
  - 3.1.1 Time-of-Flight Spectrometer . . . 40
  - 3.1.2 Velocity Map Imaging Spectrometer . . . 43
- 3.2 High Harmonic Generation . . . 46
  - 3.2.1 Phase Matching and Coherence in HHG . . . 48
- 3.3 Characterization of HHG . . . 49
- 3.4 Application and Outlook . . . 56

4 Two-Color Two-Photon Experiments as a Tool for Characterizing FEL Pulses 59
4.1 Experimental Setup at the LDM Beamline 61
4.1.1 Spectrometer and Data Acquisition 62
4.2 Temporal Overlap and Measurement of the FEL Pulse Duration . . 63
4.3 Characterization of the Polarization State of FERMI 65

5 Intensity Dependence in the Two-Color Photoionization of Helium Atoms 69
5.1 Data Analysis 71
5.2 PAD in Photoionization of Dressed He Atoms in Low Intensity NIR Fields 72
5.3 PAD in the Photoionization of Dressed He Atoms in High Intensity NIR Fields 77
5.4 NIR Intensity Dependence of PADs 79
5.5 Circular Dichroism at Different Intensities 80
5.5.1 Circular Dichroism in Low Intensity NIR Fields 81
5.5.2 Circular Dichroism in High Intensity NIR Fields 82
5.6 Summary 83

6 Multi-photon Ionization of Oriented Helium Ions with Polarization Control 85
6.1 Excitation Scheme 86
6.2 NIR Intensity Dependence of the Circular Dichroism 89
6.2.1 Circular Dichroism in the NIR Low Intensity Regime 90
6.2.2 Intensity Dependent Circular Dichroism 91
6.3 Conclusion and Discussion 93
6.3.1 Outlook 94

7 Summary and Outlook 97

List of Abbreviations 101

Bibliography 101

List of Publications 118

Acknowledgments 119

CHAPTER 1

Introduction

Human curiosity, to gain a detailed understanding of the relationship between various phenomena in nature on the one hand and the growing thirst of technological development in various areas of society on the other hand, provide a strong base for fundamental investigations of basic elements in all disciplines of science. The desire of producing novel medicines for still incurable diseases or designing new materials with special properties such as low mass, high mechanical- and heat-resistance and high electrical conductivity at the same time, as well as gaining energy from photosynthesis based processes, makes people think about a solution. Several of these areas have substantial overlap with the need to find a way to control chemical reaction as well as the process of formation and fragmentation of different materials, which has to be studied on a fundamental level. In general, one of the most effective methods for the fundamental study of different materials, is photon-matter interaction, which enables scientists to investigate material properties [1, 2, 3, 4]. The photoeffect explained by Einstein in 1905 was one of the first milestones of this kind [5].

For a deep understanding of the formation of materials and the interaction of molecules and atoms, it is necessary to investigate the electron dynamics inside atoms. In order to study these dynamics, the target has ideally to be investigated in an isolated state to avoid undesired external perturbations or in a state, where the perturbation can be controlled. However, an unperturbed small atom will typically stay in the electronic ground state and cannot be easily studied without external excitations. Therefore, the target has to be brought into a non-equilibrium state, where the dynamics in the electronic processes can be studied. This can be realized in a controlled photon-matter interaction, e.g. photoabsorption, photoexcitation and photoionization, such that all external impacts can be governed.

In general, the electron dynamics in different photon-matter experiments can be monitored by obtaining the products of the photoionization process, namely ions and photoelectrons. The ions and photoelectrons can be detected by means of spectrometers, e.g. time of flight spectrometers (TOF) or velocity map imaging spectrometers (VMI). There are several different kind of spectrometers. However, in this thesis TOF and VMI spectrometer have been used to detect the photoelectrons produced in the photoionization processes. A TOF spectrometer enables the

detection of the relative photoelectron arrival time and therefore, obtaining their kinetic energy. However, the angle of acceptance of this detector is typically limited in order to ensure the capability to employ arrays of multiple of these spectrometers for angle resolving studies. Their advantage is the high energy resolution over a relatively large energy window as well as the possibility to record electrons of a total kinetic energy of thousands of eV. In case of VMI spectrometers, the angle of acceptance is practically 4π, which enables the detection of photoelectrons ejected in all different directions. The most important advantage of this kind of spectrometer is the intrinsic ability of detecting the angular distribution of photoelectrons by means of a position sensitive detector despite the full solid acceptance angle. These spectrometers are described in more details in chapter 3.

Photoionization and photoexcitation with one or more photons as well as the connected decay processes in the electron structure of atoms gives access to monitor electron dynamics inside atoms. The timescale of the photoionization process itself is still one of the big challenges to directly observe since it is theoretically predicted to happen on the order of attoseconds, i.e. at the frontier of today's capabilities. However, many interesting electronic, atomic and molecular dynamics happen on the timescale of femtoseconds. In order to directly resolve them in a photon- atom interaction, it is imperative that the light pulses are at least on the same temporal order as the processes themselves. On the other hand, for the investigation of dynamics of inner-shell electrons (high binding energies), high photon energies in the range of vacuum ultraviolet (VUV), extreme ultraviolet (XUV), soft- and hard X-rays are needed. Therefore, in order to perform experiments for the investigation of inner-shell electron dynamics, light sources with ultrashort pulses (fs scale) and short wavelengths (XUV, X-ray) are required. The light sources, which are able to provide radiation with these properties, can be categorized in optical laser and accelerator based short wavelength radiation sources.

1.1 Optical Laser Based Short Wavelength Radiation

Short light pulses on the fs-time scale can be provided by optical lasers. However, in order to enter photon energy ranges of and beyond the VUV regime in fs-pulses, one possibility is the high order harmonics generation (HHG) of an optical laser. This can be achieved by focusing the short laser pulses into e.g. a gas medium. The interaction of the laser pulse traveling through the gas medium can change the Coulomb potential of the atoms so that electrons can be ejected in a tunnel ionization process. The released electrons in the strong electric field are accelerated and their kinetic energy will increase. Since the electric field of the light pulse is changing by traveling through the gas medium, the change of the sign of the electric field can accelerate the freed electrons back towards their parent ions. Thereby, the electrons will "recombine" with the ions so that they are trapped again in the Coulomb potential of the atom and their exceeded kinetic energy (compared to the ionization potential) will be released by emission of a short wavelength photon.

This process can be explained by the so called "Three-Step Model", which will be described in more details in chapter 3. There are several parameters playing an important role for the efficiency of the HHG process, e.g. phase-matching, laser intensity and the gas density, which are also further discussed in chapter 3.

The photon energy of the HHG radiation can be above 100 eV and in some cases even in the order of keV [6], which is in the XUV and X-ray range and sufficient to excite several inner-shell electrons in atomic targets. Moreover, the pulse duration of the HHG radiation can be in the order of attoseconds [7, 8, 9], which makes them suited for time-resolved investigation of fast electron dynamics in e.g. atoms and molecules [10]. However, for dilute targets, the intensity of the HHG is insufficient to provide enough photons within a single pulse to perform statistically valid spectroscopic experiments within the single pulse. Among others, this challenge can be addressed by using ultrashort and ultrabright pulses with photon energies from the VUV to hard X-rays from free-electron lasers (FELs). In the context of this thesis, the construction and the generation of higher harmonics of a femtosecond laser, is described in chapter 3, whereas chapters 4-6 are dedicated to non-linear two-color investigations with optical lasers and FEL radiation.

1.2 Accelerator Based Short Wavelength Radiation

Accelerator based radiation sources can provide light pulses with a wide range of wavelengths from the THz regime to the hard X-ray region. With the invention of large scale facilities, e.g. synchrotrons and FELs, these novel radiation sources for short-wavelength radiation have provided the possibility for a broad study of materials. Since the bulk of the work presented in this thesis has been performed at FELs, it is worth giving a short historical overview over the generation of such light sources.

1.2.1 Synchrotron Radiation

Synchrotron radiation is emitted by accelerated charged particles that typically move at relativistic speed. This phenomenon can be observed e.g. by bending the trajectory of a high kinetic energy electron beam by means of a magnetic field. This principle is the basis for many of today's synchrotron radiation sources that are operated for the investigation of matter with light.

In principle, a synchrotron light source consists of an electron gun, where electrons are produced in a photocathod source. The electrons are accelerated in a linear accelerator to energies of several MeVs. Subsequently, the electrons are further accelerated in a booster ring and finally they enter a storage ring, where they preserve the energy they have acquired during their preceding acceleration. The energy losses due to the radiation are frequently compensated. Many electrons are focused together in very dense 'bunches' by means of horizontal and vertical magnetic fields with respect to the beam propagation and electron bunches are formed.

In the first generation of synchrotron light sources, the radiation is produced just by the bending magnets that keep the electrons on their trajectories. Whenever the electron trajectory is bent due to the Lorenz force, part of the kinetic energy of the electron will be emitted as photons. In the case of electrons at relativistic speed, the emission direction of the light is strongly directed towards the propagation direction. Light created in this way has an extremely broad bandwidth from the visible to hard X-rays. Since the total intensity is distributed over all these frequencies, the number of photons at a certain energy within one pulse is comparably small. The first report for the observation of synchrotron light was published by F. R. Elder et. al. in 1947 [11].

In the second generation of synchrotron radiation, the electron bunches enter a wiggler, which consists of a periodic structure of magnets with alternating poles. Here, the electrons 'wiggle' through the magnetic chicane and at each turning point (acceleration) they radiate, similar to a bending magnet. The number of periods n of the wiggler's magnet structure therefore provides n-times the intensity of a bending magnet. Obviously, the electrons need to be close to the speed of light to be able to almost stack the individual pulses on top of each other and to produce one single light pulse with enhanced intensity rather than a sequence of pulses.

In the third generation of synchrotrons the wigglers have been further developed into so called undulators. Undulators basically consists of a similar periodic structure of magnets as the wigglers, which can be longer than that of the wigglers. The pulses from an undulator have much narrower bandwidth in comparison to the radiation of the wigglers due to the narrower trajectory of the electrons through the magnetic periods and a resulting interference between the electron bunch and the emitted light pulses. A classification of the underlying process and therefore the differentiation between wiggler and undulator can be done by the following equation [12, 13, 14]:

$$K = \frac{eB_u\lambda_u}{2\pi m_e c} = 0.934 \times B_u[T] \times \lambda_u[cm], \tag{1.1}$$

where e and m_e are the charge and mass of the electron, respectively, c is the speed of light and B_u is the strength of the magnetic field in the undulator (or wiggler). λ_u is the so called undulator period, which is the distance between two equal poles of magnets and is typically smaller than the period of a wiggler (see Fig.1.1)[12]. In case of undulators, $K \leq 1$ and the amplitude of the oscillating movement of the electrons is small and the emitted photons can be in resonance (in phase) and therefore, show an interference pattern, which leads to a narrow bandwidth of the radiation. However, in case of wigglers $K \geq 1$, the amplitude of the oscillating movement of the electrons is larger and leads to a broader bandwidth of the radiation.

Here, photons with odd harmonic frequencies are emitted on-axis with the propagation axis of the electron bunches, whereas, the photons with even harmonics of the central beam frequency are dominantly emitted off-axis [16]. The wavelength

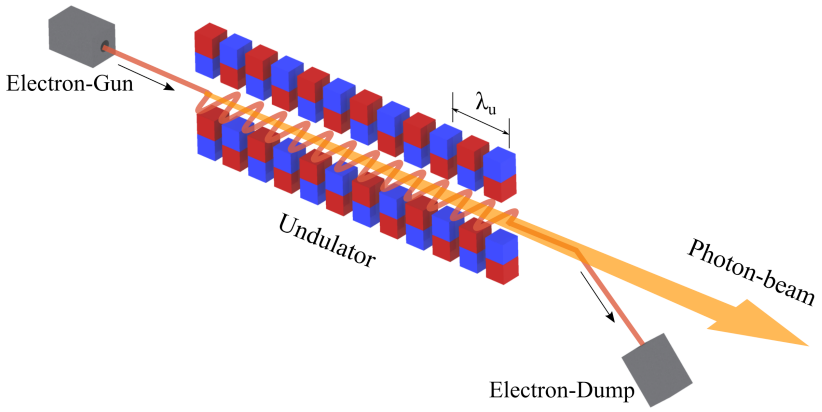

Figure 1.1: A schematic representation of photon generation in an undulator [15].

of the n^{th} harmonic emitted in the undulator can be calculated from the following equation [12, 13]:

$$\lambda_n = \frac{\lambda_u}{2n\gamma^2}\left(1 + \frac{K^2}{2} + \gamma^2\theta\right), \tag{1.2}$$

where θ is the emission angle of photons relative to the undulator axis and γ is the Lorenz factor, which is defined in the following equation [12]:

$$\gamma = \frac{E}{m_e c^2}, \tag{1.3}$$

where E is the energy of the electrons. For a collimated radiation along the undulator axis ($\theta = 0$) equation 1.2 for the first harmonic can be simplified as the following:

$$\lambda = \frac{\lambda_u}{2\gamma^2}\left(1 + \frac{K^2}{2}\right). \tag{1.4}$$

When an electron bunch moving with speed close to that of light enters an undulator with N magnetic periods, it will start to oscillate transversely and emit a train of overlapping light pulses on its pathway. The produced pulse train has a finite duration and the frequency distribution in the pulse train is proportional to $1/N$ [14]. The monochromaticity of the undulator radiation is inversely proportional to $1/nN$, where n is the harmonic order of the radiation. Therefore, for a certain λ_u, the longer the undulator, the higher the monochromaticity of the radiation [14].

1.2.2 Free-Electron Lasers

The next generation of XUV and X-ray sources is represented by free-electron lasers (FEL). Here, the production of light pulses is also based on undulator radiation. The physical process, which governs the function of most FELs is known as Self-Amplified Spontaneous Emission (SASE). Comparable to the undulator scheme presented in the previous section, the accelerated electron bunches moving through the undulator are emitting electromagnetic waves. Each electron in the bunch is not only wiggling due to the alternating magnetic field of the undulator, but also interacting with the emitted electromagnetic waves of other electrons in the bunch. This interaction over many cycles (more than needed for third generation synchrotron radiation) eventually leads to the spatial modulation of the electron density in the bunch with a period equal to the wavelength of the emitted electromagnetic wave. This effect is known as micro-bunching. This process amplifies as the electron bunches move through the undulators and the pulse energy of the radiation increases exponentially until this process is saturated. Figure 1.2 shows the increase of the pulse energy versus the travel way in the undulator at FLASH-FEL in DESY, Hamburg Germany. Here, the length of the undulator is 27 m. In order to generate radiation in the hard X-ray regime the electron energy needs to be substantially higher and the length of the undulator can be more than 100 m.

From equations 1.3 and 1.4, the photon energy of the FEL radiation is related to the magnetic field strength in the undulator and the energy of the electrons moving through the undulator. The photon energy of the resulting radiation can be controlled by the energy of the electron beam and in case of varibale gap undulators also by adjusting the magnetic field.

In the SASE process, the interaction of the emitted photons with other electrons within the same bunch leads to a radiation pulse in which the photons are in phase and therefore, transversely coherent. However, the phase and energy of the photons emitted from different parts of the bunch or even different bunches can be very different. This leads to a relatively poor longitudinal coherence and a different photon spectrum for each pulse. Here, the frequency and intensity distribution changes from shot to shot.

In order to overcome this stochastic effect, it is possible to use an external strong laser field to modulate the electron density in the undulator, so that all electron bunches are interacting with the same laser beam. This can be realized by different seeding techniques. One method is to modulate the electron bunches with a laser beam in a wiggler and afterwards the electron bunches enter an undulator, which can be shorter than in a case of the SASE. This method is known as enhanced-SASE [18].

Another technique, is the High-Gain Harmonic-Generation (HGHG). In this method the high harmonics of a fundamental laser beam are used to modulate the electron bunches in a wiggler (Modulator). After going through the wiggler the electron bunches travel through two bending magnets (dispersive section), where the density modulation is enhanced. Subsequently the electron bunches enter an

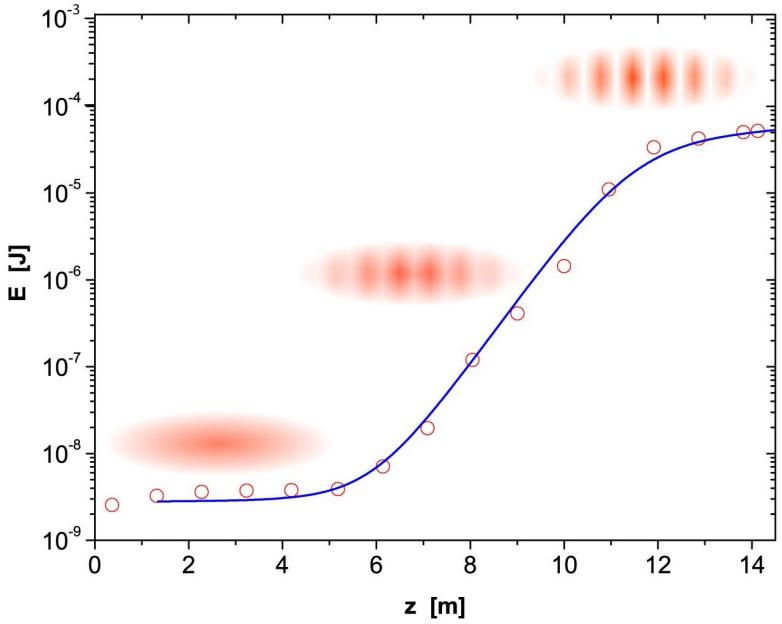

Figure 1.2: The exponential growth of the FEL pulse energy E as a function of the length z traveled in the undulator. The data (open red circles) were obtained at the first stage of the SASE FEL at DESY, the electron energy was 245 MeV. The solid curve shows the theoretical prediction. The progress of micro-bunching is indicated schematically. Laser saturation sets in for z$\geq$ 12 m. Here the micro-bunches are fully developed and no further increase in laser power can be expected. The figure and caption are taken from [17].

undulator (radiator) and start to emit short wavelength FEL radiation [19, 20]. The spectrum of the FEL radiation in this case is more intense in the fundamental mode and is narrow as all the spectral intensity is ideally put into one mode and it's harmonics [21]. In the HGHG method, the frequency and intensity distribution from shot to shot is very similar. This technique has been used for example at FERMI (FEL-1) at ELETTRA in Trieste, Italy that is the primary light source for the experiments presented in this thesis. Figure 1.3 shows a schematic representation of HGHG seeded FEL and SASE FEL.

There are several synchrotron and few FEL radiation sources around the world, which can provide light with a high spectral brightness and highly polarized short pulses in the XUV and X-ray region. These properties can be represented by the spectral brightness of the radiation, which is defined as the number of photons per unit time, per unit source area (flux, F), per unit solid angle ($d\Omega$) inside a

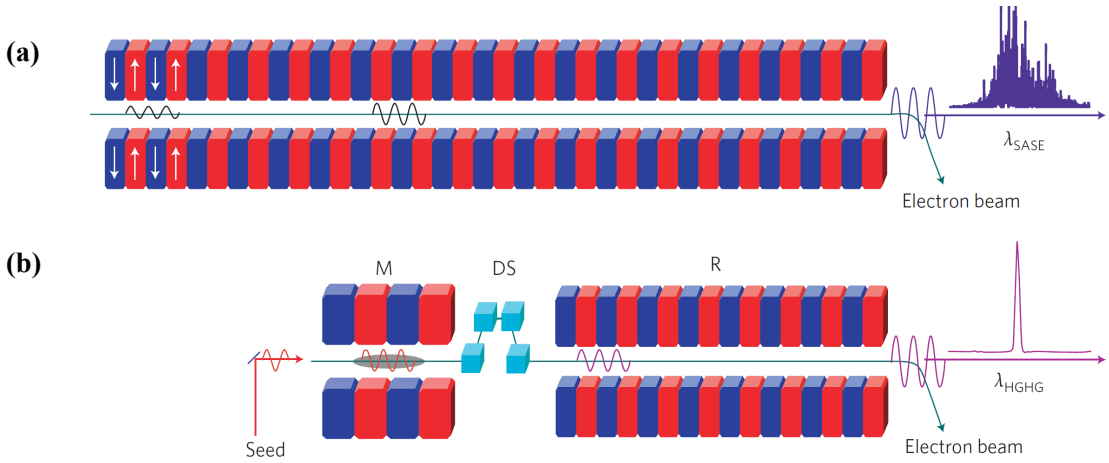

Figure 1.3: (a) SASE FEL, with poor temporal coherence. (b) HGHG FEL, showing full temporal coherence with limited harmonic number ($n \approx 10$) for a single stage. M, modulator; DS, dispersive section; R, radiator. The figure and caption are taken from [20].

bandwidth of 0.1% and is called the Brilliance:

$$Brilliance = \frac{d^2F}{d\omega d\Omega}, \tag{1.5}$$

and has the unit [photon/s/mm^2/mrad/0.1%BW]. The brilliance of different radiation sources are compared in figure 1.4. The highest brilliance of the radiation is anticipated to be provided soon at the European XFEL at Schenefeld, Germany. This FEL will provide radiation with a brilliance up to the order of 10^{33}. The electrons are accelerated to an energy of 17.5 GeV. The light pulses are radiated with a repetition rate of 27000 and the wavelength can be tuned between 0.05 to 4.7 nm [22].

In many experiments, especially in the field of bio-chemistry [24] and material sciences such as magnetization studies [25] as well as studying electron dynamics in atomic and molecular systems [26], the polarization of the incident light can play a significant role in the investigations. In this regard, circularly polarized FEL radiation could revolutionize these kind of studies. The FERMI FEL in Trieste, Italy, is the first FEL providing radiation with different polarizations, which can be set between linear horizontal, linear vertical, circular left, circular right and elliptical polarization. This possibility was enabled by APPLE type undulators [27]. The periodic set of the quadrupole magnets in this undulator has been designed to force the electrons to move in a spiral path. Therefore, the total polarization of all emitted photons can be circular. Recently, the LCLS FEL Stanford, USA, has also established the ability to provide circularly polarized light, which has been enabled

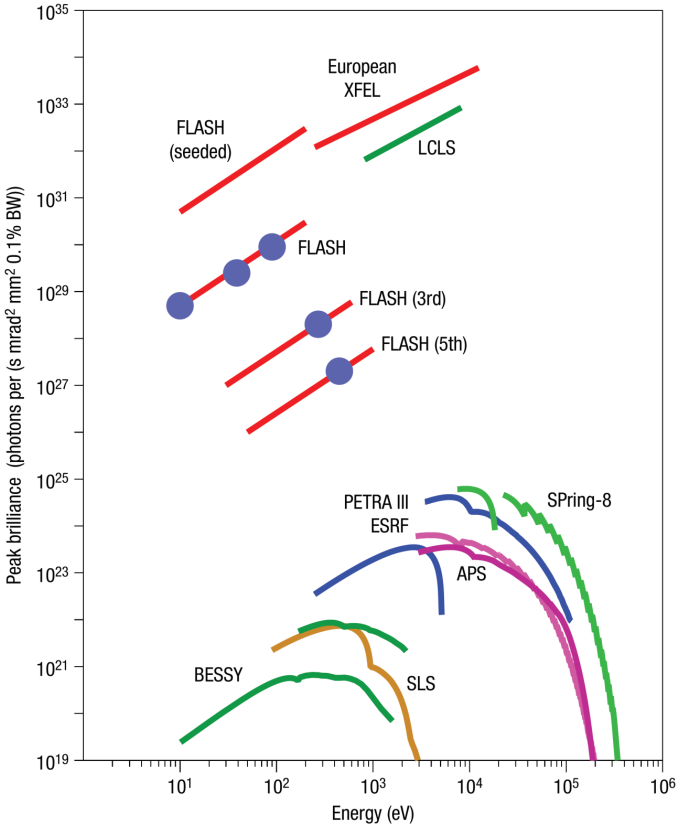

Figure 1.4: Peak brilliance of X-ray FELs in comparison with third-generation synchrotron-radiation light sources. Blue spots show experimental performance of the FLASH FEL at DESY at the fundamental, 3rd and 5th harmonics [23].

by an DELTA type of undulator [28, 29].

1.3 Time-Resolved Studies

One of the main advantages of the sources discussed above is the short pulse duration, which enables the time-resolved analysis of various processes. Time-resolved spectroscopy is an experimental method to study ultrafast electron dynamics in different targets, e.g. atoms and molecules. As one example, the decay process of electrons is investigated in these kinds of experiments, since one could basically track the temporal evolution of electron dynamics and correlations within different chemical interactions of matter as well as in photon-matter interactions.

In order to investigate fast decay processes of e.g. an atomic target, an inner-shell electron of the atom can be transferred (pumped) to a highly excited state by the absorption of a short wavelength photon (e.g. XUV), where the electron could

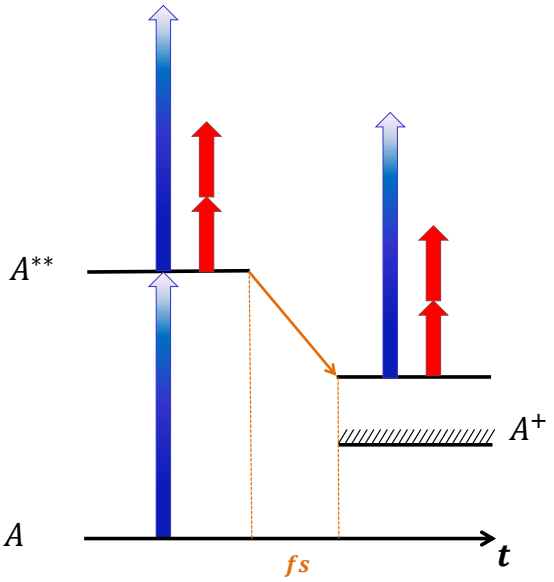

Figure 1.5: Schematic representation of a time-resolved experiment with femtosecond radiation pulses. An inner-shell electron of an atom (A) is pumped to a highly excited state by the absorption of an XUV photon (blue arrow). Here, the electron can be probed either directly (0 time delay) or after a fast decay (fs) into a final state. This can be done with a photon of the same wavelength (XUV) or photons of an optical femtosecond laser pulse (red arrows).

decay within a femtosecond time scale to a lower energy state. In an ideal case, the excited or the final state of the electron can be probed by the absorption of a photon of the same energy or a photon (or more than one) with a different energy, e.g. in the optical region (see Fig.1.5). Time-resolved pump-probe experiments [30, 31] can therefore be performed with two pulses of the same short wavelength radiation source (single-color) or with XUV and e.g. optical laser pulses (two-color) [32, 33].

In order to resolve the ultrafast dynamics of inner-shell electrons in an interaction with light, it is often beneficial to irradiate the target with femtosecond or even attosecond pulses, which have a photon energy comparable to the electron binding energy. These kinds of pulses can be provided by HHG and FEL sources. The advantage of HHG sources is on one hand the ability to provide attosecond pulses with photon energies in the XUV - X-ray region and on the other hand they can be set up in as a tabletop laser system in a laboratory. However, the intensity (photon/pulse/s) of HHG sources is limited in comparison to the FEL sources. Free-electron laser sources can provide short and radiation pulses (in fs scale) with a high number of photons per pulse, which is significant for achieving a high efficiency in different interactions. In this light, the highly intense FEL pulses enable the

study of non-linear processes in different targets.

For time-resolved pump-probe investigations of electron dynamics in atomic and molecular targets, XUV sources are often used in combination with femtosecond optical laser pulses. Thereby, in order to temporally track a certain electron transition or decay process, the time delay between the arrival of the two pulses (XUV and laser) has to be adjusted to a certain value (e.g. in femtosecond scale), which is depending on the investigated fast electronic process. This is done by changing the length of the travel way of the optical laser pulse. The studies performed within the context of this thesis are only implicitly related to fully exploring the temporal resolution, however, similar techniques have been used to find and to optimize the temporal overlap of XUV and optical laser pulses in sub-picosecond timescales (see chapters 4, 5 and 6).

1.4 Non-Linear Studies

Non-linear processes in light-matter interaction provide the opportunity to discover new phenomena in the electron dynamic of atomic and molecular species in a highly intense radiation field, which do not appear in low intensity regimes. The study of unresolved aspects of collective electronic behavior in the $4d$ dipole resonance of Xenon atoms in a two-photon ionization processes in an intense XUV field [34], is one of the examples for non-linear investigations in the electronic structure of atoms.

The invention of FELs, has opened a new opportunity for experimental investigation of non-linear processes [35], since these light sources can provide an extremely high number of photons within sub-picosecond light pulses and photon energies covering the VUV to hard X-ray region. These light sources, especially in the XUV regime, are therefore of utmost importance in the investigation of non-linear processes especially, in the interaction of inner-shell electrons of atomic systems. These studies can be performed in the context of different kinds of multi-photon processes, e.g. multi-photon excitation, multi-photon ionization, sequential ionization [36] and direct double ionization .

In general, non-linear processes in atomic photoionization appear by the simultaneous absorption of two or more photons. This kind of process was for the first time discussed in form of two-photon absorption in the theoretical studies of Goeppert-Mayer in 1931 [37] and observed in experiments with optical lasers [38]. Multi-photon processes for the investigation of non-linear phenomena can be performed with photons from light sources with the same or different wavelengths, e.g. a combination of HHG and optical laser pulses or FEL pulses and optical laser pulses [39, 40, 41]. Multi-photon processes can occur on fs time scales, therefore, light pulses with durations in the fs-order or even attosecond time scale are used in these kind of investigations [35].

1.4.1 Non-Linear Processes in Single-Color Studies

The investigation of non-linear processes in single-color experiments with atomic or molecular targets can be performed by XUV light sources, e.g. FELs. These radiation sources allow the access to the inner-shell electrons of the target and therefore, the study of Auger-decay processes. Single-color studies of non-linear processes can be realized for example by two-photon core-resonance processes, where an inner-shell electron is transferred to an excited state, which is unaccessible by a one-photon excitation, or even ejected (direct ionization) from the atom by absorbing two XUV photons simultaneously [42, 43]. These kind of studies can be valuable, in order to test the theoretical models for the multi-photon ionization in the short wavelength regime.

1.4.2 Non-Linear Processes in Two-Color Studies

The study of non-linear processes in the photon-matter interaction with two light sources of different wavelengths enables the exploration of various aspects of interactions [32, 33].

Especially regarding the case of single shot investigations, FEL sources can provide ultraintense, short wavelength light pulses with short duration in the femtosecond time scale, which can be tuned over a large spectral range. The access to the inner-shell electrons in an atomic system with XUV pulses of FEL sources on one hand and the control and manipulation as well as characterization of the initial and final states of the target by optical laser pulses on the other hand, opens the great opportunity of studying non-linear processes in two-color experiments. Furthermore, the short pulse duration of both XUV and optical laser radiation enables time-resolved investigations on the time scale of femtoseconds [40]. Thereby, an excellent temporal and spatial overlap of the XUV and optical pulses is highly important however, challenging to wield.

Figure 1.6 shows different excitation schemes for two-color experiments. The temporal and spatial overlap between the XUV radiation and optical laser pulses play an important role. Here, (a) shows a situation where the continuum state in the above-threshold ionization of the target atom can be modified by the dressing optical field so that sidebands can be formed in the photoelectron spectrum. This case is especially important, since on one hand it can enable the study of particular non-linear photoionization processes, and on the other hand, this kind of process can be utilized for the characterization of the FEL pulses (see [40] and references therein). The process (b) in figure 1.6, represents induced coupling between two high-lying resonant autoionization states with the optical laser [40]. Figure 1.6.c represents the case of a temporal delay between the XUV and optical laser pulses, which enables to determine possible intermediate states in the relaxation process or a particular final state can be characterized as shown in 1.6.d [40]. The content of this thesis is concentrated on the two-color experiments of the cases (a) and (c) in figure 1.6, which are discussed in the chapters 4, 5 and 6 of this thesis.

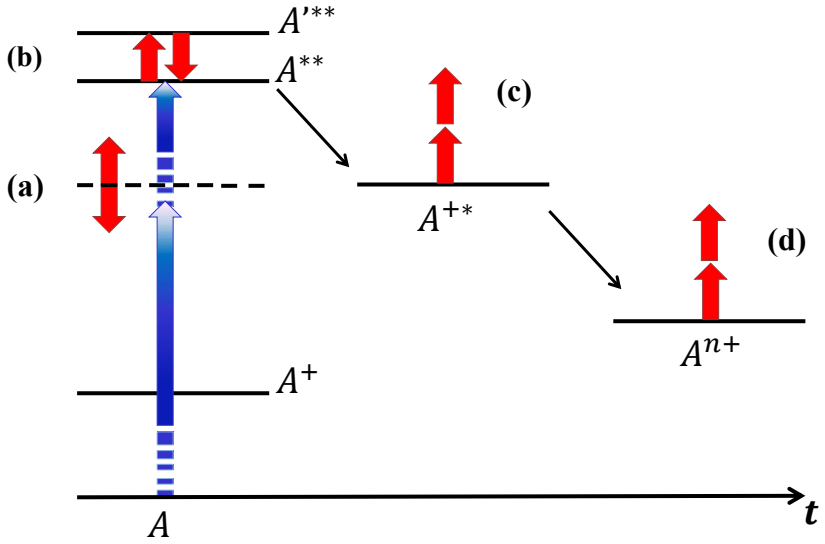

Figure 1.6: Schematic representation of typical two-color excitation schemes in atoms and molecules: (a) Two-color above-threshold ionization (ATI), (b) laser coupling of autoionization states, and time-resolved studies of (c) intermediate and (d) final ionic states formed upon electronic relaxation or molecular fragmentation [40]. The blue and red arrows represent the absorption of photons from XUV and optical laser radiation, respectively.

There are several new phenomena, which are investigated in photoionization processes such as sequential ionizations [36, 44] or above threshold ionization of atoms in single-color or studying polarization dependent electron dynamics in two-color experiments [28] by obtaining the angular distribution of the photoelectrons [26]. In the time-resolved study of the electron dynamics in non-linear processes with XUV and optical laser sources, the polarization of the light can play a valuable role for the understanding of the electron transitions in atomic systems, since it allows e.g. for a deliberate excitation of magnetic substates. Investigations of non-linear processes in atoms with circularly polarized XUV and optical laser pulses, especially with both co-and counter rotating helicities of the two radiation sources, give the opportunity to study the different response of the target to changes of the polarization state of the incident light pulses and the highly sensitive dynamics of the underlying processes [26]. Moreover, studies of the circular dichroism, different responses of the target system to right- and left-circularly polarized light, are valuable, since they can open the possibility to investigate dichroic properties in electronic systems and chiral matter [26, 45, 46].

In the context of this work, new phenomena such as circular dichroism in the above threshold ionization of atoms and polarization dependent dynamics of atoms have been investigated. Moreover, the first user experiment applying an optical laser together with the FEL pulses at the LDM endstation of FERMI revealing a

circular dichroism was performed. This experiment, was a two-color experiment, in which the polarization state and the polarization degree of the of first circularly polarized FEL beam (FERMI) was determined (see chapter 4) [47]. Furthermore, the polarization dependent behavior of oriented ionic systems has been investigated in sequential ionization processes [26] (see chapters 5 and 6).

1.5 Outline

The scientific core of this thesis are different two-color experiments with FEL radiation in combination with near infrared (NIR) femtosecond lasers for the investigation of the electron dynamic in the photoionization of atoms. The next chapter includes a brief overview of the theoretical background for the underlying processes in the photon-atom interaction, as well as for the angular distribution of photoelectrons and the circular dichroism in the photoelectron spectrum. Furthermore, in the context of this work, a two-color pump-probe setup with NIR and HHG has been designed and constructed in the SQS laser lab. The details of this setup including the optimization results of the HHG source are extensively described in chapter 3.

Chapter 4 of this thesis deals with a two-color pump-probe experiment at FERMI and the circular dichroism as a tool for characterization of the FEL pulses and determining the polarization state of FERMI. Furthermore, the dependence of the photoelectron angular distribution (PAD) to the intensity of the NIR laser beam and the circular dichroism in the PAD in two-color photoionization of Helium is described in chapter 5.

Chapter 6, includes the investigation of resonant sequential photoionization and probing resonantly excited ionic species in a two-color pump-probe experiment performed with the FEL and femtosecond optical laser pulses. This thesis is concluded in chapter 7.

CHAPTER 2

Theoretical Background

An atomic or molecular target, which is radiated with an electromagnetic wave, can interact with the incident photons so that an electron (or more) is ejected from the Coulomb potential of the target. This kind of photon-matter interaction is known as photoionization. The photoionization of e.g. an atom can be realized by absorption of a single photon with high enough photon energy (higher than the smallest electron binding energy of the target atom) or by the simultaneous absorption of many lower energy photons, depending on the scope of the experiment. Typical high brightness photon sources used for photoionization are optical lasers, high-order harmonic generation (HHG) sources, synchrotron radiation facilities or free-electron lasers (FELs). For these sources, the mechanisms of photoionization can be vastly different as discussed in the following sections.

Electrons and ions produced in the photoionization of an atomic target are carrying information about the original electronic state of the atom. This information can be extracted from the photoelectron spectrum and photoelectron angular distribution, which can provide insight into the complex electron properties and interactions inside the atom [48, 49]. Moreover, in the case of molecules, the charged particles produced in the photoionization and possible subsequent fragmentation provide information about the chemical bondings and the original molecular structure [49]. Therefore, investigations of photoionization processes in general, open the opportunity for fundamental research in different fields of physics, chemistry and material sciences [48, 49].

The experimental investigations performed in the context of this thesis are based on studies with atoms. Therefore, the theoretical background discussed in this chapter concentrates on the photoionization of atoms. In the first section, the photoionization processes are categorized in single-photon ionization and the related decay processes (section 2.1.1) and multi-photon ionization (section 2.1.2). In the second section, the angular distribution of photoelectrons produced in an ionization process and the specific effect of circular dichroism in the photoionization are described.

2.1 Photoionization Processes in Atoms

A photon with energy $\hbar\omega$, which is absorbed by an atom, can lead to the transition of an electron in the atom from an initial state with energy E_i to the final state with energy E_f, where $E_i - E_f = \hbar\omega$. For the case of a higher photon energy than the ionization potential of the atom ($\hbar\omega > I_p$), an electron is ejected from the atom into the continuum and will leave the atomic potential with a kinetic energy $E_{kin} = \hbar\omega - I_p$ [49].

In photoionization processes, the probability of ionizing an atom can be quantified by the photoionization cross section. In classical mechanics, the photoionization cross section (σ) is defined as the ratio of absorbing area to the total area of the photon-matter interaction volume. However, in quantum mechanics, the photoionization cross section is related to the electron transition probability (T_{if}) from the initial to the final state and is given by Fermi's golden rule [50]:

$$T_{if} = \frac{4\pi^2}{h} |< \phi_f \mid \hat{H} \mid \phi_i >|^2 \ \delta(E_i - E_f - h\omega), \tag{2.1}$$

where $\hat{H}$ is the Hamiltonian operator, ϕ_i and ϕ_f are the initial and final electron wave function, respectively. E_i and E_f are the initial and the final energy of the electron. Neglecting the recoil energy to the ion within the Born-Oppenheimer approximation, the partial photoionization cross section can be defined as follows [51, 52, 53]:

$$\sigma(h\omega) = \frac{4\pi^2\alpha^2}{h} \sum_{i,f} |< \psi_f \mid \sum_n e^{i\vec{k_\omega}\vec{r_n}} \vec{\epsilon}\nabla_n \mid \psi_i >|^2, \tag{2.2}$$

where α is the fine structure coefficient, $\vec{k_\omega}$ is representing the momentum of the incident photon of the field, $\vec{\epsilon}$ is the polarization vector of the photon, $\vec{r_n}$ and ∇_n are the position operator and the momentum operator of the n^{th} electron. ψ_i and ψ_f are the normalized electron wave function of the initial and final state, respectively. Considering only the dipole part of the interaction Hamiltonian, the photoionization cross section can be redefined as:

$$\sigma(h\omega) = \frac{4\pi^2\alpha a_0^2}{3} h\omega \sum_{i,f} |< \psi_f \mid \sum_n \vec{r_n} \mid \psi_i >|^2, \tag{2.3}$$

where ψ_i and ψ_f are degenerated states [51, 53].

2.1.1 Single-Photon Ionization

Single-photon ionization can occur, when the photon energy of the ionizing radiation source is larger than the binding energy of the electron in the target atom so that the absorption of a single photon can ionize the atom [53]. The outermost valence electron in an atom has the lowest binding energy and therefore, needs the

lowest amount of photon energy (in comparison to the other electrons in the atom) to be released from the atomic potential. In this case, the energy of a single photon from a VUV radiation source (e.g. HHG) is sufficient to ionize the atom [49].

In order to eject electrons from inner shells of an atom, higher photon energies are required varying from several tens eV to the order of several tens of keV. For this kind of single-photon ionization, radiation sources at shorter wavelengths (XUV to X-rays) such as synchrotron radiation facilities and FELs are needed.

After photoionization of inner-shell electrons of an atom, the electronic structure of the atom starts to rearrange electrons in a relaxation process, due to the vacancy left by the ejected electron, in order to stabilize the electronic structure.

Thereby the binding energy difference of the inner- and outer-shell can be released in form of a fluorescence photon or Auger electron. In case of a fluorescence decay the ionic state of the target does not change, since no additional electron is ejected (Fig.2.1.a) [49, 48].

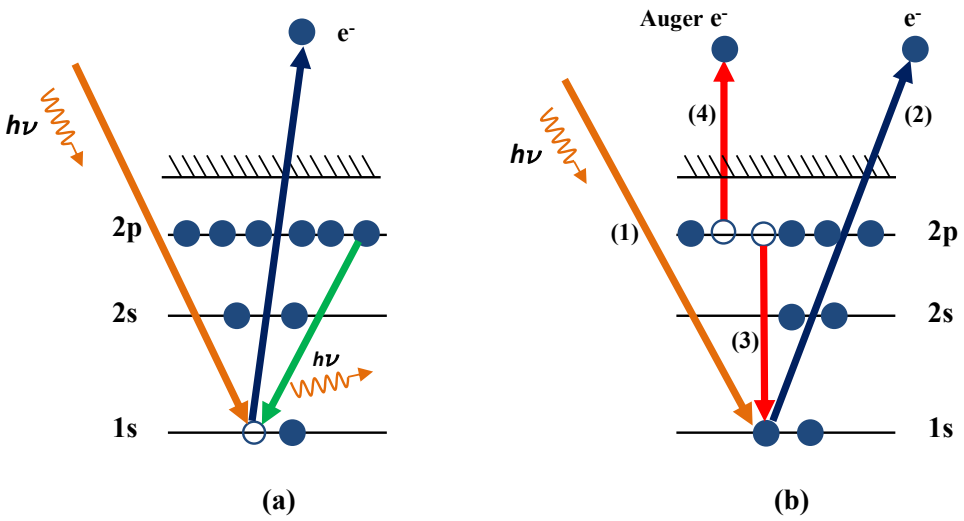

Figure 2.1: Single-photon ionization: (a) Single-photon ionization of an inner-shell electron and a fluorescence decay from the 2p to 1s state (green arrow). (b) Single-photon ionization of an inner-shell, (1) absorption of the photon by the inner-shell electron, (2) ejection of the inner-shell electron, (3) Auger decay of an outer-shell electron to fill the vacancy created by the ejected electron and (4) the released energy from the Auger decay is transferred to another outer-shell electron (Auger electron), which is then also ejected from the atomic Coulomb potential.

The Auger decay is a non-radiative relaxation process, where a second electron is released from the Coulomb potential of the ion (Fig.2.1.b). In this relaxation pro-

cess an outer-shell electron fills the vacancy left by the ejected inner-shell electron. Thereby the energy difference of the outer- and inner-shell ($E_{in} - E_{out}$) is transferred to another electron in the outer-shells with a binding energy $E_{bind} < E_{in} - E_{out}$ and this electron can also escape the atomic Coulomb potential [51, 53]. There are also other special cases of the Auger decay, e.g. resonance Auger decay [48], which are not explained in the context of this thesis.

Within an ionization process of inner-shell electrons, it is also possible that additional processes such as excitation and emission of other electrons can occur besides the main relaxation decays, which are not discussed here since they are not appearing in the experiments performed for this thesis.

2.1.2 Multi-Photon Ionization

The absorption of more than one photon by matter is called multi-photon interaction. This interaction can lead to several different scenarios where either multiple ionizations are occurring or ionization is preceded by excitations. Direct multi-photon ionization can occur in the interaction of an intense radiation field with e.g. an atom, where the energy of a single photon is not sufficient to ionize the atom. In general, there are different scenarios for the multi-photon ionization, e.g. sequential ionization, direct ionization and interactions with two (or more) light sources, which are discussed in this section and the following parts of this chapter.

Multi-photon interactions are utilized for investigating dynamics in the electronic structure of atoms, for studying outer- as well as inner-shell transitions in atoms. Generally, in multi-photon ionization, the radiation pulse contains a high number of photons within a small volume and a short time interval and can be generated by an intense optical femtosecond laser or by an FEL. In the photoionization with high intensity sources there can be different regimes of ionization processes, which have to be distinguished. The categorization of these regimes is generally done by the Keldysh parameter γ. This parameter is defined in the following equation [54]:

$$\gamma = \sqrt{\frac{I_p}{2U_p}}, \tag{2.4}$$

where I_p is the ionization energy of the ejected electron. U_p is the so called ponderomotive energy, which can be defined as the average energy gained by the electron in the electromagnetic field of a radiation pulse with a frequency of ω_R. The average kinetic energy of all electrons ejected at time t is a function of the phase ($\omega_R t_0$), which depends on the strength of the radiated electric field at t_0. U_p can be calculated from the following equation [55]:

$$U_p = \langle \frac{1}{2} m_e v^2 \rangle = \frac{e^2 E_R^2}{4 m_e \omega_R^2} (1 + 2\cos^2 \omega_R t) = const\, \frac{I_R}{4\omega_R^2}, \tag{2.5}$$

where E_R and I_R are the electric field and intensity of the radiation pulses, respec-

tively. U_p is also known as the ponderomotive potential.

According to the Keldysh parameter, photoionization processes with low frequency radiation fields ($\hbar\omega < I_p$), where the atom cannot be ionized by a single photon, are categorized in three mechanisms (see Fig.2.2).

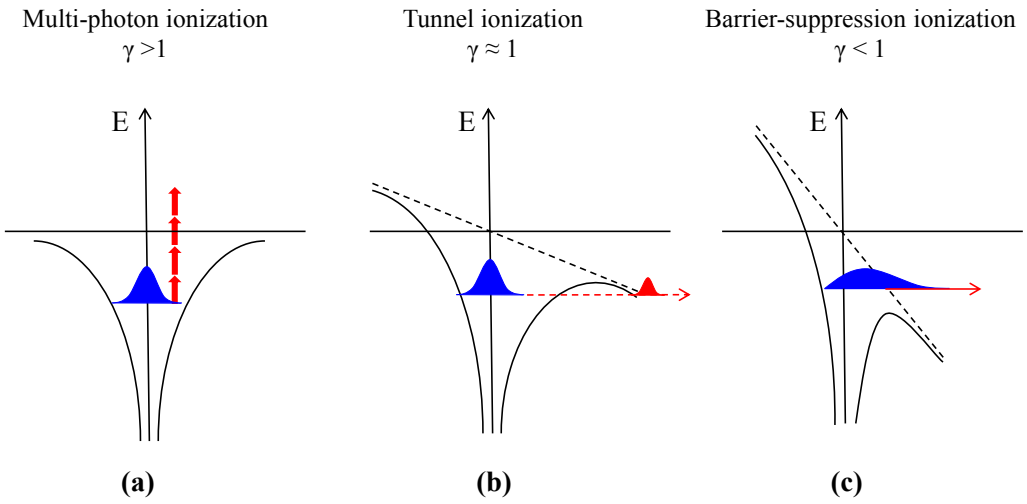

Figure 2.2: Categories of photoionization processes induced by an optical laser (800nm wavelength) for different values of the Keldysh parameter. (a) Multiphoton ionization: Absorption of more than one photon of a low intensity ($I \leq 10^{13}\,W/cm^2$) radiation pulse. (b) Tunnel ionization: in the interaction of a high intensity ($I \sim 10^{14-15}\,W/cm^2$) light pulse with the atom, the strong electric field will deform the atomic potential so that the electron can tunnel through its barrier. (c) Barrier-suppression ionization: In case of a high enough intensity of the radiation ($> 10^{15} W/cm^2$) or specific cases of excited states the potential barrier of the atom is completely suppressed so that the electron can escape the atomic coulomb potential [56]. The vertical axes are energy axes.

In the first category, where $\gamma > 1$, the radiated electric field is not influencing the Coulomb potential of the atom. In this case, the photoionization process can happen only if more than one photon is absorbed by the atom. This kind of photoionization is a non-linear process and is known as direct multi-photon ionization (see Fig.2.2.a)[57]. In this process, the minimum number of photons (N_{min}) absorbed by the atom is so that their total energy is just enough ($N_{min}h\nu \geq I_p$) to eject the electron from the atomic potential. It is also possible for the atom to absorb more photons ($N > N_{min}$). In this case the photoelectron escapes the atomic potential with larger kinetic energy $E_{kin} = N \times h\nu - I_p$. This kind of multi-photon process is known as the above-threshold ionization (ATI) [58, 59].

The second category, where $\gamma \approx 1$, is when the radiation intensity is about $I \approx 10^{14} - 10^{15} W/cm^2$, which is high enough to deform the atomic Coulomb potential so that the electron can tunnel through the potential barrier and a tunnel ionization process can occur (Fig.2.2.b). Taking into account that the radiation electric field is not static, but oscillating, the tunnel ionization can appear in each optical cycle of the pulse and accordingly limiting it to low enough frequencies to allow for sufficient time for tunneling [57, 60].

The third case is when the laser intensity is above $10^{15} W/cm^2$ ($\gamma \ll 1$) and the atomic potential barrier is suppressed by the strong electric field of the laser so that the electron is not bound anymore and become free (Fig.2.2.c). This kind of photoionization is called the barrier-suppression ionization (BSI). The relevance of excited states for suppressing the tunneling regime and entering the BSI regime at lower intensities will be further discussed in chapter 6.

Multi-photon processes can be commonly observed in photoionization experiments with optical lasers [61] or FEL sources [35]. FEL sources can provide radiations with intensities up to $10^{18} W/cm^2$, which is higher than the common intensity of optical lasers (about $10^{16} W/cm^2$). However, the currently accessible photon energy in the short wavelength range of FELs (20 eV to 20000 eV) is much higher than for optical lasers. Therefore, due to the high photon energy, the atomic potential of the target cannot react to the fast changing electric field of these radiations. Accordingly, the high frequency of FELs leads to a low ponderomotive potential (see equation 2.5) and therefore, the Keldysh parameter in ionization processes with FEL radiation is much higher than one, which defines the multi-photon ionization regime. The tunnel ionization and BSI regimes typically appear in the photoionization with intense optical lasers [62, 63, 64, 65].

The multi-photon ionization with high frequency photons can be further categorized in different processes such as sequential ionization and direct ionization [35]. The sequential ionization appears when a highly intense radiation pulse (typically tens to hundreds of fs) interacts with the atomic target. As shown in figure 2.3.a, if more than one photon from the light pulse is absorbed by the atom so that the first photon ionizes the neutral target atom A and the second photon ionizes the singly charged ion A^+ to A^{++}, so that the target is sequentially ionized by photons of the same pulse.

Direct double-photon ionization with short wavelength pulses appears when two photons of a pulse are absorbed by one individual electron simultaneously (see Fig.2.3.b). This process occurs in experiments with FEL radiation at high peak intensities ($10^{13} - 10^{16} W/cm^2$) [36, 66]. First experimental results on the yield differences between sequential and direct double-photon ionization point to about 5 orders of magnitude lower yield of the direct processes compared to one photon single ionization [34]. Fig.2.3.c displays the case of a resonance as intermediate step towards the continuum which can substantially enhance the yield for a multi-photon ionization. The polarization dependent study of such resonances in a two-color scheme is subject of chapter 6. Fig.2.3.d depicts the case of above

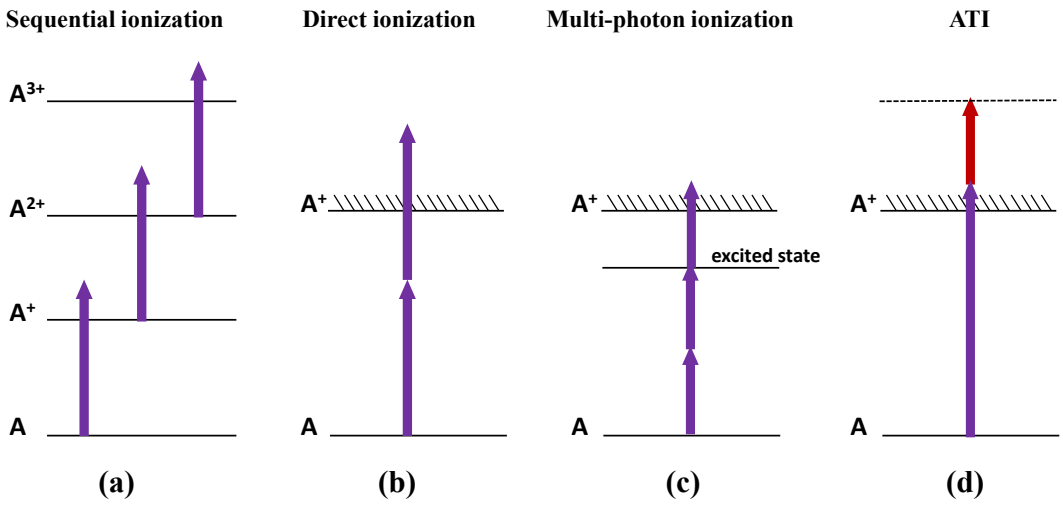

Figure 2.3: Multi-photon ionization categories: (a) Sequential ionization, where more than one photon of a pulse are sequentially absorbed by atom A. The first photon ionizes the neutral atom, the second photon ionizes the ion A^+ and the third photon the ion A^{++}. (b) Direct ionization, where two photons of a short pulse are absorbed by the same electron in the atom. (c) Resonant enhanced multi-photon ionization. The absorption of two photons excites the atom and an additional photon ionizes the excited atom. (d) Above threshold ionization (ATI) of the atom A, where the atom is ionized by a short wavelength photon and at the same time a second photon from an optical laser (red arrow) is absorbed by the ejected electron.

threshold ionization (ATI), which principally means that more photons are absorbed than needed for the ionization. This leads to additional spectral features such as electronic sidebands as further discussed in chapters 4 and 5.

The experiments performed in the context of this thesis are two-color experiments with temporally synchronized optical laser (NIR) and FEL pulses (see chapters 4 to 6). In the single-photon ionization with FEL pulses, where the target atom is dressed by an intense optical laser, the atom can simultaneously absorb or stimulated emit an NIR photon (or more) in addition to the absorption of the FEL photon. In the photoelectron spectrum of these processes, additional peaks appear on both sides of the main photoline, resulted from the absorption of the FEL photon. These peaks are known as sidebands (see chapter 4 for more details). Moreover, the interaction of the strong optical laser field with the electronic structure of the atom can lead to an energy shift of the electronic states in the atom. This effect is known as AC Stark shift (see chapter 6) [67].

In general, the shift of energy levels of an atom in a static electric field is known as Stark shift or the DC Stark shift. As it was explained by Delone and Krainov [67],

one main difference between the AC- and DC Stark shift is that in a static electric field (DC Stark shift) the perturbation of a nondegenerate bound atomic state results in a shift of that state, while in a laser field (monochromatic electromagnetic field) the initial nondegenerate state is transformed into an assembly of quasi-energy states. Moreover, in case of AC Stark shift, for a laser frequency close (not exactly the same) to a certain transition frequency between two states in the atom, each of the energy states (i.e. lower- and higher states) will split into quasi-energy states so that a resonant transition of electrons will occur. This phenomenon is known as the Rabi effect [67].

2.2 Angular Distribution of Photoelectrons

In a photoionization process, photoelectrons leave their parent ions by different emission angles in all directions [1]. In the following part of this section, the angular distribution of the photoelectrons in linearly- and circularly polarized light fields is described.

2.2.1 Photoelectron Angular Distribution in a Linearly Polarized Light Field

The emission probability of photoelectrons in a solid angle unit $d\Omega$ is given by the differential cross section. In case of a linearly polarized light field the symmetry axis is the same as the electric field vector, whereas in case of an unpolarized or a circularly polarized field it is the propagation axis of the light field [48, 68, 69].

The differential cross section can be written as a function of Legendre polynomials [69]:

$$\frac{d\sigma}{d\Omega} = \frac{\sigma}{4\pi} \sum_{k=1}^{N} B_k \, P_k(\cos\theta), \tag{2.6}$$

where θ represents the angle between the photoelectron emission vector and the electric field vector of the incident beam. Within the dipole approximation, B_k coefficients are equal to zero for an odd number k due to symmetry reasons [69]. As an example, in case of a single photon ionization within the dipole approximation, by applying the dipole approximation, all B_k coefficients except B_0 and B_2 will equal Zero. The B coefficients are commonly denoted by β and called the anisotropy parameter. For the simple case of single photon ionization, the differential cross section equation can be simplified [69]:

$$\frac{d\sigma}{d\Omega} = \frac{\sigma}{4\pi}(1 + \beta P_2(\cos\theta)), \tag{2.7}$$

[1] The description for the angular distribution in this section is based on the detailed explanation in reference [68] and references therein.

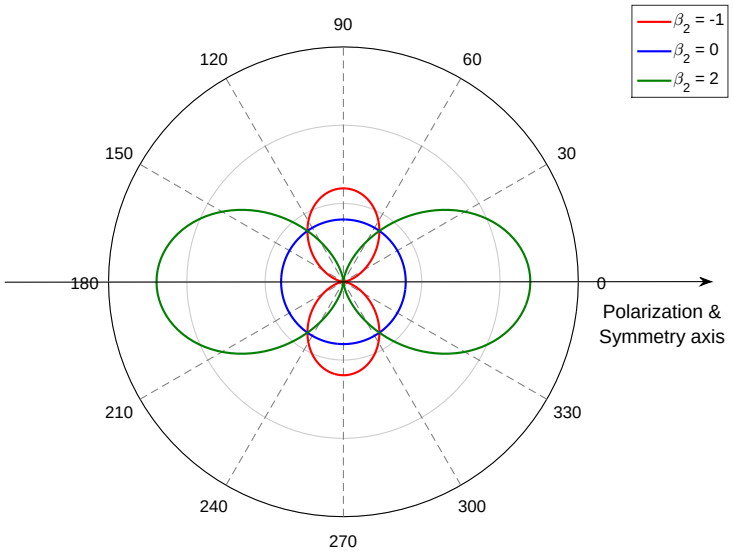

Figure 2.4: The angular distribution of photoelectrons produced in the interaction with one photon from a linearly polarized light field in a two dimensional plane for different values of the anisotropy parameter β_2. Note that the propagation axis of the light field is perpendicular to the plane of the figure.

where

$$P_2(\cos\theta) = \frac{1}{2}(3(\cos^2\theta) - 1). \tag{2.8}$$

As it is shown in the equation 2.7, the photoelectron angular distribution is defined by the anisotropy parameter β. In case of a linearly polarized radiation, the value of the anisotropy parameter (β_L) ranges from -1 to 2, since for all other values of β_L the differential cross section can be negative [70]. The angular distribution can be further simplified for particular angles, e.g. $\theta = \pm 54.7\,\text{deg}, \pm 125.3\,\text{deg}$, the so-called "magic angle", because under this angle the total cross section can be determined without further knowledge of the angular distribution:

$$\frac{d\sigma}{d\Omega} = \frac{\sigma}{4\pi}, \tag{2.9}$$

Figure 2.4 shows the angular distribution of photoelectrons for $\beta_L = -1, \beta_L = 0$ and $\beta_L = 2$ for a horizontal linearly polarized field. The symmetry axis of the angular distribution for different β_L-parameters is the linear polarization axis, which is taken as quantization axis.

2.2.2 Angular Distribution in a Circularly Polarized Light Field

For a circularly polarized light field, equation 2.6 can be written as the following:

$$\left(\frac{d\sigma}{d\Omega}\right)_{\nu\nu'} = \frac{\sigma}{4\pi}\sum_{k=1}^{N}\beta_k^{\nu\nu'}\,P_k(\cos\theta), \tag{2.10}$$

where the notation ν, ν' is for different helicities of the circularly polarized light field. For the simple case of single-photon ionization with circularly polarized photons the asymmetry parameter

$$\beta_2^{\nu\nu'} = -\frac{1}{2}\beta_L. \tag{2.11}$$

The first Legendre coefficient $\beta_1^{\nu\nu'}$ for a circular polarized incident photon is nonzero [68, 70, 71] (see also [72] and references therein). The sign of this coefficient is changing, reversing the helicity of the circular polarization:

$$\beta_1^{\nu} = -\beta_1^{\nu'}. \tag{2.12}$$

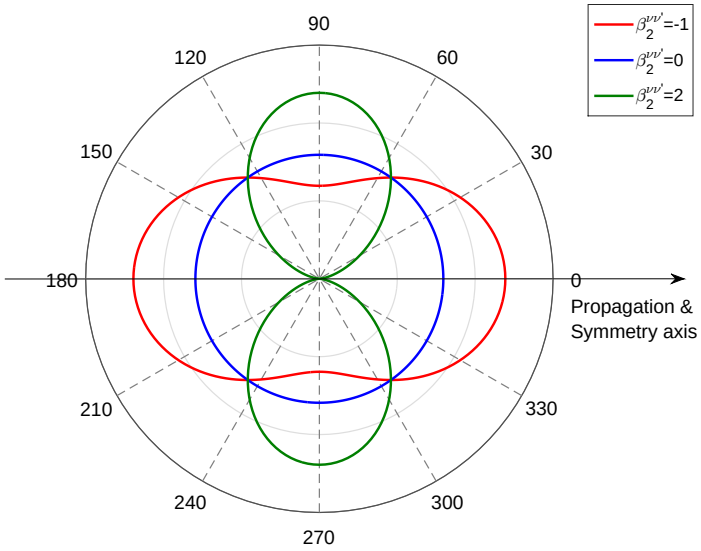

Figure 2.5: The angular distribution of photoelectrons produced in the interaction with one photon from a circularly polarized light field in a two dimensional plane for different values of the anisotropy parameter $\beta_2^{\nu\nu'}$. Note that the figure is showing a slice along the symmetry axis of the angular distribution of the photoelectrons, which is the propagation axis of the light field. Note that the angle grid in this figure is not for the azimuthal angle θ.

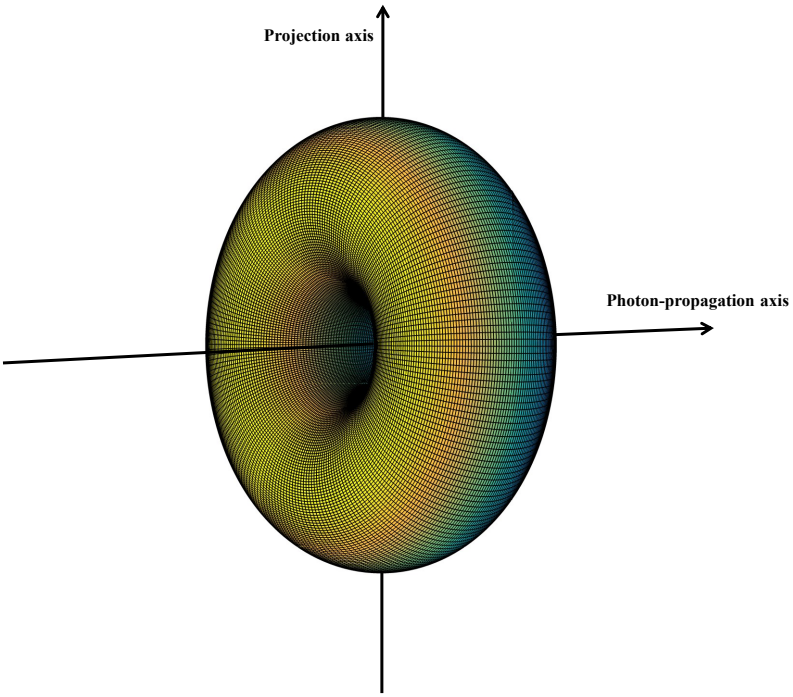

Figure 2.6: The donut-form of photoelectron angular distribution for $\beta_2^{\nu\nu'} = 2$ in a circularly polarized light field, i.e. in the single-photon ionization in a He atom, where the absorption of one photon ($l = \pm 1$) produces a photoelectron in the continuum state p, $m = \pm 1$. The projection axis is perpendicular to the propagation axis of the light and is showing towards a spectrometer, where the photoelectrons are detected.

In case of an unpolarized atomic or molecular target the coefficient $\beta_1^{\nu\nu'}$ is equal to Zero [68, 70]. Therefore, the differential cross section can be simplified in the following equation:

$$\left(\frac{d\sigma}{d\Omega}\right)_{\nu\nu'} = \frac{\sigma}{4\pi}\left(1 - \frac{\beta_2^{\nu\nu'}}{2}\left(\frac{3}{2}\cos^2\theta - \frac{1}{2}\right)\right). \tag{2.13}$$

The angular distribution of photoelectrons for different values of $\beta^{\nu\nu'}$ is shown in figures 2.5 and 2.6.

Considering an experimental situation where an unpolarized target can interact with more than one photon at the same time, the equation of the differential cross section will change to:

$$\frac{d\sigma}{d\Omega} = \frac{\sigma}{4\pi}\sum_n \beta_{2n} P_{2n}(\cos\theta), \tag{2.14}$$

where n is the number of interacting photons. As it is demonstrated in Yang's theorem [69], using the dipole approximation for a multiphoton interaction of cir-

cularly polarized photons and an atom in a spherically symmetric state, the cross section can be calculated from the following equation:

$$\left(\frac{d\sigma}{d\Omega}\right)_{\nu\nu'} = \frac{\sigma_{\nu\nu'}}{4\pi}\left(1 + \sum_{k=1}^{N} \beta_{2k}^{\nu\nu'} P_{2k}(\cos\theta)\right), \tag{2.15}$$

where k is the number of photons involved in the ionization process, $P_n(x)$ are the Legendre polynomials, $\beta_{2k}^{\nu\nu'}$ are the asymmetry parameters and $\sigma_{\nu\nu'}$ denotes the angle integrated cross section. The angle θ is the emission angle of the photoelectrons with respect to the propagation axis of the beams, considering e.g. a two-color photoionization process with two circularly polarized light fields propagating collinearly. ν, ν' are denoting the helicity of the incident beams, which can be right and left circularly polarized. The photoelectron angular distribution is not only axially symmetric, but also symmetric with respect to $\theta = \pi/2$ (Eq.2.15) [51, 69, 70].

2.3 Dichroism in Photoionization

The polarization dependent difference in light-matter interaction is commonly called dichroism. The origin of this phenomenon can be either related to spin properties of the studied material [25, 73, 74] or an asymmetric chiral structure [45, 75]. This dichroic effect of the material in interaction with a linearly- or circularly polarized photon is called linear dichroism or circular dichroism, respectively [73].

In general, dichroism is a powerful tool to gain information about the magnetic or stereochemical structure of solids and molecules in the interaction with VUV and X-ray radiation, respectively. These phenomena have historically often been studied with lasers and synchrotrons [45, 73]. The interest ranges from fundamental spin control [76] to (bio-)chemistry [24] and material science such as magnetization studies [25]. Furthermore, in photoionization processes with an atomic target, the dichroism can be imprinted in the photon absorption probability of magnetic substates as well as in resulting partial wave compositions and therefore in the electron angular distributions. This kind of investigations can be realized by experiments with VUV or X-ray sources on a certain atomic target in the gas phase. However, in order to study the dichroic effect, the atomic target has to be polarized. Therefore, in these experiments the target atom polarization can be induced by the absorption of photons from an optical laser [73].

Figure 2.7 shows a general scheme of methods for studying different kinds of dichroism in the photoionization of electrons of an atomic target. The circular dichroism in the photoelectron angular distribution (CDAD) is studied by both circularly polarized XUV and optical laser (Fig.2.7.a). The linear dichroism in the angular distribution of photoelectrons (LDAD) can be investigated by a linearly polarized XUV beam and a circularly polarized optical laser (Fig.2.7.b). In case of both linearly polarized XUV and laser beams, one speaks about a linear alignment

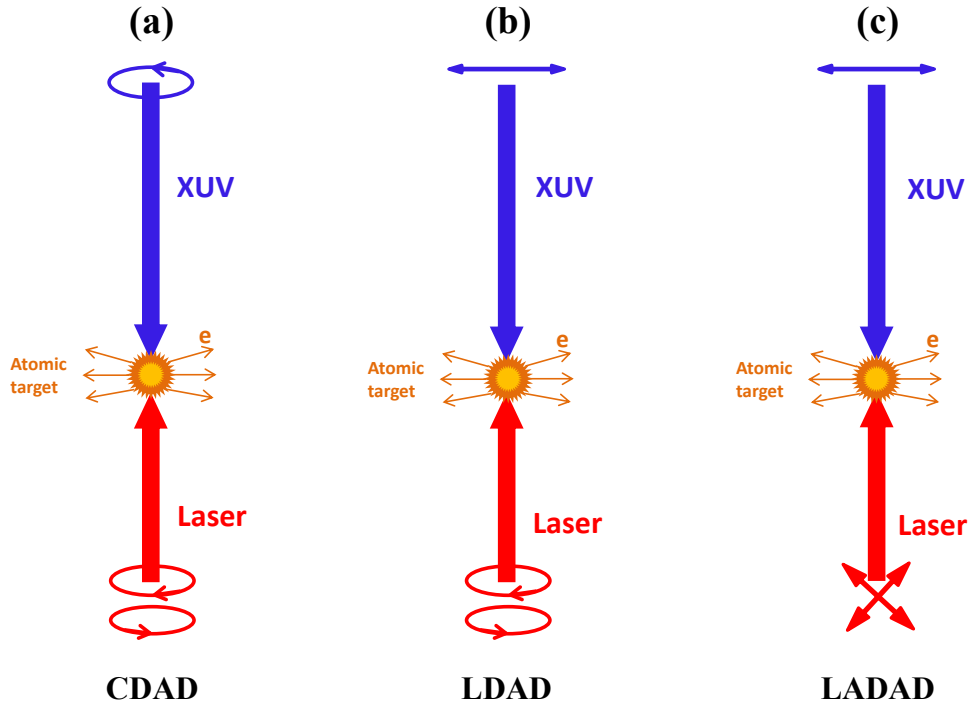

Figure 2.7: Methods of studying dichroism in the photoionization of an atom by different polarization combinations of co-axially oriented XUV and optical laser beams. (a) Circularly polarized XUV and optical laser for studying CDAD (see text). (b) Linearly polarized XUV combined with circularly polarized optical laser for the investigation of LDAD. (c) Both linearly polarized XUV and optical laser for the investigation of (see text) [73].

dichroism in the angular distribution (LADAD) of photoelectrons (Fig.2.7.c) [73].

In this thesis, the experimental investigations on dichroism have been performed with synchronized circularly polarized XUV (FEL) and optical laser sources. Therefore, the following section describes only the circular dichroism.

2.3.1 Circular Dichroism in Photoelectron Spectroscopy

In experiments performed in the context of this thesis, the photoelectron angular distribution are investigated in photoionization processes with circularly polarized XUV and optical laser radiations. Thereby, the angular distribution can be sensitive to the relative helicity of the radiations. A simultaneous change in the helicity of both beams will not change the angular distribution of the photoelectrons due to the preserved symmetry [75]. However, changing the helicity of one of the beams, the photoelectron angular distribution can differ as the values of $\sigma_{\nu\nu'}$ and $\beta_{2k}^{\nu\nu'}$ in equation 2.10 are unequal for the co-rotating ($\nu = \nu'$) and counter-rotating ($\nu \neq \nu'$) light fields. This results in a circular dichroism in the integrated cross

section and in the angular distribution of the photoelectrons. The circular dichroism in the angular distribution (CDAD) is defined by the ratio of the subtraction of differential cross sections for co-rotating and counter-rotating fields to the sum of them:

$$CDAD = \frac{\left[\left(\frac{d\sigma}{d\Omega}\right)_{\nu\nu} - \left(\frac{d\sigma}{d\Omega}\right)_{\nu\nu'}\right]}{\left[\left(\frac{d\sigma}{d\Omega}\right)_{\nu\nu} + \left(\frac{d\sigma}{d\Omega}\right)_{\nu\nu'}\right]}, \tag{2.16}$$

considering $\nu \neq \nu'$. The circular dichroism (CD) for the angle integrated cross section can be written in a similar way:

$$CD = \frac{\sigma_{\nu\nu} - \sigma_{\nu\nu'}}{\sigma_{\nu\nu} + \sigma_{\nu\nu'}}. \tag{2.17}$$

The circular dichroism in the multi-photon ionization process can theoretically be described in different approaches. The first one is the time dependent theoretical model which has been developed based on the strong field approximation (SFA) [54, 77, 78]). The time-dependent model is more convenient in case of fast photoelectrons with a kinetic energy of several tens of eV as the re-scattering effect by the ions is negligible in this case [39]. Using the SFA approach is appropriate for the case of a low intensity NIR field, where only one or two NIR photons are interacting with the target, as well as in the high intensity case where more photons interact. Therefore, the time dependent strong field approximation approach is an adequate model to study the dependence of the photoelectron angular distribution and the circular dichroism on the intensity of the NIR beam.

The second approach is the standard perturbation theory considering long pulses, so that the time structure of the pulses is neglected in the equations. This approach uses a tensor analysis method which is based on the rotation invariance and symmetry arguments. Thus, for any polarization of the photons it is possible to predict the general form of the photoelectron angular distribution [79]. The analysis of experimental data based on this approach can provide detailed information about the contribution of electronic partial waves. The perturbation theory approach enables to consider a set of measurements in multiphoton ionizations, which gives the transition matrix elements including the phases of the electronic partial waves [80]. The disadvantage of the perturbation approach is that the calculation can be practically applied only for up to two NIR photon absorptions regardless of the XUV radiation, as the demonstration of the asymmetry parameters in the angular distributions for the cases of three and more photon absorptions become complicated.

Considering a strong NIR laser field ($10^{11} - 10^{13} W/cm^2$), the influence of the laser on the atomic and the bound ionic states can be neglected in the time dependent SFA as well as in the perturbation theory approach. In this context, both theoretical approaches have been applied to calculate the angular distribution and circular dichroism of He atoms, which is described in more details in the following sections.

2.4 Time Dependent Strong Field Approximation

The theoretical studies and calculations of the time dependent strong field approximation (SFA) for the XUV photoionization process of an atom in a dressed NIR laser field was developed by A. K. Kazansky et al. and published in 2011 [77]. In this section, these calculations are briefly described closely based on reference [77].

The two-color (XUV and NIR) photoionization of an atom can be considered within the first-order time-dependent perturbation theory. Hence, the amplitude of the transition from the initial atomic state Ψ_0 to the final state including the ionic state Ψ_f and the emitted photoelectron state $\psi_{\vec{k}}$can be written as [77]:

$$\mathcal{A}_{\vec{k}} \sim -i \int_{-\infty}^{\infty} dt\, \tilde{\mathcal{E}_X}(t)\, \langle \Psi_f\, \psi_{\vec{k}}(t) \mid \hat{D} \mid \Psi_0 \rangle\, e^{-i(E_b-\omega_X)t}\,, \tag{2.18}$$

where $\tilde{\mathcal{E}_X}$ is the envelope of the XUV pulse, ω_X is the corresponding mean frequency, $E_b = E_0 - E_f$ denotes the binding energy of the electron and $\hat{D}$ is the dipole operator. For a circularly polarized XUV beam with polarization vector $\vec{\epsilon}_X^{\pm}$, the dipole operator is given by the following equation:

$$\hat{D}^{\pm} = (\vec{\epsilon}_X^{\pm}\, \vec{r}) = -\sqrt{4\pi/3}\; r Y_{1,\pm 1}(\hat{r}), \tag{2.19}$$

where the plus and minus signs correspond to right and left circularly polarized XUV radiation, respectively. Y_{lm} is a spherical harmonic. Considering a right circular polarization for both fields XUV and IR as well as an s-orbital ionization, equation (2.18) is redefined as:

$$\mathcal{A}_{\vec{k}}^{++} = -i \int_{-\infty}^{\infty} dt\, \tilde{\mathcal{E}_X}(t) d_{sp} Y_{1,+1}(\theta_0(t), \phi_0(t))\, e^{i\phi(\vec{k},t)} e^{-i(E_b-\omega_X)t}\,, \tag{2.20}$$

where θ_0 and ϕ_0 are the initial emission angles of the photoelectron showing its emission direction before propagating in the dressing IR field [39, 81]. In case of a right circularly polarized XUV radiation and a left circularly polarized IR field a similar expression ($\mathcal{A}_{\vec{k}}^{+-}$) can be derived.

For an arbitrary helicity of the XUV (ν) and IR beams (ν'), the differential cross section can be determined from the amplitude:

$$\frac{d\sigma_{\nu\nu'}}{d\Omega}(\theta) \sim \mid \mathcal{A}_{\vec{k}}^{\nu\nu'} \mid^2 . \tag{2.21}$$

Using the equation 2.16, the circular dichroism in the angular distribution of photoelectrons is calculated from the equation:

$$CDAD = \frac{\mid \mathcal{A}_{\vec{k}}^{++} \mid^2 - \mid \mathcal{A}_{\vec{k}}^{+-} \mid^2}{\mid \mathcal{A}_{\vec{k}}^{++} \mid^2 + \mid \mathcal{A}_{\vec{k}}^{+-} \mid^2}. \tag{2.22}$$

And so the integral of the corresponding differential cross section over all angles

will give the angle integrated circular dichroism (see [39] and references therein):

$$CD = \frac{\int d\Omega \mid \mathcal{A}_{\vec{k}}^{++} \mid^2 - \int d\Omega \mid \mathcal{A}_{\vec{k}}^{+-} \mid^2}{\int d\Omega \mid \mathcal{A}_{\vec{k}}^{++} \mid^2 + \int d\Omega \mid \mathcal{A}_{\vec{k}}^{+-} \mid^2}. \tag{2.23}$$

2.5 The Perturbation Theory Approach in Sideband Formation

In the perturbation approach of a two-color above threshold ionization process, the simultaneous absorption of an XUV photon and the absorption (or emission) of an NIR photon is considered first.

Using the dipole approximation, the differential cross section in equation 2.15 for a two photon absorption, can be simplified as the following [39, 82]:

$$\left(\frac{d\sigma}{d\Omega}\right)_{\nu\nu'} = \frac{\sigma_{\nu\nu'}}{4\pi}\left(1 + \beta_2^{\nu\nu'} P_2(\cos\theta) + \beta_4^{\nu\nu'} P_4(\cos\theta)\right). \tag{2.24}$$

In the absorption of a left handed XUV photon ($j = -1$) by the He atom with an electron in the ground state (quantum numbers $s, m = 0$), the electron moves to a continuum state with p-symmetry for the outgoing electron and with a magnetic quantum number of $m = -1$, due to the dipole selection rules, and will result in the main line of the photoelectron spectrum of He (Fig.2.8). Based on the selection rule, an additional absorption of a NIR photon leads to a photoelectron in a s- or d-state. In case of an additional absorption of a left handed NIR photon ($j = -1$) the photoelectron will have a final state with a magnetic quantum number of $m = -2$, which can only be formed by an outgoing d-wave (See figure 2.8). This process will show up as a sideband on the high energy side of the main line in the photoelectron spectrum (higher sideband: HSB). On the other hand, an absorption of a right handed NIR photon ($j = +1$) transfers the photoelectron into a final s- or d-state with a magnetic quantum number of $m = 0$. In case of a stimulated emission of a right handed NIR photon, the electron will move to a d-state ($m = -2$) and for a left handed NIR photon an s- or d-state ($m = 0$) and will appear in the photoelectron spectrum as a sideband with a peak energy lower than the main line (lower sideband: LSB). For a right handed XUV photon (the purple dashed arrow in fig. 2.8), the projection of the angular momentum of the photoelectrons will only change the sign. As it is illustrated in figure 2.8, with a simultaneous change in helicity of the XUV and NIR beams (change from the arrows at the left side to the right half of the figure) the final state of the electron will stay the same (same quantum numbers).

In equation 2.24, the cross section and asymmetry parameters (β) can be written in terms of the emission amplitude of s and d electrons [39]. Therefore, for the absorption of an NIR photon (higher sideband, HSB) the cross section can be

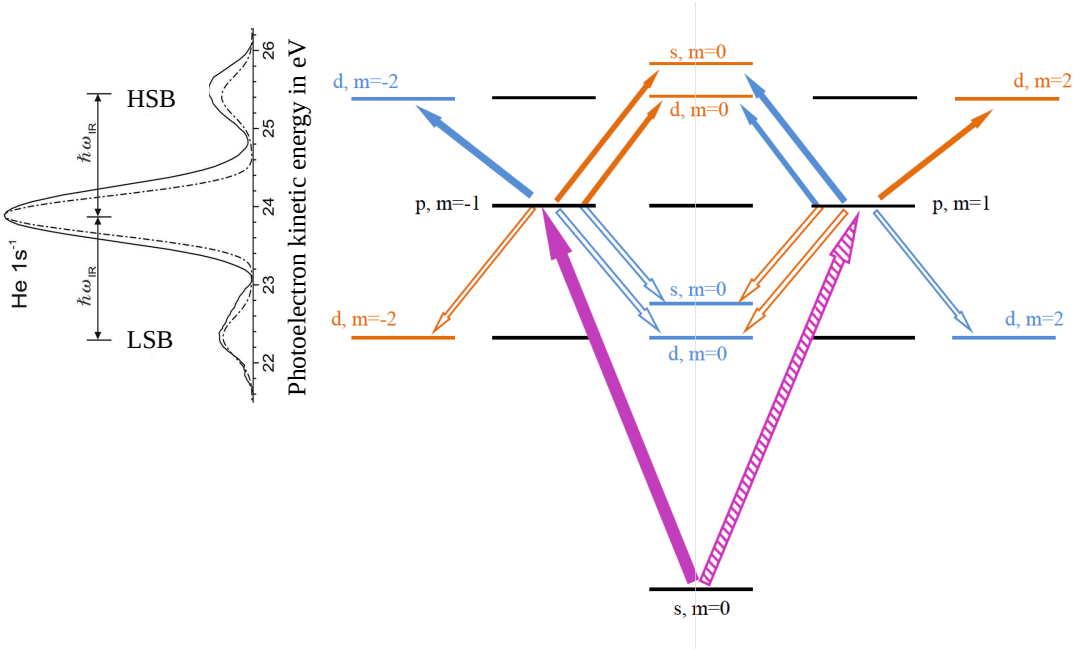

Figure 2.8: Transition scheme of the 1s electron in the ground state of a He atom in interaction with two circularly polarized photons of two-colors (XUV and NIR). The filled (dashed) purple arrow shows the absorption of a left (right) handed XUV photon. The solid blue (red) arrows are corresponding to the additional absorption of a left (right) handed NIR photon and the arrows with no filling are showing the stimulated emission of an NIR photon [39]. The spectrum on the left side was taken from [83].

calculated as the following [39]:

$$\sigma_{+-}(HSB) = 2\pi(2\pi\alpha)^2\omega_{XUV}\omega_{IR}\left(\frac{1}{9} \mid D_s \mid^2 + \frac{1}{45} \mid D_d \mid^2\right), \tag{2.25}$$

$$\beta_2^{+-}(HSB) = \frac{2}{7}\frac{\mid D_d \mid^2 + 7\mathcal{R}[e^{i(\delta_d-\delta_s)}D_sD_d^*]}{\mid D_s \mid^2 + \frac{1}{5} \mid D_d \mid^2}, \tag{2.26}$$

$\mathcal{R}$ denotes the real part,

$$\beta_4^{+-}(HSB) = \frac{18}{35}\frac{\mid D_d \mid^2}{\mid D_s \mid^2 + \frac{1}{5} \mid D_d \mid^2}, \tag{2.27}$$

$$\sigma_{++}(HSB) = 2\pi(2\pi\alpha)^2\omega_{XUV}\omega_{IR} \mid D_d \mid^2, \tag{2.28}$$

$$\beta_2^{++}(HSB) = -\frac{10}{7} \approx -1.43, \tag{2.29}$$

$$\beta_4^{++}(HSB) = \frac{3}{7} \approx 0.43, \tag{2.30}$$

where $\delta_l\,(l = s, d)$ is the electron phase in the continuum, D_l are the radial parts of the two-photon matrix elements [39].

For the calculation of the β-parameters for the lower sideband (LSB) in figure 2.8 (stimulated emission from the p, $m = \pm 1$), equations (2.25) - (2.27) have to be exchanged with equations (2.28) - (2.30):

$$\sigma_{++}(LSB) = 2\pi(2\pi\alpha)^2\omega_{XUV}\omega_{IR}\left(\frac{1}{9} \mid D_s \mid^2 + \frac{1}{45} \mid D_d \mid^2\right), \tag{2.31}$$

$$\beta_2^{++}(LSB) = \frac{2}{7}\frac{\mid D_d \mid^2 + 7\mathcal{R}[e^{i(\delta_d-\delta_s)}D_s D_d^*]}{\mid D_s \mid^2 + \frac{1}{5} \mid D_d \mid^2}, \tag{2.32}$$

$$\beta_4^{++}(LSB) = \frac{18}{35}\frac{\mid D_d \mid^2}{\mid D_s \mid^2 + \frac{1}{5} \mid D_d \mid^2}, \tag{2.33}$$

$$\sigma_{+-}(LSB) = 2\pi(2\pi\alpha)^2\omega_{XUV}\omega_{IR} \mid D_d \mid^2, \tag{2.34}$$

$$\beta_2^{+-}(LSB) = -\frac{10}{7} \approx -1.43, \tag{2.35}$$

$$\beta_4^{+-}(LSB) = \frac{3}{7} \approx 0.43\,. \tag{2.36}$$

In case of co-rotating XUV- and IR-photons (same helicities), the value of the β-parameters for higher sidebands are constant numbers (2.29,2.30) and therefore, independent from the radial matrix elements D_l [39]. For this case, using the equations 2.29 and 2.30, the photoelectron angular distribution (2.24) can be simplified to the following equation [39, 84]:

$$\left(\frac{d\sigma}{d\Omega}\right)_{++} = 2\pi(2\pi\alpha)^2\omega_{XUV}\omega_{IR}\frac{1}{4} \mid D_d \mid^2 \sin^4\theta. \tag{2.37}$$

However, for the case of counter-rotating XUV and IR fields, the result is related to the D_l matrix elements and depends therefore on the atomic model used for the calculation. In this case the integral of the circular dichroism is calculated by the following equation [39, 85]:

$$CD = \pm\frac{5}{7}\frac{\mid D_d \mid^2 - \mid D_s \mid^2}{\mid D_d \mid^2 + \frac{5}{7} \mid D_s \mid^2}, \tag{2.38}$$

where the + (-) sign denotes the higher(lower) sideband. The same kind of calculations can be applied for the absorption of three photons (an XUV- and two

IR-photons) to describe also the second sidebands [39].

2.6 Summary

In this chapter, the theoretical bases of the photoionization process and the angular distribution of photoelectrons in the ionization of atoms were briefly discussed. For most of our experiments the theoretical description was specifically developed by the theoreticians A. Kasansky, N. Kabachnik, A. Grum-Grzhimailo, E. Gryzlova, K. Bartschat and N. Douget (see references [26, 77, 78, 86] and references therein). Moreover, the polarization dependency of the photoelectron yield and their angular distribution in a two-color (XUV and NIR) photoionization process were described shortly, especially the example of circular dichroism in the photoelectron angular distribution of sidebands was discussed for the two theoretical descriptions using the perturbation theory and the strong field approximation. The perturbation theory approach is a useful method for the calculation of the photoelectron angular distribution and circular dichroism in two-color two-photon photoionization processes with XUV sources and low intensity($I \leq 10^{12} W/cm^2$) NIR laser pulses. For the theoretical calculation and predictions of the photoelectron angular distribution and circular dichroism in the two-color multiphoton ionization with XUV pulses and high intensity ($I = 10^{12} - 10^{14} W/cm^2$) NIR laser beam, the time dependent strong field approximation is applied. These two theoretical methods [39, 87, 77] were applied to determine the results of two-color photoionization experiments which have been performed in the context of this work and are described in chapters 4 and 5.

One of the photoionization processes described in this chapter was the tunnel ionization in atoms by the interaction with a highly intense optical laser. This kind of process is used to generate high order harmonics of the optical laser which can provide short pulses with wavelengths in the XUV region. In the following chapter, the generation of the high order harmonics and its applications in two-color experiments are described in more details.

CHAPTER 3

Experiments with High Order Harmonics

The investigation of photoexcitation and photoionization of atoms and molecules enables deep insight into their electron structure and dynamics [88, 89, 90]. Electronic processes are mostly taking place on ultra-fast time scales. Therefore, the dynamics of these processes are typically studied by short light pulses in the femtosecond or attosecond regime. Before the advent of free-electron lasers, this ultrafast regime was dominated by optical lasers and the generation of their higher harmonics (HHG) [91, 92, 93]. For the latter, photon energies can be achieved that enable single photon ionization even of inner-shells of small systems. For optical lasers with relatively long wavelengths, the ionization can be achieved by strong field ionization (see Chapter 2) .

More than fifty years ago, it was demonstrated that propagation of a laser field through a transparent medium such as a crystal can lead to radiation of optical harmonics of the laser [94]. The process was studied in 1967 in a rare gas medium were the third harmonic of the optical laser was observed [95]. This type of experiments were the first steps towards generating high order harmonics with short wavelengths by means of optical lasers.

High order harmonics are generally produced by focusing intense optical laser pulses into a gaseous or a solid medium [55, 96, 97]. The phenomenon originated in a gaseous environment was observed in 1987 for the first time, when McPherson et al. could successfully generate up to the 17^{th} harmonic at 14.6 nm by focusing laser pulses with a wavelength of 248 nm into a neon gas medium [98]. This kind of experimental setup enables the generation of vacuum ultraviolet (VUV) and extreme ultraviolet (XUV) pulses with durations on the femtosecond- or even attosecond time scale.

A main feature of the high harmonic radiation is the temporal and spatial coherence of the pulses. The photon energies provided by high harmonic generation are usually in the range between 10 to 100 eV. However, in special cases HHG sources can also reach photon energies up to the order of keV [6]. In comparison to large scale facilities such as free electron lasers and synchrotron radiation sources delivering short wavelength radiation in the femtosecond and picosecond time scale, respectively, an HHG source has the advantage of much smaller overall size (table top), i.e. it can be set up and used in a conventional laser laboratory. Alternatively,

the major advantage of free-electron lasers over HHG sources is the much higher pulse energy which uniquely enables for example single shot spectroscopy. Synchrotron radiation sources in contrast provide comparably long pulses but they are offering a much larger photon energy range, better stability and a larger average brightness than HHG sources.

There have been several studies to explain the mechanism of the HHG process [99, 100, 101]. An accurate description of the HHG process requires the solution of the time-dependent Schroedinger equation, which is beyond the scope of this chapter. Nevertheless, the process can be described in a classical model for the interaction between atoms and a strong laser field [60]. This model is often called the three-step model and is explained in section 3.2. In the context of this work, an HHG pump-probe experimental setup was designed and constructed for the study of electron dynamic of atoms and molecules. In the following section of this chapter, this setup is described in more details.

3.1 Experimental Setup at the XFEL Laser Lab

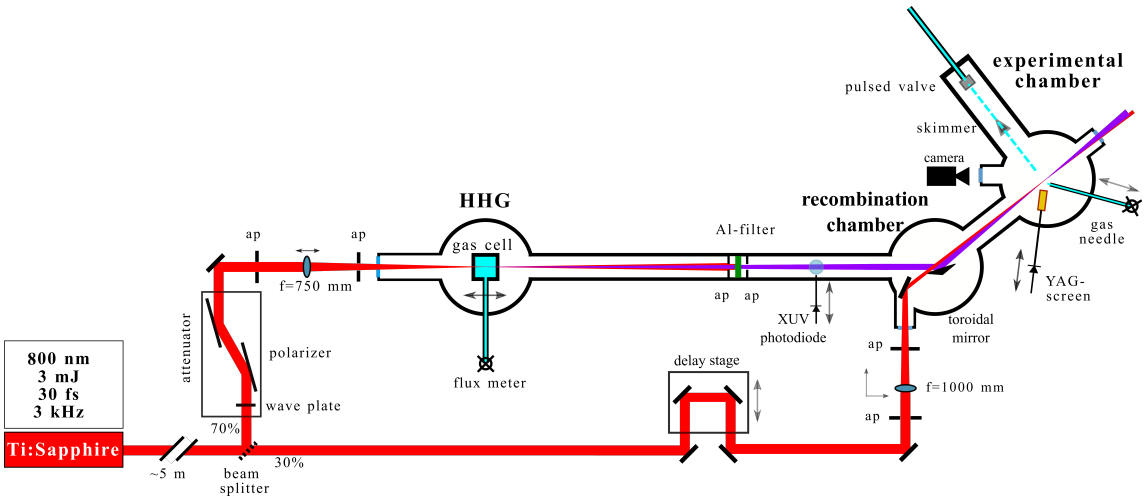

Figure 3.1: The HHG pump-probe experiment at SQS laser lab. The notation "ap" in this schematic means aperture. see text for details.

The pump-probe setup at the SQS laser lab is dedicated to applications for time resolve investigations on different atomic and molecular targets. The setup includes a Ti:sapph femtosecond laser as main light source (Fig.3.1). The Ti:sapph laser used in this setup has a central wavelength of 800 nm. The energy of each laser pulse is about 3 mJ. The laser pulse duration can be set to a minimum value of about 20 fs at a repetition rate of 3 kHz. The laser pulses are split in two parts by a beam splitter. The beam splitter reflects 70% of the laser pulse energy which is used to generate high order harmonics (VUV). The transmitted 30% of the laser radiation is used as NIR source for pump-probe experiments. The VUV

and NIR pulses finally focused at the same point in the interaction region inside the experimental vacuum chamber.

In order to generate VUV pulses, the main part of the fundamental laser pulses reflected from the beam splitter is focused into a gas medium. The laser pulses are focused by a lens with a focal length of 750 mm to a focal spot of $\emptyset = 60\mu m$ inside a gas cell. The peak intensity in the focal region is in the order of $10^{15}\, W/cm^2$. For optimizing the high harmonic pulses, the intensity of the NIR laser beam has to be tuned. This is realized by an attenuator before focusing the laser into the gas medium (Fig.3.1). The attenuator consists of a half wave plate, which enables to rotate the polarization of the laser beam, and two polarizers. The polarizers are reflecting the horizontal component of the polarized light and transmit the vertical component. Each of the linear polarizers has an incident beam angle of 72 degrees. The laser beam in this setup is linear horizontally polarized. By setting the half wave plate to a particular angle, the polarization of a certain percentage of the photons in the laser beam is rotated to linear vertical, so that after propagating through the wave plate the laser beam will contain both vertical and horizontal polarization components. The vertical polarization component of the laser beam is transmitted through the polarizer plates and is blocked with beam blocked. The rest of the laser beam, which is linear horizontally polarized, will propagate through the attenuator. Thus, changing the rotation angle of the half wave plat allows to control the intensity of the horizontal component of the linear polarized laser beam[1]. Since the gas cell is mounted inside a vacuum chamber, the laser pulses have to pass through an entrance window of the vacuum chamber. The entrance window is anti-reflection coated for 800 nm. To control the geometrical phase mismatch in the HHG process, the lens has been mounted on a translation stage, which allows to change the position of the focus over a length of 40 mm ($1\,\mu$m step size) relative to the gas cell. Furthermore, two apertures are mounted before and after the lens for alignment purposes.

The gas cell is made out of stainless steel and can have different lengths of $5.5, 7.5$ and 10 mm (Fig.3.2). It is sealed with 0.1 mm thick copper foils from both sides in order to control the gas flow and pressure. The focused laser pulses can drill holes through the foils in order to prepare their own beam path. The gas is flowing into the cell through a stainless steel pipe which is also holding the gas cell. The other end of the pipe is connected to a gas pressure reducer. The position of the gas cell can be adjusted along three axes by means of a manipulator mounted on top of the HHG chamber. In order to regulate the flux and pressure in the gas cell, a flux meter [2] is used which enables a controlled gas inlet flux down to 10^{-6} mbar l/s. Depending on the gas which is used to generate the high harmonics, the optimal pressure in the gas cell can be different. For instance, the optimal pressure for Ar in the gas cell is measured to be 19 mbar whereas, the optimal gas cell pressure for Xe is about 3 mbar. The discussion how an 'optimal' operation is defined can

[1]The attenuator is a product of the Altechna company.
[2]Pfeiffer Vacuum Gas Dosing Regulating Valve EVR 116.

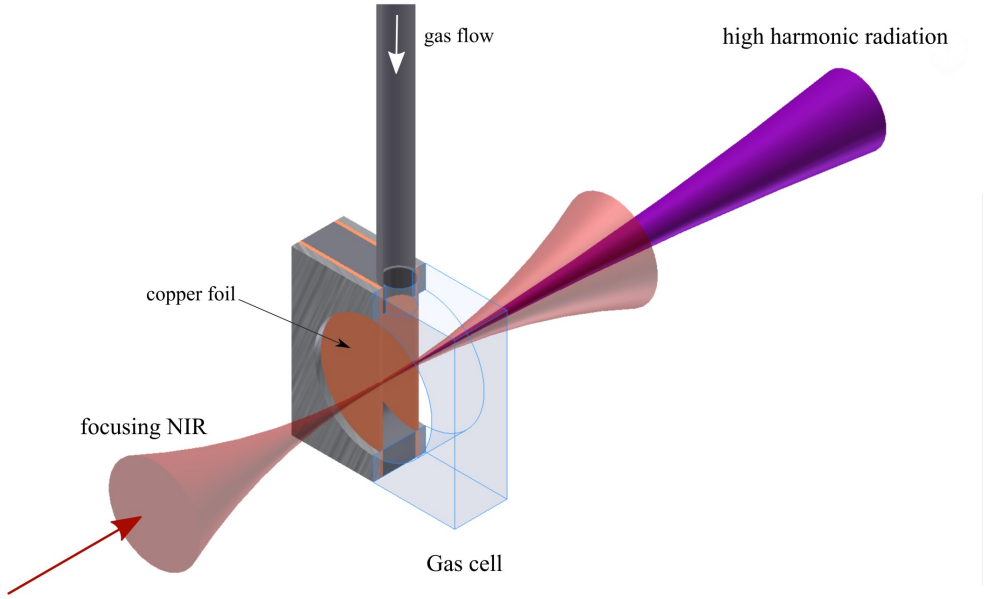

Figure 3.2: A view trough the gas cell: The gas cell consists of a stainless steel frame which is sealed with copper foils from both sides. The length can be chosen between 5.5, 7.5 and 10 mm. The gas is flowing through a pipe from the top in to the cell. The focused laser beam is drilling a hole in the copper foils and interacting with the gas. The pressure in the cell can be controlled by regulating the gas flow. This is done by means of a flux meter.

be found below. The background pressure in the HHG chamber for both gases is about 3.1×10^{-3} mbar (see section 3.3).

After the gas cell, the generated VUV pulses will co-propagate with the fundamental laser pulses through an aluminum filter [3][102]. The 150 nm thick aluminum foil of the filter has an approximate transitivity of %1 for NIR pulses. The transmission of VUV pulses with photon energies between 20 to 60 eV is $70\% - 80\%$. The filter is placed between two apertures, which limit the spot size of the NIR beam on the filter to avoid any damage due to heat load. The yield of the transmitted VUV pulses can be detected by a photodiode [4] which is mounted on a manipulator and can be moved into the VUV beam to measure the intensity (see Fig.3.1). The HHG pulses are focused into the interaction region in the experimental chamber by means of a toroidal mirror. The gold coated surface of the toroidal mirror enables an optimal reflection of photons in the energy region of 20 to 100 eV with an incident angle of 72 degrees. The mirror has a focal length of 500 mm for an object distance of 2000 mm which equals the distance between the HHG gas cell

[3] Aluminum foil on mesh with a diameter of 10 or 15 mm from Lebow company [102].
[4] AXUV 100G from EQ photonics.

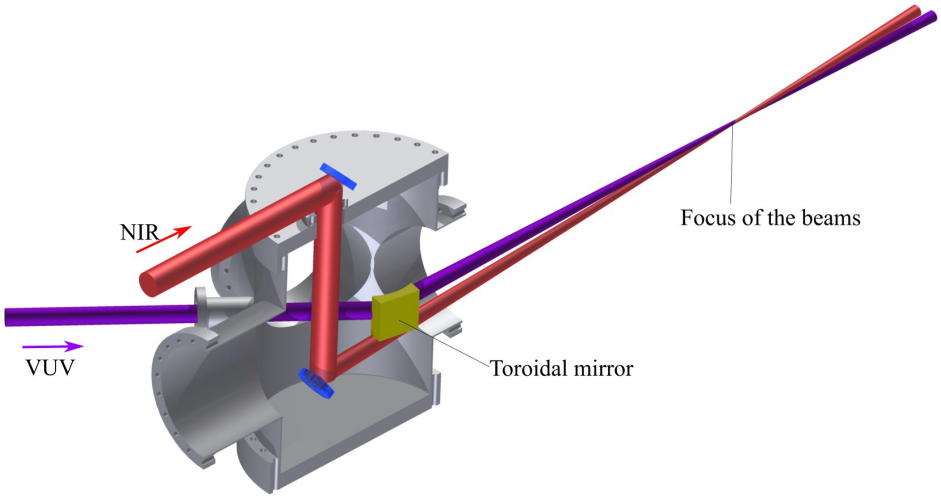

Figure 3.3: The VUV radiation is focused by a toroidal mirror into the interaction region. The NIR laser beam is propagating almost coaxially with the VUV beam such that the focal spot of the two beams are overlapped in the interaction volume.

and the mirror. The focal spot size produced by the mirror was measured to be about 50 μm.

The second part of the laser beam, which is transmitted through the beam splitter propagates towards a delay stage. The delay stage[5] has a total travel distance of 150 mm (1 ns in time scale) and a minimum step size of 0.1 μm. The minimum step size is giving the minimum possible delay of 0.7 fs, which can be generated between the two pulses in the different beam paths and is for the present setup 0.7 fs. The NIR pulses are then focused by a lens of 1000 mm focal length and entering the recombination chamber through a coated window. It is reflected into the interaction region in the experimental chamber such that the NIR beam is propagating quasi-coaxially (with an angle of about 3°) with the VUV radiation (Fig.3.3). The spatial overlap of the beams in the interaction region can be monitored by using a YAG screen and a camera. The YAG screen is mounted on a manipulator allowing to move the screen into the interaction region.

The target gas for the pump-probe experiment, is injected either by a gas needle for an effusive gas injection or by a super sonic gas jet. The gas jet is produced by using a pulsed valve [103] and a skimmer [104] in combination with two turbo-molecular pumps[6]. The jet valve can be synchronized to the laser pulse and enables to probe a high density of gas in the interaction region. The advantage of the pulsed gas jet (with respect to a continuous gas flow) is that the background pressure in the chamber stays in the high vacuum region. Whereas, the gas needle enables a

[5]Newport company, High Precision Linear Stage, 150 mm Travel, GTS Series.
[6]Pffeifer vacuum, HiPace 700 M mit TM 700, DN 160 ISO-F.

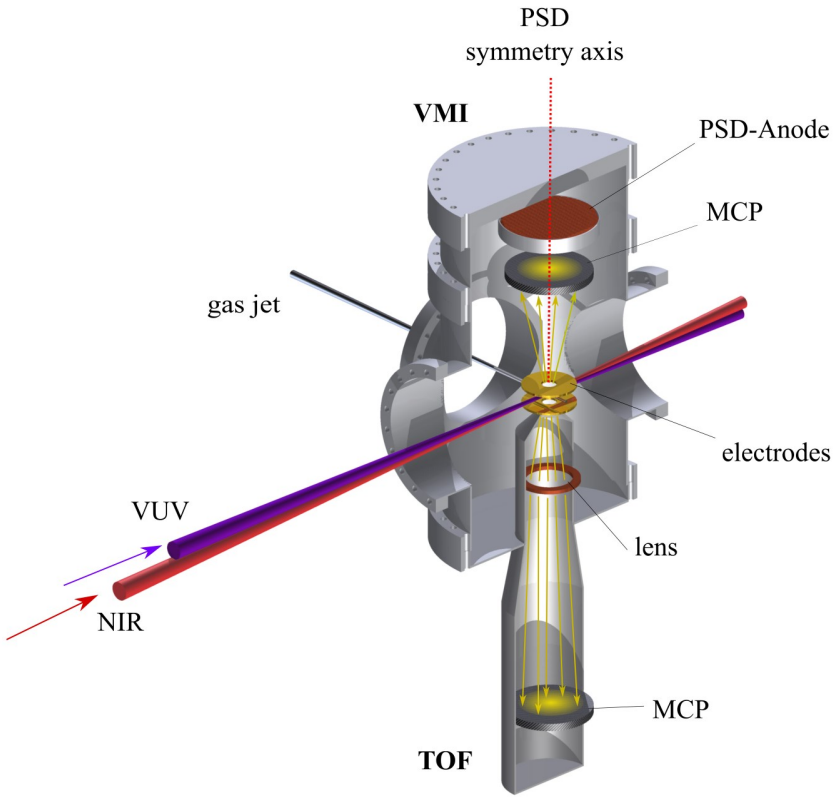

Figure 3.4: The experimental chamber with the VMI spectrometer mounted on top and the TOF spectrometer mounted on the bottom (see the text).

constant gas flow, but lower gas density in the interaction region. This arrangement is useful for optimization measurements at the beginning of the experiments.

In order to detect and analyze the charged particles produced by the interaction between the gas and the focused beams, two types of spectrometers have been used. The first one is a time of flight spectrometer (TOF) installed at the bottom of the experimental chamber and the second is a velocity map imaging spectrometer (VMI) mounted in the upper half of the chamber (see Fig.3.4). The spectrometers are explained in more detail in the following part of the chapter.

3.1.1 Time-of-Flight Spectrometer

The time-of-flight spectrometer (TOF) is a commonly used spectrometer for photoionization experiments with pulsed light sources [105, 106]. The first spectrometer of this kind was proposed by Stephens in 1946 [107]. The TOF spectrometer in the present setup can be used either as an electron or as an ion mass spectrometer [108, 109]. However, in the scope of this thesis it was only used in electron counting mode. Here, the produced electrons in the interaction volume travel through a drift tube towards a multichannel plate (MCP) where their arrival time is recorded. In

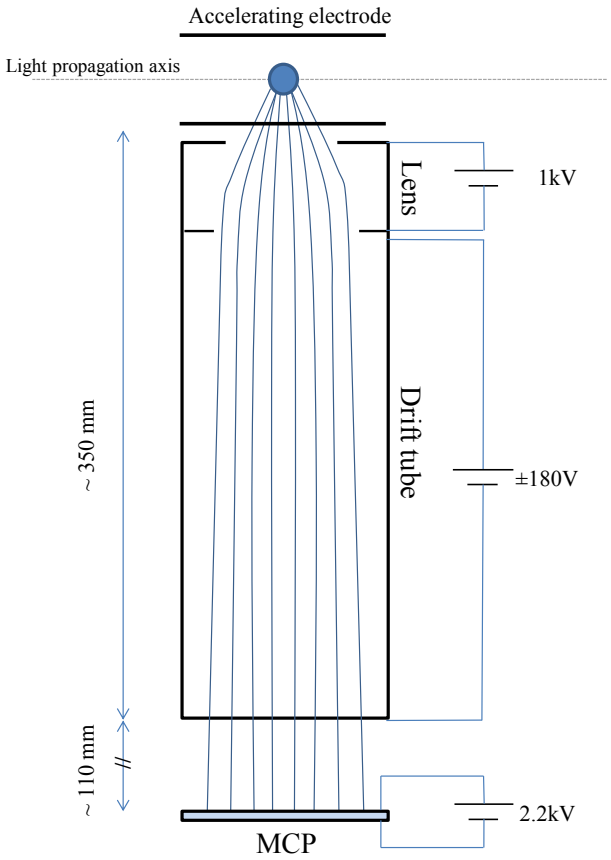

Figure 3.5: A schematic sketch of the structure of a TOF used in the laser lab. A homogeneous electric field applied to the interaction region can accelerate the charged particles toward the MCP. The voltages in this figure are set for the electron mode of the TOF spectrometer [110].

some advanced TOF spectrometers such as the one employed here, there is an additional extraction module (Lens) [105, 110], which enables to collect more electrons by collimating them towards the MCP (Fig.3.5). The higher collection efficiency allows for better statistics, however, compromises the energy resolution.

Considering an electron released in the interaction region at time t_0, which moves towards the MCP and is recorded at a certain time (t), the flight time of the electron ($t - t_0$) is related to it's kinetic energy:

$$t - t_0 = \left[\frac{m_e d_{eff}^2}{2eE_{kin}}\right]^{\frac{1}{2}}, \tag{3.1}$$

where d_{eff} is the effective distance between the interaction region and the MCP. The time t_0 is triggered by the laser and is the arrival time of each light pulse in the interaction region.

The photoelectrons produced in an ionization process evolve in a 3D emission

pattern. The number of photoelectrons collected by the TOF is limited by the diameter of the entrance of its drift tube (entrance aperture). The TOF used in the HHG setup is a Wiley-McLaren based spectrometer with an entrance aperture diameter of 7 mm and an acceptance angle of 30° (full angle) [111]. The spectrometer setup allows to be used either as an electron TOF spectrometer with a time of flight resolution of $\frac{T}{\Delta T} > 100$ or as a time of flight mass spectrometer with a mass resolution of $\frac{m}{\Delta m} > 300$. The minimum kinetic energy of the photoelectrons, which can be analyzed is specified to be about 5 eV. Under the current experimental conditions, it is expected that the TOF is able to detect photoelectrons with kinetic energies less than 5 eV. The drift tube of the TOF has a length of 354 mm and therefore, the distance between the interaction region and the TOF detector is relatively short. The maximum potential difference, which can be applied to the ends of drift tube in electron-mode is −180 V, so fast electrons can be decelerated. The TOF in this setup was used to optimize the HHG radiation by monitoring the photoionization process induced by the HHG. As a first showcase, the HHG radiation was used to ionize argon atoms. The maximum kinetic energy of the photoelectrons is less than 50 eV which are detected by the TOF spectrometer. Subsequently, the TOF signal is magnified through a wideband, low noise amplifier, discriminated by a constant fraction discriminator (CFD, typically with a threshold of $\sim$ 200 mV and a pulse output width of $\sim$ 50 ns) and digitized by a time-to-digital converter (TDC) with a time resolution of about 60ps [112]. In this scheme, each pulse of the laser can produce one electron count with a given time information. The acquired counts are then accumulated in a time histogram that becomes the spectrum. In order to obtain the order of the high harmonics, it should be possible to read off the photon energy of each peak. Therefore, the photoelectron time-spectrum has to be converted to an energy-spectrum. The time to energy conversion of the time axis (t) in the photoelectron spectrum can be done by using the following equation:

$$E = \frac{m_e d_{eff}^2}{2(t - t_0)^2}, \tag{3.2}$$

where m_e is the mass of an electron and d_{eff} is the effective distance the photoelectron has to travel from the interaction region towards the MCP of the TOF. t_0 is the zero point of the time axis in the time-spectrum. After converting the photoelectron spectrum to the energy scale, the spectral features have to be quadratically scaled, in order to maintain the correct area under the peaks. Therefore, the yield axis in the photoelectron time-spectrum (Y_t) has also to be rescaled (Y_E). This can be done by taking in to account that the area under the peaks before and after the conversion should not change ($\int Y_E dE = \int Y_t dt$). The rescaling of the photoelectron yield (Y_t to Y_E) is can be done by using the following equation 3.2:

$$Y_E = Y_t \frac{(t - t_0)^3}{m_e d_{eff}^2}. \tag{3.3}$$

3.1.2 Velocity Map Imaging Spectrometer

A velocity map imaging spectrometer (VMI) allows the simultaneous measurement of the angular distribution and kinetic energy of the photoelectrons or ions. One of the important characteristics of this spectrometer is its 4π collection efficiency. This spectrometer become a widely established tool used for the investigation of photoionization and photodissociation dynamics of atomic and molecular targets [113, 114, 115, 116] since its first introduction in 1997 [117].

The basic idea of a VMI is to project the 3D spatial distribution of the charged particles onto a position sensitive detector (PSD). The charged particles are accelerated towards the detector with an inhomogeneous electric field applied by means of two electrodes mounted above and below the interaction region (see figure 3.6). In the SQS-setup the PSD is mounted such that its symmetry axis is perpendicular to both the linear polarization axis and beam propagation axis of the beam. One advantage of this structure is its ability of mapping all particles with the same velocity to points with the same radial distance from the center of the PSD, independent from their initial position in the interaction region. As long as the emission angle of the particles relative to the symmetry axis of the PSD (elevation-angle ϕ) is nonzero, the velocity of particles can be mapped through their position on the PSD. This leads to a 2D projection of the angular distribution of the charged particles on the detector. The arrival position of each particle on the PSD is defined through the parameters R and an angle θ in a polar coordinate system, where R is the distance to the symmetry axis of the PSD and is different for particles with different kinetic energy:

$$E_k = \frac{1}{2} m\, v^2 \sim R^2. \tag{3.4}$$

The angular distribution of the charged particles is cylindrically symmetric around an axis. In case of a linear polarized light field the symmetry axis is the polarization axis and for circularly polarized pulses it is the propagation axis of the light pulses. The angle between the emission direction of the particles and the beam propagation axis is called the azimuthal angle which is equal to the angle θ projected on the PSD. The 3D distribution can then be calculated from the 2D projection through a mathematical process called inverse Abel-Transformation [113].

There are different types of position sensitive detectors. One kind is consisting of an MCP, a phosphor screen and a CCD or sCMOS camera [117]. The MCP amplifies the detected electrons and creates an electron avalanche which is accelerated towards the phosphor screen where it induces light emission. This emission shows the arrival position of the charged particles via visible light and is then recorded through the camera. The main advantages of this type of PSD is the high spatial resolution, which is limited by the pore size of the MCP and consequently, the width of the electron avalanche arriving at the screen. However, the disadvantage is the timing resolution which is limited by the phosphorescence life time of the phosphor screen (ms) and the time resolution of the camera as well as applications

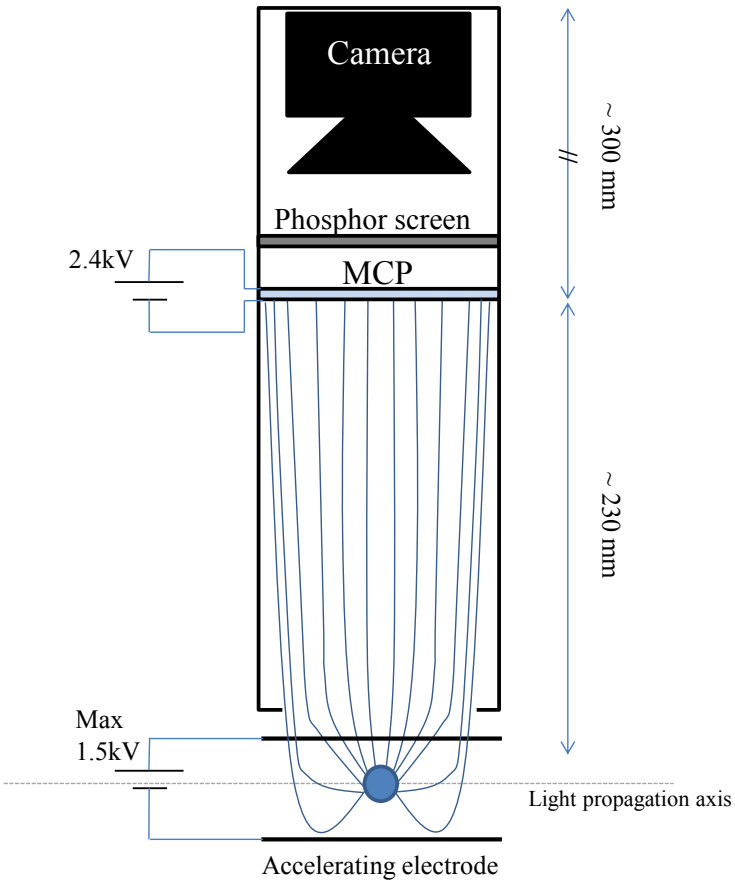

Figure 3.6: A schematic sketch of the structure of the VMI. The inhomogeneous electric field between the electrodes projects the 3D distribution of the photoelectrons onto the position sensitive detector [110].

of high repetition rates $\gg$ 100 Hz.

In other investigations such as coincidence experiments, it is important to correlate the position of a particle to the arrival time of another particle on the same or a different detector. Therefore, different kinds of detectors have been developed, which make use of split anodes or delay line anodes [118, 119, 120] instead of the phosphor screen and camera combination. The basic principle of delay line detector is to have three long wires, where each of them is crossing a given plane many times (Fig.3.7). Each wire is on a different plane and are installed on top of each other, as shown in figure 3.7. Once an electron hits a certain channel of the MCP, many electrons are released from the channel and move towards the delay lines. If the electrons hit the wires, a current can be measured at the start and the end of each delay line. Depending on the hit position along the wire, a time delay can be

measured between the signals arriving on the two ends of each wire. Out of the time delay between the signals of two ends of the wires, position and the arrival time of the electrons can be calculated. This can be done by using only two delay lines. However, the signals of the third delay line are used as a redundant source of information for the cases when the signal is lost due to non perfect electronic conditions or simultaneous events. The time resolution of this PSD type is in the order of few nanoseconds. However, the number of particles, which can be detected simultaneously is limited by the time resolution of the delay line PSD (less than 1 ns) and the recovery time of the electronics (in the order of ns) [112]. Therefore, in experiments with intense light sources such as FELs, it might be difficult to record the position of all produced particles due to the interaction of a high number of photons in a pulse with a gas sample [114, 115].

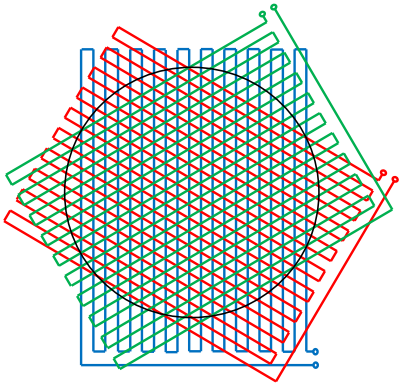

Figure 3.7: A schematic sketch of a three dimensional delay line PSD. The three wires (green, red and blue) are crossing through three parallel planes, where one is on top of the other. The electrons released from the interaction region are moving towards the PSD perpendicular to the plane of the figure. The time delay of the signals at the start and the end of the wires gives information about the hit position and the arrival time of the electrons.

A general limitation of the VMI spectrometer is the range of the kinetic energy of the particles, which can be acquired [121, 122]. This limit is given due to the defined diameter of the MCP and the voltage limit, which can be applied to the electrodes to accelerate the charged particles with a high kinetic energy towards the detector. The smaller the diameter of the PSD, the higher the voltage has to be to bent the travel way of the charged particles to hit the PSD.

The SQS-VMI spectrometer in the HHG setup at the laser lab is consisting of an MCP with a diameter of 120 mm and three anode delay lines. The time resolution of the delay lines for each event is about 1 ns. The voltage limit, which can be applied to the electrodes in the interaction region is about 3 kV. The spectrometer is able to detect electrons with a maximum kinetic energy of 150 eV and ions with

kinetic energies up to 40 eV.

In the context of this chapter, only the TOF spectrometer was used (in the electron-mode). Principally, the two spectrometers can be used in coincidence to analyze photoelectrons and ions produced in the interaction of both VUV and NIR pulses with a sample gas.

3.2 High Harmonic Generation

The ionization process of an atom in a light field is strongly depending on the electric field intensity, central frequency of the photons ω_0 (photon energy $\hbar\omega_0$) and the atomic ionization potential I_p. For instance, a photoionization process can take place in a weak electric field with a photon energies higher than the binding energy of the target atom or molecule. Opposed to that, the ionization of atoms by an optical laser with low photon energy ($\hbar\omega_0 < I_p$) will appear only in strong fields in form of multiphoton ionization or tunnel ionization.

The high harmonic generation process can be explained by the three-step model in the tunnel ionization regime ($\hbar\omega_0 < I_p < U_p$) [123]. In the first step, the strong electric field of the laser (about $10^{14} W/cm^2$) modifies the Coulomb potential of the atom and enables the valence electron to tunnel through the potential barrier (see Figure 3.8.a).

In the second step, the released electron in the optical laser field gains kinetic energy (Fig. 3.8.b). As the optical pulse is traveling through the interaction medium, the direction (sign) of the electric field changes. Therefore, the freed electron will be accelerated and driven back to its parent ion (Fig 3.8.c). In the third step the electron will recombine with the parent ion and its kinetic energy will be emitted as a photon (Fig 3.8.d). In classical mechanics, a free moving electron in an optical field can be driven back to the parent ion, only if the electric field is linearly polarized [125, 126]. Therefore, the generation efficiency of the high order harmonics depends among other parameters on the purity of the linear polarization of the fundamental laser beam [127, 128].

Every half-period of the laser oscillation the electron gets the chance to tunnel through the atomic potential barrier. In an ideal case, the electron will re-encounter its parent ion after another half cycle of the laser oscillation. The kinetic energy gained by the free electron in the laser field is then set free in form of a photoemission. The kinetic energy, which can be gained by the electron depends on the time when it becomes free (t_0) from the atomic potential. Within every half cycle, this time for each electron escaping its parent atomic potential can be different. Thus, each photon generated in this process is emitted with its individual frequency. Now, the emitted photons can only be odd harmonics of the fundamental laser frequency (ω_0). This results from the fact that the simultaneous conservation of global energy and of global momentum cannot be provided by the absorption of two or any even number of photons [129]. Therefore the frequency of the emitted photons can be

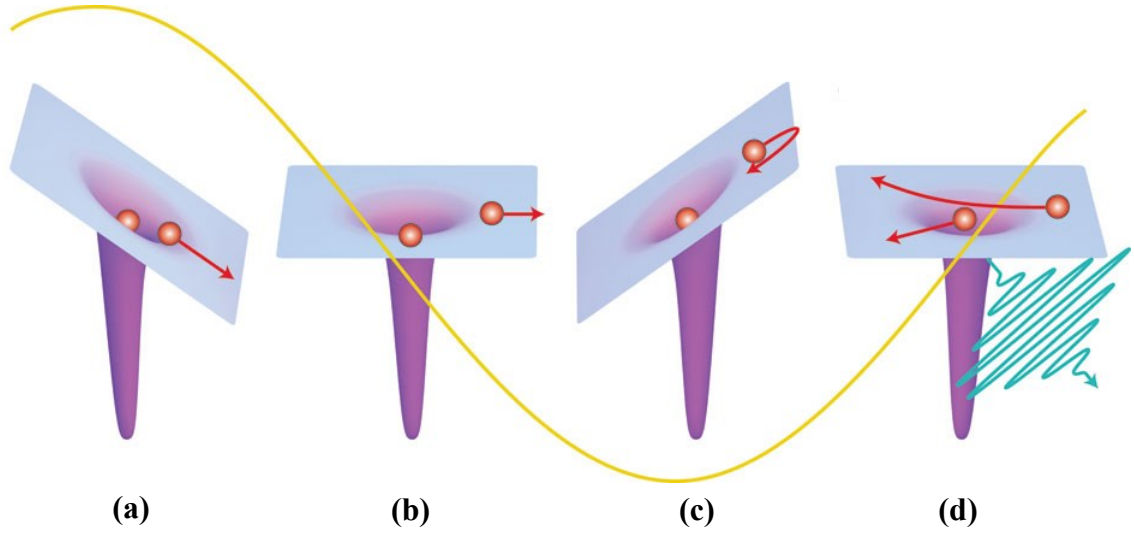

Figure 3.8: The three-step model for the HHG process: (a) In the first step, the oscillating electric field of the beam (yellow curve) modifies the Coulomb potential of the atom, enabling the electron to tunnel through the barrier and escape into the laser field. (b) In the second step, the free electron will gain kinetic energy, due to the strong optical field. (c) The electron is driven back to its parent ion while the sign of the field changes. (d) In the third step, the electron recombines with the parent ion, emitting a high harmonic photon with an energy equal to the kinetic energy of the electron gained in the field plus the ionization potential of the atom [124].

defined as:

$$\omega_q = q\,\omega_0, \tag{3.5}$$

where $q = 2n + 1$ is the harmonic number. The individual frequencies of the emitted photons results in a spectrum of different harmonics. The highest harmonic frequency appears when the freed electron has the longest trajectory in the laser field and gains the highest possible kinetic energy. The maximum energy is related to the ponderomotive potential by a factor of 3.17 and can be calculated from the following equation [60, 100, 129]:

$$\hbar\omega_{max} = I_p + 3.17U_p \propto I_L\omega_0^2, \tag{3.6}$$

where ω_{max} is referred to as the cut-off frequency. The highest order harmonic is also often called the cut-off harmonic. From equations 3.5 and 3.6 the cut-off harmonic can be calculated from the following equation:

$$q_{max} = \frac{I_p + 3.17U_p}{\hbar\omega_0}. \tag{3.7}$$

The cut-off order harmonic can be extended to higher orders with an increase of the ponderomotive potential U_p, according to equation 3.7. This is done by increasing the peak intensity of the laser field or its wavelength. The required peak intensity for the generation of high order harmonic radiation in a rare gas medium is in the order of 10^{14} to $10^{16}\,W/cm^2$ [96, 130]. On the other hand, a much higher intensity will reduce the probability of the recombination process as the magnetic component of the laser field becomes large enough that the electron will accelerate in a spiral trajectory and the probability of a recombination with the parent ion will be reduced [55]. The order of the cut-off harmonic can also be increased by using atoms with a higher ionization potential. However, the efficiency of the production of high order harmonics can be lower for atoms with higher ionization potentials.

The HHG process is a highly non-linear process which cannot be completely explained by the three-step model. For instance, the radiated high frequency pulses in this process are coherent and co-propagating with the fundamental laser beam. In the next section the propagation properties of high frequency pulses are approached in more details.

3.2.1 Phase Matching and Coherence in HHG

In the HHG process, each laser pulse traveling through the gas medium ionizes a large number of atoms. In quantum mechanics, each electron freed by tunnel ionization at a certain time t_0, is considered as a wave packet oscillating with an individual frequency. The frequency of this electron depends on the strength and the phase of the laser electric field at t_0. Considering a large number of atoms distributed in space at the focal region of the fundamental laser, a large number of electron wave packets will be accelerated into the continuum and back towards their parent ions. Therefore a large number of high harmonic photons are emitted at a certain harmonic order and result in an HHG wave front with a certain phase. The HHG wave front will appear only when all emitted photons are interfering constructively at the end of the gas medium. This happens when the emitted photons are in phase with the fundamental laser wave front. The phase difference of the harmonic photons ($\Delta\phi$) is related to the constant difference of their wave vectors (Δk) as the following:

$$\Delta\phi = z\Delta k, \tag{3.8}$$

where z is the propagation distance of the photons and Δk is called the phase mismatch. For the q^{th} harmonic at a given distance the phase mismatch is [131]:

$$\Delta k_q = k_q - qk_0, \tag{3.9}$$

where k_0 is the wave vector of the fundamental laser. The recombination of the electrons and ions at different positions in the focal region and the emission of constructively interfering photons results in a spatially coherent HHG radiation. A perfect phase match happens if $\Delta k_q = 0$.

In a realistic case, a large number of atoms are interacting with the laser beam practically at the same time. Each atom is surrounded by other atoms as well as ions and free electrons produced by the tunnel ionization process. Therefore, in the propagation of photons through this medium not only the refraction index of the gas medium [132] but also the ions and electrons are affecting the wave vectors (dispersion in the plasma) [133]. Moreover, by focusing the laser beam with a lens, the wave front and the phase of the laser will be changed. This geometrical change in the phase of a Gaussian beam is called the Gouy phase shift [131, 134]. Furthermore, the distance over which the wave fronts stay in phase is given by the length of the gas medium [135], which is again limited by the coherence length (L_{coh}). From equation 3.8 the coherence length can be defined by the following equation:

$$L_{coh} = \frac{\pi}{\Delta k}. \tag{3.10}$$

To achieve a maximum yield of the harmonics, all these parameters have to be controlled under the experimental conditions such that the phase mismatch is reduced to a minimum [136]. Considering equation 3.10, for a given length of the gas medium (L_{med}) the following condition has to be fulfilled:

$$\Delta k \, L_{med} < \pi \, . \tag{3.11}$$

The typical length of the gas medium is between 2 and 15 mm depending on the experimental setup. Under experimental conditions the effect of the geometrical phase mismatch and the propagation distance in the gas medium as well as the refraction index of the medium can be controlled by varying the position of the focus in the gas medium, changing the length of the medium and changing the pressure of the gas in the medium. These parameters have to be set such that the high harmonic yield approaches its maximum possible value at the end of the gas medium.

In the context of this work, the generation of high order harmonics has been realized by setting up a laser system in the laboratory of the SQS research group at the European XFEL. Thereby, different parameters of the HHG such as gas pressure, focus of laser in the gas cell, length of the medium and the laser power were optimized to tune the HHG radiation to its maximum yield. In the following sections the results of tuning the HHG are briefly described.

3.3 Characterization of HHG

The intensity of different harmonics is affected by the phase mismatch, as it was discussed in the previous section. The highest intensity at different photon energies of the harmonics can be reached by optimizing parameters such as laser focal spot size in the gas cell, focal intensity in the gas cell and the gas pressure. In this section, the dependency of the harmonic intensities on these parameter will be

discussed.

Generally the intensity of all high harmonics (overall intensity) can be measured by special photodiodes (e.g. XUV-photodiodes) [137]. In the commissioning of the SQS-HHG setup, the high harmonic pulses were used to ionize Ar atoms. The kinetic energy of the photoelectrons is given by the difference between the absorbed high harmonic photon energy and the binding energy of 3p electrons in Ar. The photoelectrons are detected by means of a TOF spectrometer. The photoelectron yield is related to the ionization cross section at the photon energy of the corresponding harmonic and its intensity.

Table 3.1: The right column in this table shows the cut-off harmonic order ($H_{Cut-off}$) for different gases Ar, Kr, and Xe. For each gas, the lowest binding energy (E_b), optimal pressure (Opt. P) in the gas cell and optimal pulse energy (Opt. E_{pulse}) for generating the 21^{th} harmonic are listed in this table.

Gas	E_b	Pressure	Pulse energy	$H_{Cut-off}$
Ar	15.8 eV	19 mbar	1.1 mJ	$H27$
Kr	14.1 eV	8.3 mbar	1.1 mJ	$H25$
Xe	12.1 eV	2.86 mbar	1.0 mJ	$H23$

Figure 3.9 shows the photoelectron spectrum on a photon energy scale after conversion from the time scale. The 11^{th} harmonic of the fundamental laser (photon energy =1.55 eV) is the lowest harmonic with enough photon energy (17.05 eV) for ionizing the outer 3p electrons of Ar atoms (I_p = 15.8 eV, which is the binding energy averaged over the two spin-orbit components $^2P_3/2$ and $^2P_1/2$.) Fig. 3.1. In figure 3.9, we suppose that the first harmonic is the 11^{th} harmonic, since it is expected that the TOF spectrometer is able to detect the photoelectrons corresponding to this harmonic. However, since an absolute calibration of the TOF spectrometer was not done here, it might be that the lowest harmonic peak represented in the spectrum of figure 3.9 is the 13^{th}.

In order to reach the highest possible harmonic photon energy and the corresponding cut-off frequency, the HHG has to be optimized. From equation 3.7 the ionization energy of the gas used to generate high harmonics is a relevant parameter for tuning HHG. Therefore, in the context of this work, Argon, Krypton and Xenon were used to optimize the HHG and to compare the cut-off frequencies.

Therefore following parameters have to be set to an optimal value:

- Position of the laser focal spot with respect to the gas cell,
- Gas pressure in the gas cell,
- Laser pulse energy,
- Length of the gas cell,

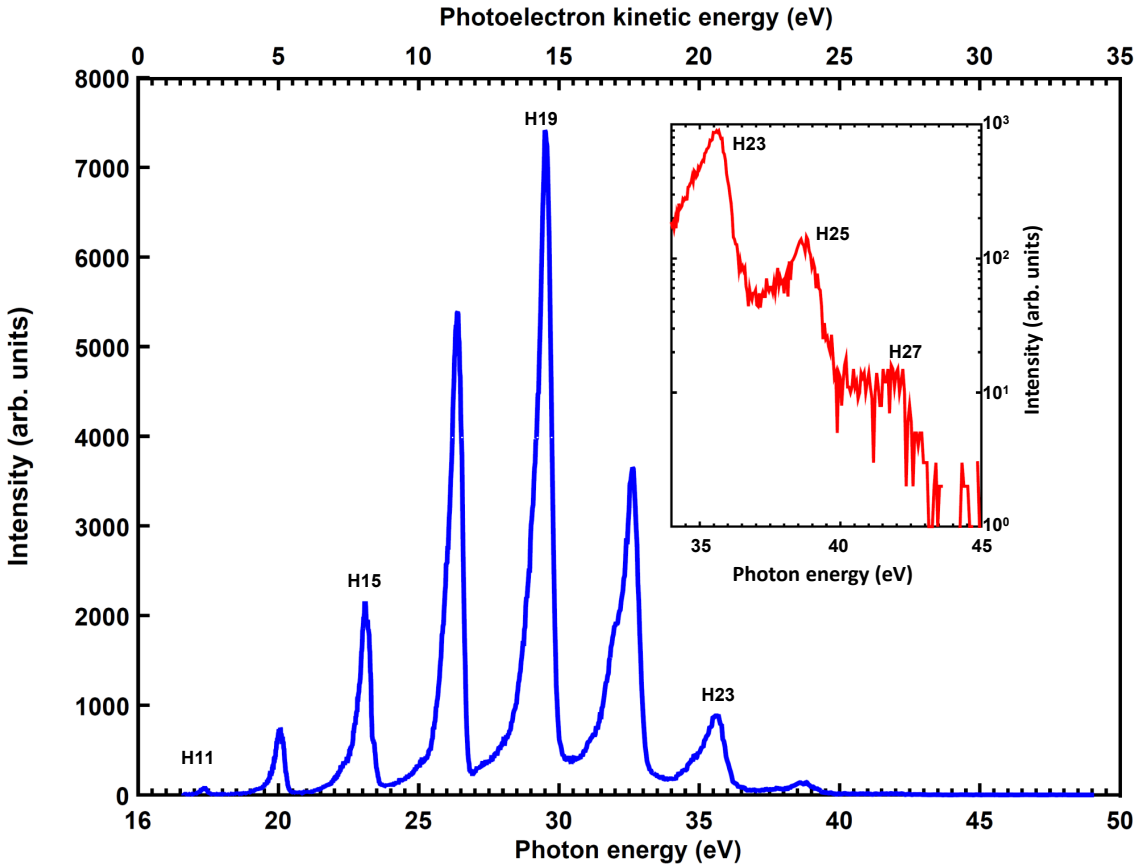

Figure 3.9: Photoelectron spectrum produced by the interaction of high harmonics generated by focusing an intense optical laser into a rare gas (Ar) medium (laser photon energy = 1.55 eV). The photoelectrons resulting from this process are collected by an electron TOF spectrometer. The first peak at 17.05 eV (photon energy) is the photoelectron yield corresponding to the 11th harmonic (H11). The cut-off energy for the high harmonics is at about 42 eV which correspond to the 27^{th} harmonic (see H27 in the inset). The inset shows the 23^{th} to 27^{th} harmonics in a logarithmic scale of the intensity.

- Chirp of the laser pulses.

In order to find the best value for each of these parameters, the other parameters have to be set to a fixed value. This was done in three steps. In the first step, the pressure of Ar in the gas cell was fixed to 19 mbar and the pulse energy was set to 1 mJ to find the optimal focal spot position relative to the gas cell. Changing the position of the lens and acquiring the photoelectron spectrum, the dependence of the photoelectron yield corresponding to each harmonic intensity can be recorded. After normalizing the photoelectron yield by the ionization cross section of Ar 3p electron, the variation of harmonic intensities with the position of the focal spot respective to the gas cell can be illustrated as shown in figure 3.10.

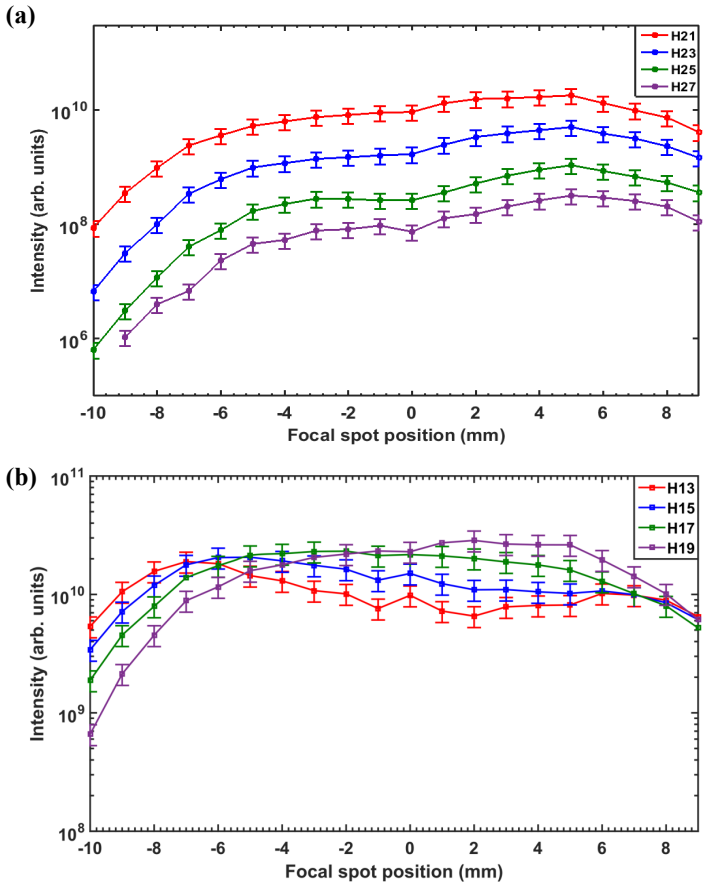

Figure 3.10: The variation of the harmonic intensities (in Log. scale) with changing the focal spot position of the laser relative to the midpoint of the gas cell. (a) The intensity of the 21^{th} to 27^{th} harmonics is maximum at +5 mm (before the gas cell). (b) The different behavior in the intensity variation of the 13^{th} to 19^{th} could be either explained by the different phase matching of the harmonics or might also be due to the Coulomb force of the ions produced in the experimental chamber, which could be large enough to retard photoelectrons with a lower kinetic energy and decrease their counts in the TOF spectrometer (see text).

The lens was moved along the beam axis and so the focal spot position could be scanned along the gas cell length. The zero on the focal spot position axis in figure 3.10 is corresponding to the middle of the gas cell length. Positive values on the focal position axis correspond to the case when the laser beam is focused before propagating through the midpoint of the gas cell.

The intensity variation of the 11^{th} harmonic was not included due to a low count rate in comparison with the background signals of the TOF. The intensity of the 13^{th} harmonic achieves it's maximum at two different focal points. A major maxi-

mum at +7 mm and a minor maximum at −7 mm on the two sides of the gas cell can be observed. One argumentation could be that the phase mismatch for the 13^{th} harmonic is minimum at these two focal positions. The maximum intensity for the 15^{th} and 17^{th} harmonics can be achieved at a focal spot position of −6 mm and −2 mm respectively. As it can be seen in figure 3.10, when the laser pulses are focused before the gas cell (+2 to +5 mm) the intensities of the $21^{th} - 27^{th}$ harmonics rise to a maximum value. Therefore, under the given conditions, in order to produce intense high order harmonics, the best phase mismatch is achieved when the beam is focused before entering the gas cell (at +5 mm). However, the harmonics 13^{th} and 15^{th} show a totally different behavior. In their case, the intensity is not maximum at focal position +5 mm. At this position, the harmonics generated in the gas cell radiate with the highest intensity. Therefore, a large number of ions are produced in the interaction of the harmonics and the gas in the experimental chamber. The unusual behavior of the 13^{th} and 15^{th} harmonics could be interpreted in two different ways. The first way is that the phase matching of the photons at theses harmonics are worse in comparison to the higher order harmonics. Another explanation could be a detection issue of photoelectrons in the spectrometer, which appears due to the attractive Coulomb force of the large number of ions, retarding the relatively slower photoelectrons. The photoelectrons produced by the absorption of the 13^{th}, 15^{th} and 17^{th} harmonics have a kinetic energy of 4.35, 7.45 and 10.55 eV, respectively, which might be retarded by the Coulomb force of the ions in the interaction region. The kinetic energy of photoelectrons produced by the 19^{th} to 27^{th} harmonics (13.56 eV to 26.05 eV) are considerably larger and therefore, not affected. In the following, a similar behavior in the intensities of the lower harmonics can also be seen in the pressure scan and the pulse energy scan of the laser.

The second step for tuning HHG is to optimize the pressure of Ar in the gas cell. This procedure was done by gradually changing the gas cell pressure and acquiring the photoelectron spectrum. Varying the gas pressure in the gas cell, leads to a change of the gas density in the focal region of the laser beam and therefore to a change of refraction index in the gas medium. Through the variation of the refraction index the phase mismatch can be changed and therefore the harmonic intensities can be adjusted. The result of these scans is shown in figures 3.11.a and 3.11.b. The intensity of the 19^{th} harmonics shows an almost flat behavior in the pressure regions between 12 mbar and 23 mbar. The intensities of the 21^{th} to 27^{th} harmonics are highest in the pressure region between 17 mbar and 19 mbar (Fig.3.11.b). However, the harmonics 13^{th} to 17^{th} show a totally different behavior. In their case, the intensity is minimum in the pressure region 17 - 19 mbar. This behavior could again be due to the different phase matching of these harmonics or might be caused by the attractive Coulomb force of the large number of ions, decelerating the slower photoelectrons corresponding to these harmonics.

Considering the 21^{st} to 27^{th} harmonics, a clear decrease of the intensities can be seen in the high pressure regions after the maximum ($19 - 25$ mbar). This decrease

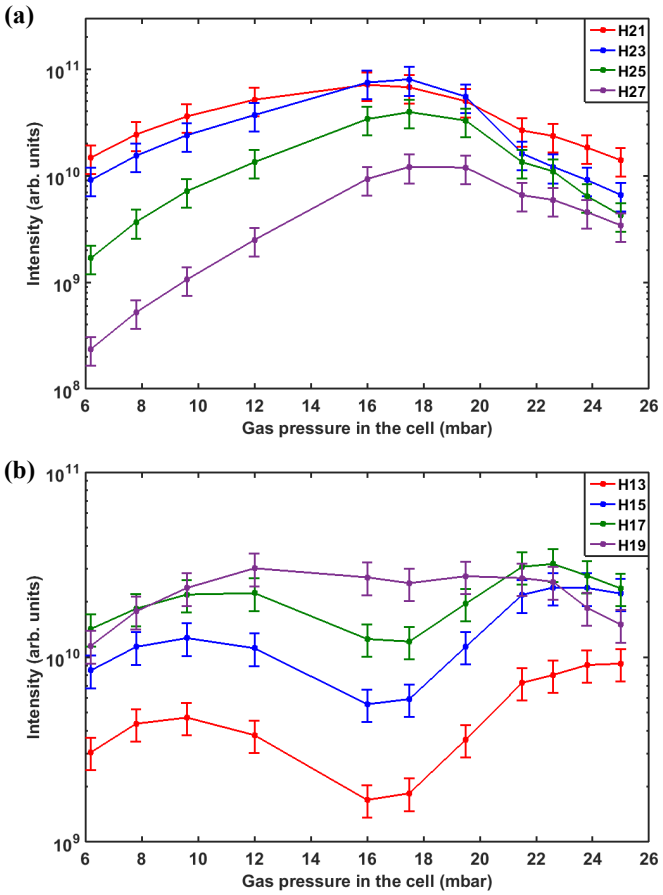

Figure 3.11: The variation of the harmonic intensities (in Log. scale) with the change of the pressure. (a) The optimal gas pressure region for the 21^{th} to 27^{th} harmonics is in the pressure region $17-19$ mbar. (b) The intensity of the 13^{th} to 17^{th} harmonics is decreasing to minimum at the same region ($17-19$ mbar). This different behavior in comparison to the harmonics in (a) might be either due to the different phase matching of the harmonics or it could also be due to the Coulomb force of the ions produced in the experimental chamber, which could be large enough to retard photoelectrons with a lower kinetic energy and decrease their counts in the TOF spectrometer (see text).

of intensities can be explained by the fact that the high frequency photons can be reabsorbed in the gas medium when the density (pressure) of atoms increases. This decrease of intensity cannot be seen for the 13^{th} to 17^{th} harmonics due to the reason explained before.

In the third step, the intensity dependence of the harmonics to fundamental laser pulse energy was observed. From equations 2.5 and 3.7, it is known that the ponderomotive potential is directly related to the laser intensity and the maximum

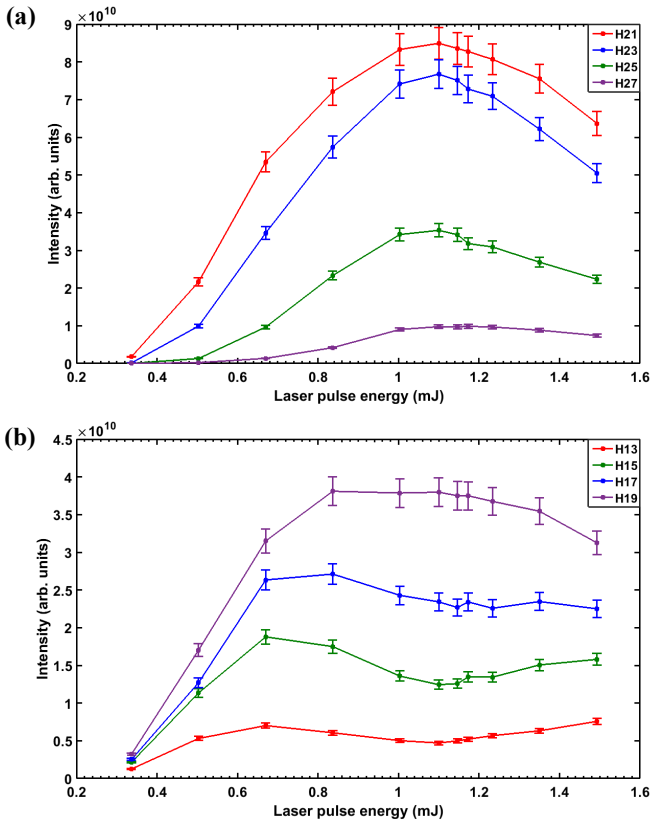

Figure 3.12: Variation of harmonic intensities by changing the laser pulse energy: The intensity-axis is in logarithmic scale. (a) the optimal pulse energy for the 21^{th} to 27^{th} harmonics is 1.1 mJ. At pulse energies higher than 1.1 mJ the intensity of the harmonics 19^{th} to 27^{th} is decreasing rapidly. This effect is due to rising probability of ionization. In this cases the probability of the recombination of the electrons and their parent ions will decrease quickly. (b) In case of 11^{th} and 17^{th} harmonics the intensities are minimum at pulse energies between 1 and 1.2 mJ. This might be either due to the different phase matching of these harmonics or it could also be due to the Coulomb force of the ions produced in the experimental chamber, which could be large enough to retard photoelectrons with a lower kinetic energy and decrease their counts in the TOF spectrometer.

order harmonic generated in the HHG process (cut-off order) is also directly related to the ponderomotive potential.

In order to find the optimal laser intensity, the pulse energy of the laser was gradually increased decreasing the initially applied attenuation (see Fig.3.1). The

variation of harmonic intensities by changing the laser intensity is shown in figures 3.12.a and 3.12.b. For our setup, it turns out that the optimal pulse energy of the fundamental laser for the production of 21^{th} to 27^{th} harmonics is 1.1 mJ. As it can be seen in figure 3.12.b, for pulse energies higher than 1.1 mJ, the intensities of the harmonics except the 13^{th} and 15^{th} harmonics are decreasing due to the ionization of Ar atoms in the intense laser field. Here, the increasing pulse energy leads to a growing number of freed electrons in the gas medium due to the tunnel ionization. These electrons can change the diffraction index of the medium and therefore, at high laser pulse energies (here, higher than 1.1 mJ) the intensity of the harmonics will decrease [138].

In case of the 13^{th} to 17^{th} harmonics the released photoelectrons are retarded by the ions so that their count rate in the TOF spectrometer is decreasing at the expected optimal pulse energy of 1.1 mJ. Therefore, the intensity curve for these harmonics does not look like to decreasing at higher pulse energies of the fundamental laser.

The pulse duration of the fundamental laser is another parameter which has to be set such that the chirp of the laser pulse after traveling through the transmissive optical elements is at a minimum. The lowest chirp was achieved at a pulse duration of 21 fs during these experiments. The generation of high harmonics depends also to the length of the gas cell. During the HHG-tunning the length of the gas cell was fixed to 5.5 mm. This value was known to be the optimal length for the gas medium from earlier studies with a similar setup [139]. However this has not been re-evaluated in the frame of this thesis.

3.4 Application and Outlook

The first step for the future investigations is to measure the pulse duration of the high order harmonic radiation. This will be done by using the pump and the probe beam line at the same time. In order to measure the pulse duration of the HHG radiation, the VUV (HHG) and NIR pulses will be focused in to the interaction region in the experimental chamber (Fig.3.1). The VUV pulses can be used to ionize He atoms. Whereas, the NIR photon energy (1.55 ev) is not enough to ionize the He atoms. In the next step the focused VUV and NIR pulses will be spatially overlapped by observing the focal spot of both beams on the YAG screen by means of a camera and a telescope. In the next step, a cable antenna can be used in the focus of both beams in order to detect the light pulses and monitor their temporal overlap by connecting the cable to an oscilloscope. With this method the overlap in time can be obtained with a precision of about 20 ps. An excellent temporal overlap of the VUV and NIR pulses in a sub-picosecond can be monitored in the photoelectron spectrum of the photoionization process of helium atoms in the interaction with both VUV and NIR photons. Here, in addition to the main peak, from the photoionization of helium atoms by the absorption of a VUV photon, sideband peaks can also be seen in the photoelectron spectrum.

Sidebands appear due to the simultaneous absorption (or stimulated emission) of an NIR photon (or more) and a VUV photon by the electron in helium atom (see next chapter). Therefore, in the next step one would scan the delay between NIR and VUV pulses, so that at some point the sideband appear in the photoelectron spectrum, so that the "zero-delay" is obtained. by scanning the temporal delay of the two pulses around the "zero-delay" and measuring the kinetic energy of the photoelectrons of helium atoms, it is possible to measure the pulse duration of the VUV radiation. This is explained for application at FEL experiments in the next chapter.

The SQS setup is designed to perform time resolved two-color pump-probe experiments to study ionization processes on atomic and molecular targets. In order to investigate ultrafast processes (fs time scale) in the electron dynamics of a certain target with an individual ionization energy, a short pulse with a short wavelength and accordingly a particular order of the high harmonics is necessary to be radiated on the sample. This order of the harmonics can be filtered out of the HHG pulses by means of a monochromator. Therefore, another important step to complete the pump-probe setup for a certain experiment is to mount a monochromator just after the HHG chamber (Fig.3.1).

The future goal of this HHG setup is to perform time resolved two-color pump-probe experiments for the investigating fragmentation of molecules as well as non-linear processes in atoms. Moreover, by developing this HHG source to a circularly polarized VUV radiation source, the polarization dependent in photoionization processes in atomic targets can be investigated in two-color VUV and NIR experiments. Thereby, the VMI spectrometer will be utilized to obtain the angular distribution of the photoelectrons. A similar kind of experiment was performed in the context of this work by making use of a VMI spectrometer. This experiment and more details about the application and investigations done by a VMI spectrometer can be found in the following chapter of this work.

CHAPTER 4

Two-Color Two-Photon Experiments as a Tool for Characterizing FEL Pulses

Multiple photoionization and photoexcitation in two-color experiments with short wavelength light sources (e.g. HHG and FEL) overlapped with optical laser pulses on atomic targets is a powerful method for investigations of electron correlations and inner-shell dynamics in the electronic structure of atoms. The photoelectron spectrum resulting from these experiments provides valuable information about the photon-matter interaction as well as fast relaxation processes (short life time of the relaxing excited states) in the atom. Therefore, multi-photon experiments with synchronized XUV and femtosecond optical laser pulse, have received special attention and have been successfully performed in different studies (e.g.[140, 141]). Regarding a more technical perspective, two-color experiments with XUV and optical laser pulses provide also an advantageous tool for characterizing FEL and HHG pulses [142, 143].

The advent of circularly polarized FEL sources opened a new opportunity for developing experiments to study new aspects in atomic, molecular and more complex targets. Furthermore, the unique feature of highly intense, circularly polarized FEL pulses also allows for investigations of circularly dichroic light matter interactions. Circular dichroism (see chapter 2) is typically a small effect of only few percent, underlining the great importance of sophisticated beam diagnostics. In order to enable such new perspectives on the distinct absorption differences between left and right circularly polarized light, the delivered radiation characteristics have to be analyzed before performing experimental investigations on different targets. In the context of this thesis, the first user experiment with highly intense circularly polarized FEL radiation has been performed at FERMI FEL-1 (see the Introduction1). The main goal of this experiment was to characterize the degree of circular polarization of FERMI. In this chapter, the methodological background of this diagnostic experiment as well as the results of the characterization are described in details.

This study is based on the photoionization of helium atoms in a two-color experiment using XUV and NIR pulses. Helium was selected for this investigation since it is theoretically and experimentally a well studied and well accessible tar-

get. In the photoionization of an atom, where an electron with a binding energy E_{bind} is ejected by the absorption of an XUV photon ($h\nu_{XUV}$), the electron will escape the atomic potential with a kinetic energy of $E_{kin} = h\nu_{XUV} - E_{bind}$. The signal of these photoelectrons detected by a VMI spectrometer, shows up as a main peak (mainline) in the photoelectron spectrum. A modulation of this process can be realized by the presence of a highly intense NIR laser pulse temporally overlapped and spatially synchronized with the XUV pulse. In this case, the target atoms are dressed by the strong electric field of the NIR laser. Under these conditions, the kinetic energy of the photoelectron ejected by the absorption of an XUV photon can change by the absorption or stimulated emission of NIR photons ($E_{kin} = (h\nu_{XUV} - E_{bind}) \pm nh\nu_{NIR}$). This effect can be observed in the photoelectron spectrum in form of additional peaks on both sides of the main line and are known as the sidebands. The number of the sidebands on each side of the mainline in the photoelectron spectrum, reflects the minimum number of absorbed (or stimulatedly emitted) NIR photons. The distance between first sidebands (on each side) and the main line in energy scale is equal to $h\nu_{NIR}$. Figure 4.1 shows the mainline and sidebands in the photoelectron spectrum in two-color ionization of helium atoms with one XUV and one NIR photon. There have been many experimental [140, 141, 144, 145] and theoretical [146, 147, 148] studies for understanding this phenomenon.

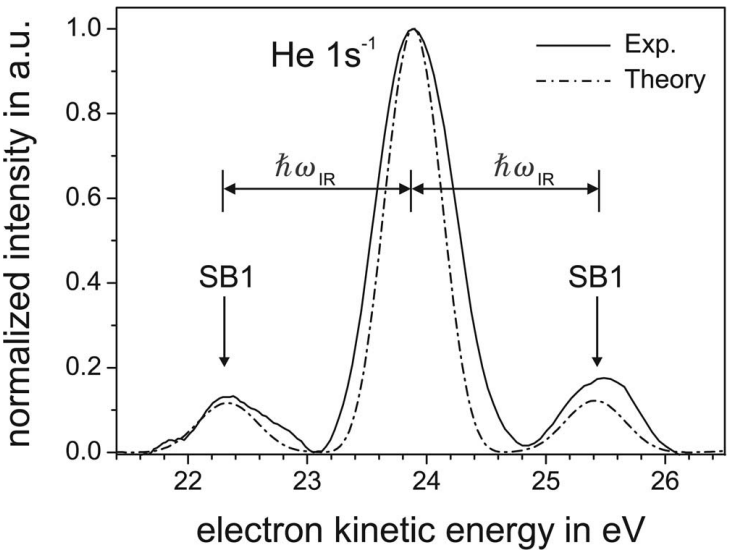

Figure 4.1: Photoelectron spectrum in the region of He $1s^{-1}$ for overlapping FEL+NIR beams showing the high and low-energy sideband. Dashed line: Theoretical photoelectron spectrum of He obtained from time dependent Schroedinger equation calculations for the present characteristics of the FEL and optical laser [83].

It was shown in previous two-color multi-photon studies with linearly polarized

light sources that the photoelectron angular distribution (PAD) and the sideband yields can be affected not only by the intensity of the dressing NIR laser field, but also by the change of the beam polarization [145]. Moreover, the PAD properties can reflect particular dynamics of the photon-atom interactions [144, 145]. In one-color experiments with circularly polarized radiation, the sensitivity of the PAD to the helicity of the light can be observed only, if the electronic structure of the target atom in ground state is not symmetric [149]. However, as it was predicted in theoretical studies [79, 86, 150], the sensitivity of the PAD and the yield of sidebands to the helicity of circularly polarized radiation can be observed in a two-color experiment with a symmetric atomic target, if an asymmetry is induced to the atoms by at least one of the colors.

For the characterization of unknown polarization properties of the FEL, it is worth to use an atomic target, which is well studied in order to predict the experimental results with theoretical calculations. In this regard, the current two-color experiment was performed with helium atoms and the sensitivity of the sidebands to the relative beam helicity (circular dichroism) was observed. As it is described in this chapter, this effect was then used to characterize the FEL polarization state.

In the following parts of this chapter, the experimental methods as well as the data analyzing techniques and the measurement results together with the theoretical predictions are described.

4.1 Experimental Setup at the LDM Beamline

The light pulses generated at FERMI FEL-1 provide a unique opportunity for many kinds of investigations. This FEL is the first seeded free-electron laser operating in the extreme ultra violet (XUV) region [27]. The pulses with a length of 30 to 100 fs (FWHM) carry an energy up to few 100 μJ depending on the wavelength and on the polarization. The photon energy of this radiation can vary between 12 and 62 eV. The repetition rate of the pulses can be set to 10 or 50 Hz [151]. For the purpose of the currently described experiment, the wavelength of the FEL radiation was set to 25.6 nm (48.4 eV photon energy), which corresponds to the 10^{th} harmonic of the tunable seed laser. At the time of this experiment, the repetition rate was limited to 10 Hz [39, 47].

The FERMI FEL-1 ends in three different experimental stations, the diffraction and projection imaging (DiProI), elastic and inelastic scattering (TIMEX, TIMER) and the Low density matter (LDM) endstation. The present experimental study was performed at the LDM endstation [152], which was designed, inter alia, for two-color investigations on atomic, molecular and cluster targets. In this study, the FEL radiation was pointed into the interaction volume of the LDM instrument by active focusing mirrors to a spot size of 50 μm. The peak intensity of the FEL beam in focus was in the order of $10^{13} W/cm^2$. Furthermore, the pulse energy of the FEL radiation was monitored by a gas monitor.

The NIR laser beam used in this setup is optically split from the seed laser of

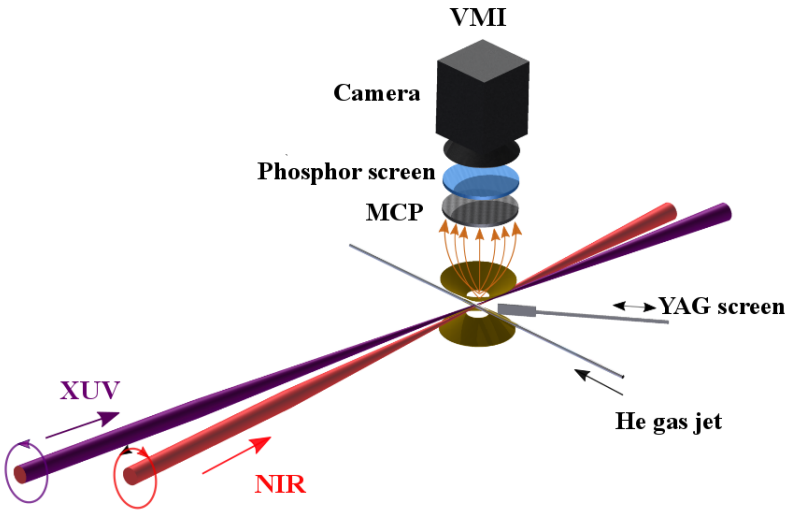

Figure 4.2: A schematic representation of the experimental setup at the LDM instrument. The TOF spectrometer is not displayed in this figure (see text). In the current experiment, the FEL radiation was left-circularly polarized. The NIR laser beam provided circularly polarized radiation with left- or right handed helicity.

the FEL [151]. The advantage of this configuration is a jitter free temporal overlap with the XUV radiation [39, 47]. In this experiment, the NIR laser was radiating with a central wavelength of 784 nm and with a duration of 175 fs. In this setup, the NIR pulses in the vacuum chamber are propagating almost co-linearly to the FEL radiation and are spatially overlapped with the XUV pulses in the interaction region. The spatial overlap can be controlled by motorized mirror systems in the NIR beam path and it is possible to monitor the focal spot of the two beams on an yttrium-aluminum-garnet crystal (YAG) by a CCD camera [39, 47].

4.1.1 Spectrometer and Data Acquisition

The LDM endstation contains two spectrometers, a VMI on top and a TOF spectrometer below the interaction volume, which can be operated simultaneously [153]. However, in the experiments performed within the context of this thesis, only the VMI spectrometer was employed in order to record the angle resolved photoelectron spectrum (see Fig.4.2)[39]. The photoelectrons produced in the interaction region of the light pulses and the target atoms (helium in this case) are accelerated by the strong electric field between the repeller and extractor electrodes (see chapter 3) towards the VMI spectrometer. The VMI detector consists of an MCP with a phosphor screen on top and an SCMOS camera as readout. The accelerated pho-

toelectrons from the interaction region move towards the MCP, where the signal is amplified and a large number of electrons are released in an avalanche of secondary electrons caused in the capillaries by the applied acceleration voltage. These electrons are subsequently hitting the phosphor screen. The kinetic energy of these electrons is enough to locally excite the surface of the screen so that the decay process in the local electronic structure of the screen releases a visible photon, which can be detected by the camera (see Fig3.6 in chapter 3). In this way, the hitting position of the photoelectrons can be recorded. The camera of the VMI spectrometer has a resolution of 6.5 μm [153]. The hitting position of all photoelectrons gives the projection of the photoelectron angular distribution in two dimensions (see chapter 3). In order to generate statistically valid single-shot VMI-spectra, it is necessary to have a sufficient gas density in the interaction volume. However, an overload of the gas in the interaction region has to be avoided, since space charge effects, which increase with increasing sample density, can be detrimental for the resolution of the electron spectra. Therefore, for the injection of gas phase targets, an injection system based on a supersonic jet containing an Even-Lavie pulsed valve is mounted to the vacuum chamber, which enables a supersonic gas injection into the interaction volume (for more details see [39, 153]). For the present study, other delivery methods such as an effusive gas jet would also be sufficient.

4.2 Temporal Overlap and Measurement of the FEL Pulse Duration

The first approach for a temporal overlap of the XUV and NIR pulses was realized by moving a broad band cable antenna into the focal region of the two beams. Each time the cable is irradiated by a pulse, a current can be measured on its other end. The signal of the cable connected to an oscilloscope shows two traces corresponding to the XUV and NIR pulses. By changing the path length of NIR pulses with a delay stage, the two peaks on the oscilloscope can be overlapped with a precision of < 50 ps.

In the next step, the temporal overlap of the pulses was adjusted on a sub-picoseconds time scale. For this purpose, a two-color two-photon ionization process was performed with He atoms. Thereby, the wavelength of the FEL beam was set to 51.53 nm. This photon energy is in resonance with the electron transition from the He ground state ($1s^2$) to the Rydberg excited state He $1s5p$ ^{1}P with an excitation energy of 24.03 eV and a life time of 7.7 ns [154]. The energy needed to ionize He from this state ($5p$-shell) is about 0.55 eV [1], which corresponds to an energy less than provided by one NIR-photon (1.58 eV). When the NIR pulse arrives within 7.7 ns after the XUV pulse, the He atoms can be efficiently ionized and the photoelectrons can be detected with a kinetic energy of 1.03 eV (Fig.4.3.a) [39]. The time delay of the two pulses was scanned from a negative time delay

[1] The ionization energy of He$1s^2$ is 24.58 eV

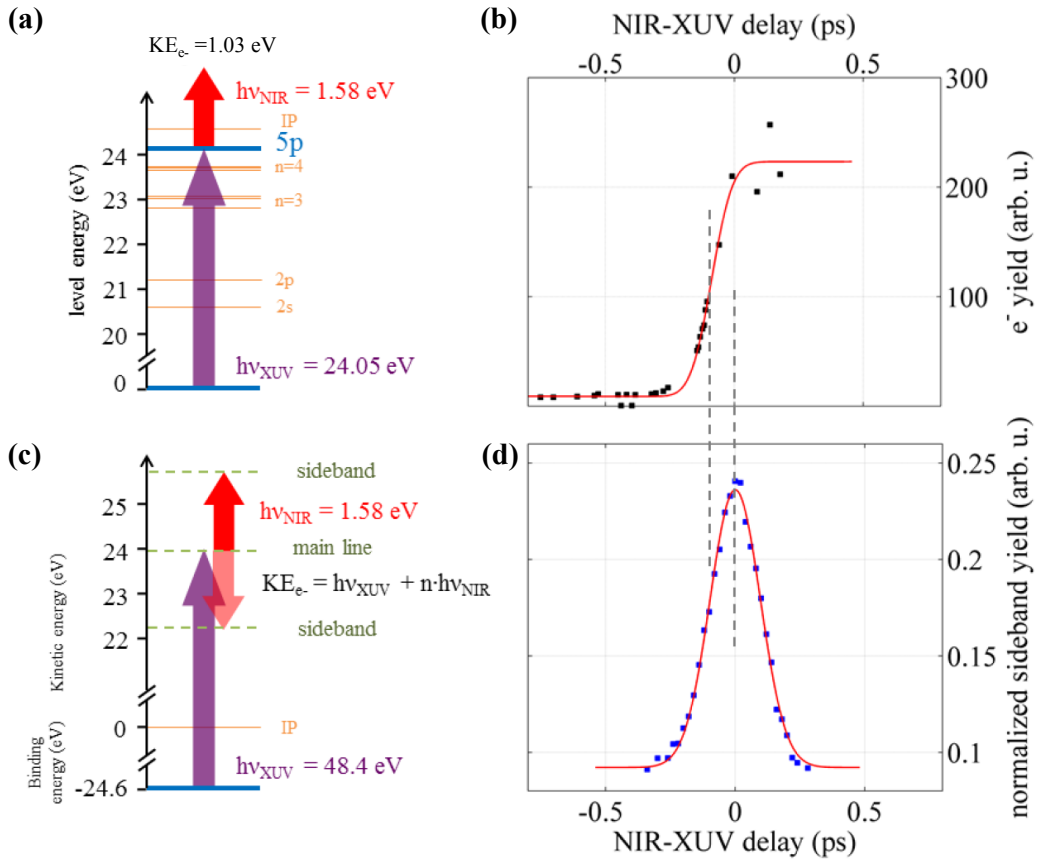

Figure 4.3: Scan of the temporal delay between FEL and NIR pulses produced for determination of "zero" delay time. The scan is performed looking at two different processes, namely the resonant two-photon ionization of atomic helium, schematized in panel (a), and the two-color two-photon direct photoionization producing sidebands (panel (c)). For both schemes the measured electron yield from the observed process is represented as a function of the NIR-XUV delay in panels (b) (black dots) and (d) (blue dots) respectively. (b) The yield from resonant two-photon ionization is modeled with a step function (red curve). The zero time delay is identified as the half-maximum position of the step function. In panel (d) the sideband yield, normalized to the yield from the mainline, is modeled with a Gaussian curve, and the peak position identifies the zero time delay (see text) [39].

(NIR pulse arrives before the XUV pulse) to a positive delay where the NIR pulse arrives after the XUV pulse and the photoelectron yield was recorded (Fig.4.3.b). The yield of the resonant two-photon ionization was modeled with a step function $f(t) = \int_0^t \exp(-(t-t_0)^2/\tau dt$ (see the red curve in fig.4.3.b) [39]. The position of the half-maximum of the step function is identified as "zero" time delay. With this

method the temporal overlap was determined with a precision on a sub-picosecond time scale.

In order to reach a sub 100-femtosecond scale of precision in the temporal overlap, the two-color above threshold ionization process (ATI) with He atoms was performed to measure the signal of the sidebands [40, 140]. This was realized by setting the photon energy of the XUV radiation to 48.4 eV and performing a new delay scan, so that the intensity variation of the sidebands could be detected. (Fig.4.3.c). This intensity variation was then normalized to the yield of the main line and is represented in the cross correlation curve of figure 4.3.d. The final optimization of the temporal overlap is done by maximizing the intensity of the sideband peaks in the photoelectron spectrum. The cross correlation curve was modeled with a Gaussian curve. The position of the peak intensity of this curve on the time axis corresponds to the zero time delay of the XUV and NIR pulses [39]. The width of this curve gives a convolution of the durations of FEL and IR pulses. The width of this curve ($\Delta\tau$) is 200 fs and is related to the duration of the XUV (τ_{XUV})and NIR (τ_{NIR}) pulses by the following equation:

$$\Delta\tau = \left(\tau_{XUV}^2 + \tau_{NIR}^2 + J^2\right)^{\frac{1}{2}}, \tag{4.1}$$

where J is the temporal jitter of the FEL radiation. As it can be seen in figure 4.3.b and 4.3.d, there is a difference of about 100 fs in the position of the time zero in the two scans. This difference corresponds to the change of the optical path of the OPA seed laser [2] due to the difference in the seed wavelength for the two experiments [39]. In this experiment, the temporal jitter was negligible (< 25 fs rms in this experiment) in comparison with the pulse durations [155]. As the NIR pulse duration is well known (175 fs), the cross correlation curve can be used to measure the pulse duration of the XUV radiation. Using equation 4.1, the duration of the XUV pulses was determined to be about 95 fs.

4.3 Characterization of the Polarization State of FERMI

Circularly polarized FEL radiation can be generated by "Apple2" undulators [19, 27, 28, 156, 157], which force the electron bunches to move in a spiral path. Thereby, a part of the kinetic energy of the electrons is radiated in form of circularly polarized photons. In order to characterize the polarization state and polarization degree of the FERMI FEL radiation, helium atoms were ionized by FEL photons with a distinct polarization setting, here left circular polarization. The absorption of such a photon leads to an induced orientation in the helium atom.

Considering a single photon ionization of a He atom by a left-handed FEL photon ($J = -1$) with an energy of 48.4 eV, the $1s$ electron will be released into a

[2] OPA: Optical Parametric Amplifier

continuum state with an angular momentum of $j = 1$ (p-wave), $m_j = -1$. This photoelectron is leaving the atomic potential with a kinetic energy of 23.8 eV and can be detected in the photoelectron spectrum (as a main line). The PAD in this case is a 2D-projection of a p-wave angular distribution. However, this information is not enough for the determination of the polarization state of the XUV pulses, since the magnetic quantum number of the final state of the photoelectrons cannot be obtained in this process. Therefore, the XUV-ionization process was performed in the presence of the synchronized NIR pulses. The simultaneous absorption of an XUV and an NIR photon would result in a sideband in the photoelectron spectrum at a higher energy than the main line, separated by the NIR photon energy.

In order to confirm the polarization status of the FEL photons (supposed to be left-handed circularly polarized), the final state of the photoelectrons has to be obtained from the acquired photoelectron spectrum. The final continuum state of the photoelectron depends on the relative helicity of the circularly polarized beams. The helicity of the photons can be determined then by characterizing the continuum-continuum transition of the photoelectrons in a two-color study with the FEL pulses and circularly polarized NIR photons with a well known helicity.

By considering only the higher sideband in case of a left-handed NIR photon, the final state of the photoelectron would be a d-state with a magnetic quantum number

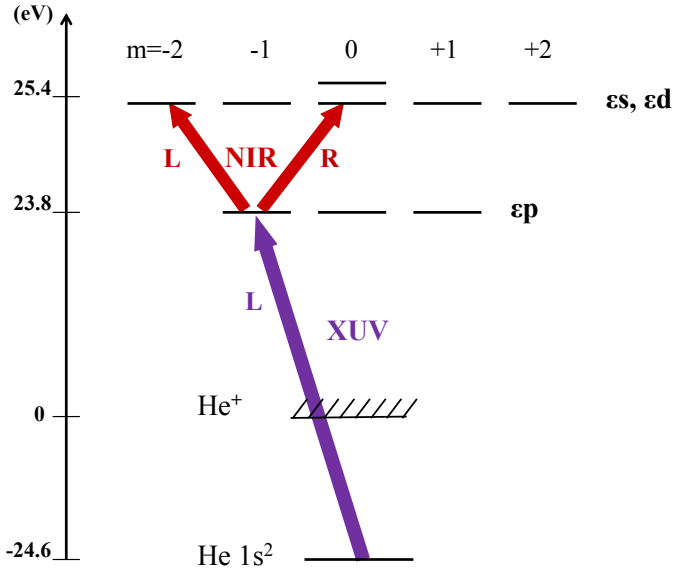

Figure 4.4: Schematic of the two-color ionization of He by left-handed circularly polarized XUV photon and the additional absorption of a left- or right-handed photon. depending on the relative polarization of the beams, the final state of the electron in the continuum can be different. This schematic includes only the case of absorption of an NIR photon.

of $m = -2$ (see Fig.4.4). In case of right handed NIR photon, the photoelectron would be prepared in an s- or d-state with a magnetic quantum number of $m = 0$.

For verifying the polarization status of the FEL photons, the NIR laser beam was operated in a left- and right-handed circular polarization state. The simulated spectra based on SFA calculations predict that in case of co-rotating (left-left, LL) XUV and NIR pulses the yield of the higher sideband would be higher than in the case of counter-rotating beams (left-right, LR). Therefore, the helicity of the XUV radiation was determined by comparing the intensity of the high energy sideband for the co- and counter-rotating case. This gives the circular dichroism (CD):

$$CD = \frac{I_{LL} - I_{LR}}{I_{LL} + I_{LR}}, \tag{4.2}$$

where I_{LL} and I_{LR} correspond to the intensity of the higher sideband for co-rotating and counter-rotating XUV and NIR radiation, respectively. A negative value of the CD would mean a higher intensity of the sideband for a left-handed helicity of the NIR beam. This again would confirm that the helicity of the FEL radiation should be the same (left-handed), since the for co-rotating beams the sideband intensity was predicted to be higher.

SFA predicts the circular dichroism to be maximum at $(90)^\circ$ in the angle resolved photoelectron spectrum [47]. Figure 4.5.a shows the photoelectron spectrum for an emission angle of $(90\pm4)^\circ$. The red line shows the simulated spectrum based on SFA and the black dashed line is resulting from the experimental measurements. The circular dichroism of the higher sideband in the photoelectron emission ($25.2 - 26.1$ eV) was theoretically calculated for the cases of 90% and 100% circularly polarized radiation (Fig.4.5.b) [47]. The experimental result for the circular dichroism of the higher sideband was determined to be -0.04 ± 0.004. This negative value confirms that the helicity of the FEL radiation is left-handed.

For the determination of the circular polarization degree of the XUV pulses, the lower sideband was not taken into the account. As it can be seen in figure 4.5.b the error of the experimental result for the lower sideband is much higher, which comes from the overlap of the signals of the main line and the lower sideband in the angle resolved photoelectron spectrum of the VMI (see chapter 5).

The photoelectron transfer from the main line to the sidebands by absorption (or stimulated emission) of NIR photons, is a polarization dependent process (due to its orientation). Therefore, the number of electrons transferred to the higher- and lower sidebands is not exactly equal, which results in a nonzero circular dichroism in the main line as shown in figure 4.5.b. This small value can also be affected by the quality of the overlap of the NIR and XUV pulses in the interaction region, since in case of an imperfect overlap, a part of the ionized He atoms could miss the NIR pulses. This effect was also included in simulations [39].

Comparing the experimental and theoretical results for the circular dichroism of the higher sideband, the purity of the circular polarization of FERMI pulses is calculated to be 0.95 ± 0.05 at the location of the experiment [47]. This number

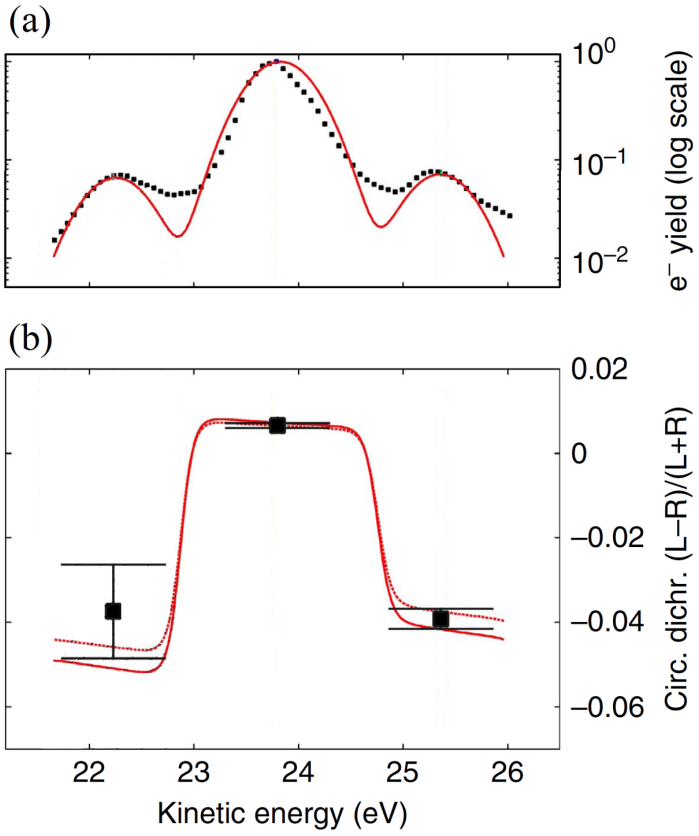

Figure 4.5: (a) Experimental (black squares) and theoretical (solid red line) electron spectra. (b) Comparison of the circular dichroism in the photoelectron emission derived from the experimental (black squares) and the theoretical (red lines) spectra at emission angles of $(90 \pm 4)°$; the red-dashed line represents a circular polarization of 90%. The squares represent the average value and the respective statistical error from the energy region corresponding to each photoemission line. The low-energy sideband was not taken into account for the analysis, since the overlap of this sideband with the main photoemission line in the VMI spectrum results in a relatively large error bar [47].

could be reduced by any linear or unpolarized [3]. radiation of the NIR or XUV (FEL) pulses. As the NIR laser pulses had a circular polarization degree of almost 100%, the error in the determination of the purity of circular dichroism in XUV pulses does only negligibly depend on it [47].

[3]Here, the term "unpolarized" is used for randomly polarized photons so that the polarization of all these photons cannot be classified in the different polarization categories (Linear, circular and elliptical).

CHAPTER 5

Intensity Dependence in the Two-Color Photoionization of Helium Atoms

The photoionization of helium atoms with XUV and NIR pulses in the FERMI FEL diagnostics was already discussed in chapter 4. In this chapter, the physical aspects of this process, such as the angular distribution and circular dichroism of the photoelectrons as well as the effect of the NIR laser intensity will be discussed in more details. The setup and experimental condition are the same as described in chapter 4. As it was mentioned in the previous chapter, the photoionization of He atoms was investigated by applying circularly polarized XUV pulses with a photon energy of 48.4 eV. The PAD, was projected to the position sensitive detector of the VMI spectrometer (see Fig.5.1). The symmetry axis of the VMI is perpendicular to the propagation axis of the FEL radiation. Therefore, the quantization axis is the same as the beam-propagation axis and is shown by the white arrow in figure 5.1.b. According to equation 2.15 for single-photon ionization of helium atoms (He $1s^2$) with circularly polarized radiation, the PAD is expected to be similar to the donut-distribution shown in figure 2.6. The 2D-projection of the PAD is shown in figure 5.1.b, where the intensity of the photoelectrons has a maximum at the emission angle of $\theta = \pi/2$. The intensity distribution of the photoelectrons at an emission angle of $\theta = \pi/2$ is shown in figure 5.1.c. This 2D angular distribution is in fact similar to figure 2.5 for $\beta = 2$. The spatial distribution of the photoelectrons in the interaction region can be traced back from the two dimensional angle resolved distribution of the photoelectrons by applying the inverse Abel-transformation method [113].

In the XUV-photoionization of dressed helium atoms with an NIR laser field, sidebands can be observed in the PAD. Here, the number of the sidebands is directly depending on the minimum number of NIR photon interactions and is therefore, highly sensitive to the peak intensity of the NIR radiation in the interaction volume. In order to study the intensity dependence of the PAD and the circular dichroism, the two-color above threshold ionization (ATI) of helium atoms was performed in two different intensity regimes. The experimental approach and the obtained results of this study are described in the following parts of this chapter.

In the weak intensity regime, the peak intensity of the NIR radiation was set to

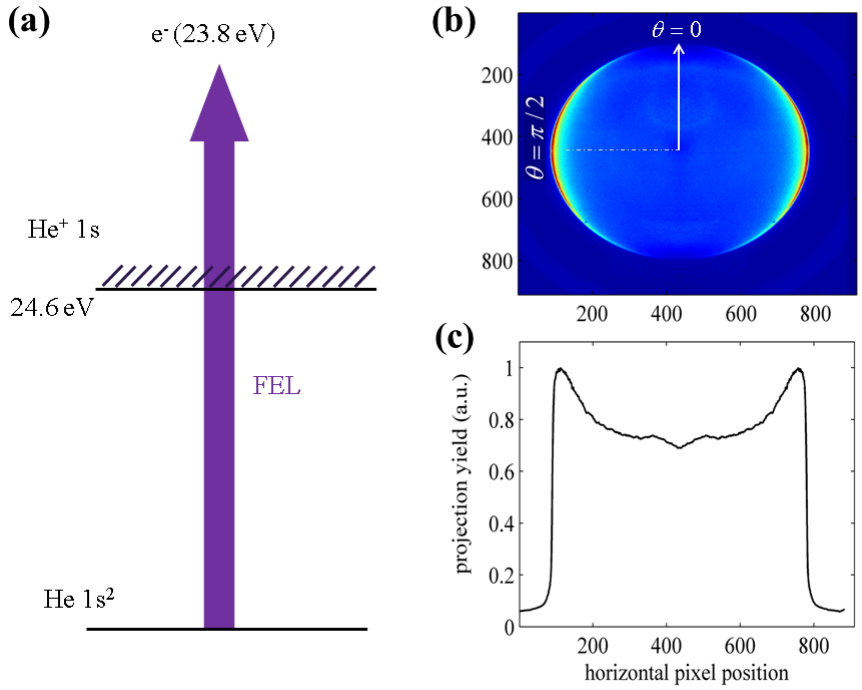

Figure 5.1: (a) Schematic view of the single-photon ionization of He atoms by an XUV pulse of $48.4eV$. (b) The 2D-projection of the photoelectron angular distribution $(p, m = \pm 1)$ on the VMI, the white arrow shows the direction of beam-propagation.(c) The photoelectron yield at emission angle $(\pi/2)$ in the 2D-projection of the angular distribution.

$3 \times 10^{11}\, W/cm^2$ whereas, for the strong regime it was increased to $7.2 \times 10^{12}\, W/cm^2$. Figure 5.3 shows the spectrum of the photoelectron ejected in the ATI of He atoms at an emission angle of $\theta = 90°$ for the low intensity regime of NIR pulses (blue curve) and highly intense pulses (red curve). The central photoline at approximately 24 eV appears due to the absorption of an XUV photon, since the ionization potential of the $1s$ electron in He is equal to 24.6 eV. The spectra are normalized to the total electron yield, as the NIR intensity regime is well below the threshold for direct ionization of ground state He $1s^2$. Thus, the total electron yield can be assumed to be solely determined by the XUV intensity and therefore, to be independent on the NIR intensity. In other words, the integral of the photoelectron spectrum should stay the same and therefore, with the appearance of the sidebands the yield of the main line will decrease. Consequently, an increase of the NIR intensity, which leads to formation of a higher number of sidebands, would result in a larger decrease of the main line yield in the photoelectron spectrum.

In the following, the data analyzing method and the experimental results for the measurement of the angular distribution of the photoelectrons as well as the circular dichroism in both NIR intensity regimes, are presented and compared with the theoretical calculations. In the next chapter, the results of the photoemission

in the resonance excitation of He ions in a multi-photon process is described.

5.1 Data Analysis

The experimentally obtained 2D-distribution of photoelectrons can be utilized to reconstruct the initial 3D PAD by using the inverse Abel transformation (IAT) [113]. Once IAT is applied, a 2D projection of the initial 3D PAD is to be compared with the raw data and an error is found. This reciprocal process is continued until the measure of difference approaches to a minimum, resulting in a successful reconstruction of the 3D PAD. Figure 5.2 shows a comparison between the raw data (left half of the figure) and the reconstructed 2D spectrum (right half). The VMI images for the experiment described in this chapter have been recorded for a total number of 36000 single shots [39]. To determine the circular dichroism, the difference between two electron images for both helicities of the NIR beam have been recorded and the background signal has been subtracted from the spectra.

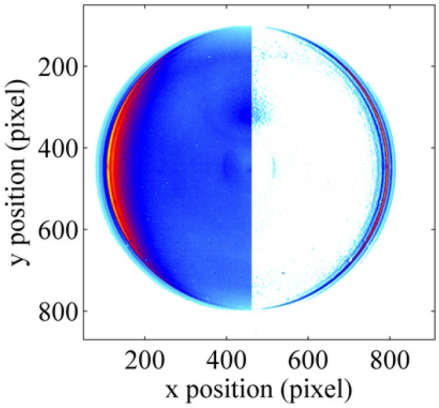

Figure 5.2: The left half of the figure shows the raw image on the VMI detector obtained from the two-color photoionization process, and the right half of the figure is a section of the reconstructed 3D velocity and angular distribution obtained from the experimental raw data by using the inverse Abel-transformation [39].

In order to obtain the experimental PAD, the main signal and each sideband signal in the raw angle resolved spectrum, were integrated over the full width of half maximum (FWHM) of its peak in a narrow angular binning. In the next step, the angular distribution was fitted by equation 2.15, where the asymmetry parameters ($\beta_{2k}^{\nu\nu'}$) have been used as fitting parameters. By changing the integration range within the FWHM of the photoemission peak, the fitting parameter (β) will change. This variation was used to estimate the uncertainty of the β-parameters [39].

For a realistic comparison between experimental and theoretical results obtained by the SFA, the three-dimensional angle resolved photoelectron spectra (double

differential cross section) is simulated based on the theoretical predictions assuming a non-uniform distribution for the NIR intensity distribution. In these simulations, the intensity ratio of the sidebands and main line have been adjusted in a way that gives the best fit to the experimental spectra. This method realizes the quantitative estimation of the influence of intensity distributions in the experimental results for a realistic condition.

5.2 PAD in Photoionization of Dressed He Atoms in Low Intensity NIR Fields

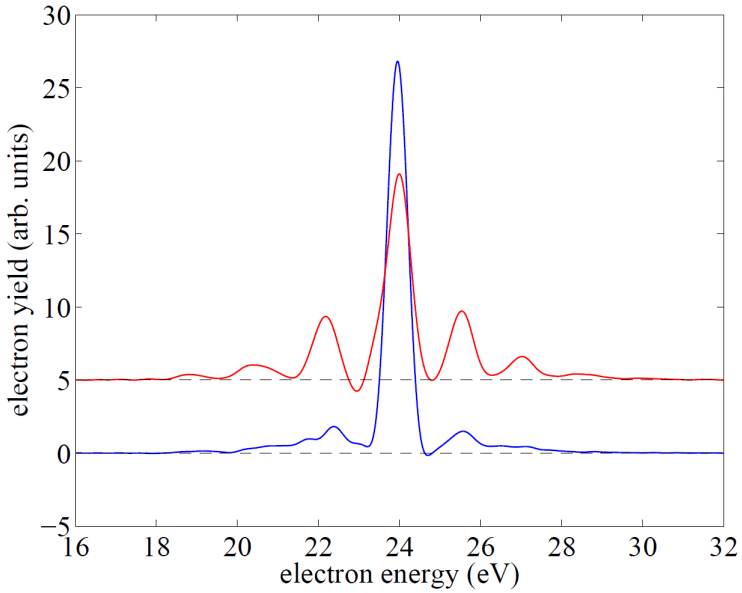

Figure 5.3: Formation of sidebands in the photoelectron spectrum at $\pi/2$ emission angle, resulted from the ATI of helium atoms with XUV radiation in the presence of NIR field for two intensity regimes of the NIR radiation, high intensity ($7.2 \times 10^{12}\, W/cm^2$, red curve) and low intensity ($3 \times 10^{11}\, W/cm^2$, blue curve). The red curve was shifted to a higher level for illustration reasons [39].

In the low intensity regime of the NIR radiation, the intensity of the laser beam has been selected such, that only one sideband appears on each side of the central photoline in the photoelectron spectrum. Here, the main photoline in the spectrum shows up at about 24 eV and is a result of the absorption of an XUV photon with the energy of 48.4 eV (blue curve in figure 5.3). In the low intensity

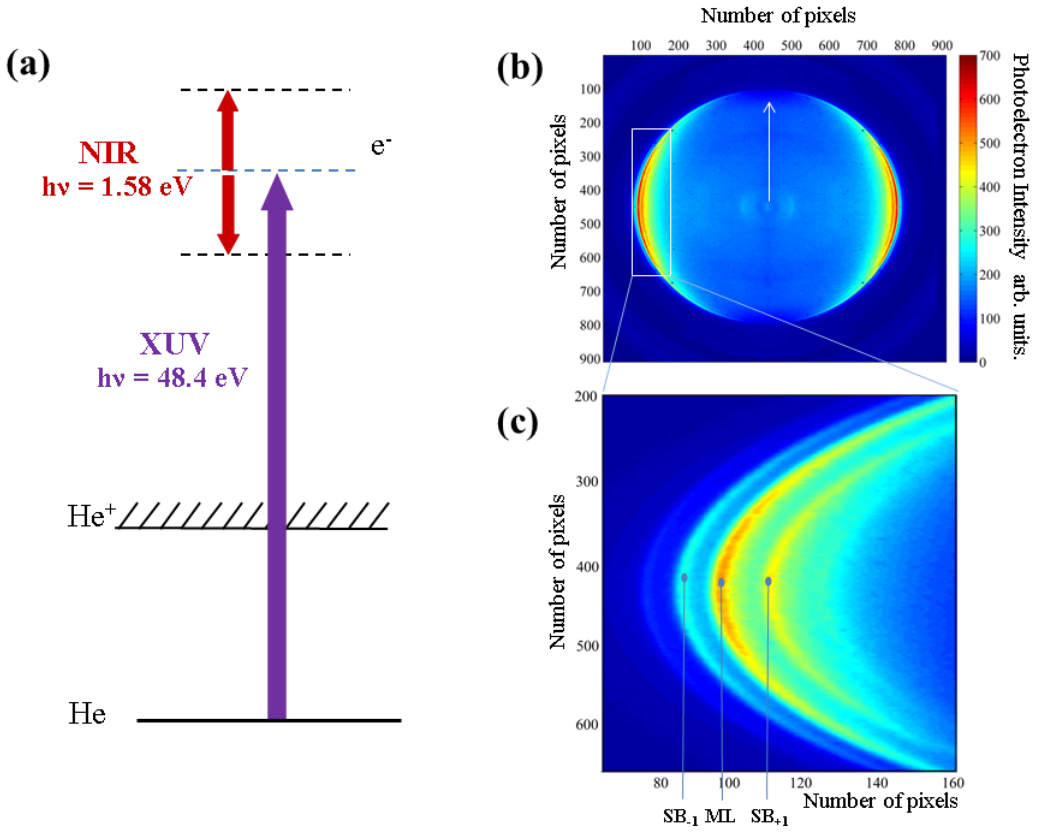

Figure 5.4: (a) Schematic view of the ATI of He atoms with XUV radiation in the presence of an NIR field, both with a circular polarization. Here, the XUV and NIR pulses are in an excellent temporal and spacial overlap. (b) The 2D-projection of the PAD (raw data). The color-code is showing the photoelectron yield. The white arrow shows the direction of the beam-propagation. (c) Zoomed picture, the main photoline (ML) and the higher- and lower sidebands (SB_{+1} and SB_{-1}, respectively), are clearly seen. The maximum of the low energy sideband (SB_{-1}) seems to be more intense than the high energy one (SB_{+1}). This effect in the 2D projection is due to the overlap of the main photoline with the low energy sideband (see text and Fig.5.5).

NIR beam, only few NIR photons are involved in the interactions. Thus, the predictability of the underlying processes within the strong field approximation is very robust. Therefore, this intensity condition is optimally suited for proving fundamental concepts in photon matter interaction. Figure 5.4 shows the 2D projection of the photoelectron angular distribution detected by the VMI spectrometer.

As expected, in the case of relatively low NIR intensity, the main photoline (ML) is more intense than the sidebands. Although the lower energy sideband has a higher maximum than the high energy sideband, its yield is smaller as it can be

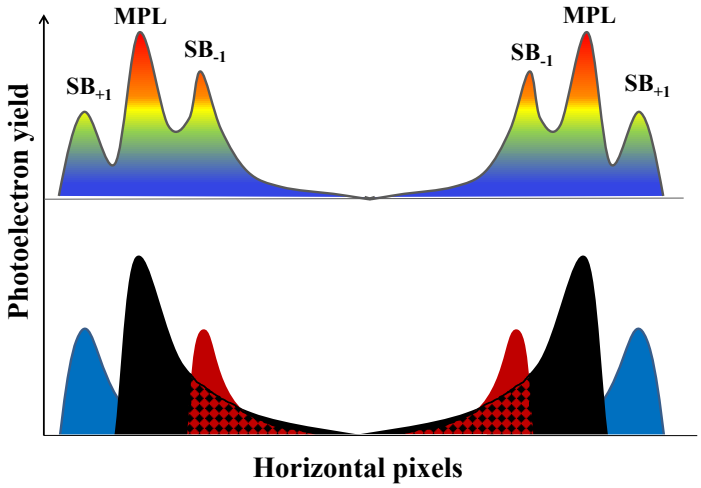

Figure 5.5: A schematic view of the overlap signals of the mainline and the low energy sideband in the VMI. (Top): The low energy sideband (SB_{-1}) appears with a higher maximum in comparison to the high energy sideband (SB_{+1}), (below) this is due to the overlap of the signals of the mainline and the low energy sidebands, which is overlapped so that the sum of both signals appears for the low energy sideband [39].

seen in figure 5.5. As it can be seen in this schematic view, this effect appears since the signal of the mainline has a relatively large overlap with the lower sideband in comparison with the higher sideband.

The signal of the VMI (see for example Fig.5.4.b) shows the angular distribution in a polar coordinate system, where the radius component increases with the kinetic energy of the photoelectrons and the angular component is related to the angular momentum of the photoelectrons (see chapter 2). In the photoionization of He $1s$, the PAD generated by single-photon absorption of an FEL photon and photoelectrons from a two-color (FEL and NIR) two-photon absorption are shown in figure 5.6.a. This angular distribution can be transformed to a Cartesian coordinate system as a double differential cross section (emission angle vs. photoelectron kinetic energy). The experimental result and the SFA based simulation for the double differential cross section are represented in figure 5.6.(b) and (c). For the single photon absorption and two photon absorption, this was done by fitting equations 2.13 and 2.15 for $k = 2$, respectively, where the β-parameters in the equations were used as fitting parameters [39].

The two-color photoionization of helium was studied under two different polarization configurations of the XUV and NIR pulses. The first configuration are co-rotating pulses, where both XUV and NIR have a left handed helicity (LL) and

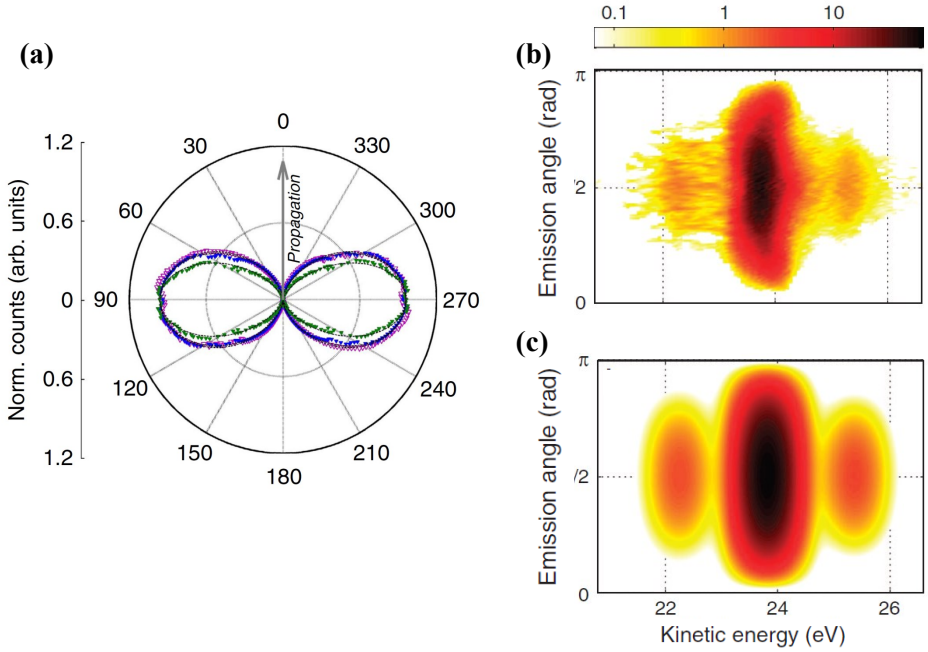

Figure 5.6: (a)Polar representation of the angular distributions (normalized to the maximum) for the one-photon ionization of He (purple) and for the two-color two-photon ionization leading to the main photoline (blue) and the sideband (green). Dashed-black curves are the best fitting of the experimental data with equation 2.13 and equation 2.15 for $k = 2$, respectively. (b) Experimental result for the double differential cross section and (c) the SFA based simulation of the double differential cross section. The respective intensities for (b,c) are indicated by the color scale on top of (b) [47].

the second configuration is the counter-rotating case with a left handed XUV pulse and right handed NIR radiation (LR).

For both polarization combinations (LL, LR), the asymmetry parameters $\beta_2^{\nu\nu'}$ and $\beta_4^{\nu\nu'}$ from equation 2.24, have been determined from the experimental data for the high energy sideband (SB_{+1}) and the low energy sideband (SB_{-1}). The results were compared with theoretical calculations based on the strong field approximation and perturbation theory (see chapter 2). The theoretical- and experimental results for the β-parameters are presented in table 5.1 [39]. In general, the experimental values of the asymmetry parameters are in a good agreement with the theoretically calculated values. However, the values calculated in the perturbation theory approach for the two cases of the LL polarization configuration (SB_{-1}) and LR one (SB_{+1}), the agreement is slightly worse. This could be due to the low kinetic energy of the photoelectrons, which is not high enough to theoretically describe the photoelectrons (without NIR field) by a plane wave [39].

Comparing the two polarization combinations LL and LR, a small difference can be determined from the angle integrated photoelectron yield of the sidebands, which is showing the appearance of the circular dichroism. The same effect can also be seen in the results of the theoretical calculations based on the perturbation theory approach.

Using equations 2.26 and 2.27 for the experimental values of $\beta_2^{\nu\nu'}$ and $\beta_4^{\nu\nu'}$, the ratio of the matrix elements D_s and D_d were determined as the following:

$$\left(\frac{\mid D_s \mid}{\mid D_d \mid}\right)_{SB_{+1}} = 1.00 \pm 0.04, \tag{5.1}$$

$$\left(\frac{\mid D_s \mid}{\mid D_d \mid}\right)_{SB_{-1}} = 1.07 \pm 0.06, \tag{5.2}$$

which are in agreement with the perturbation theory prediction of $\frac{|D_s|}{|D_d|}$ for the higher- and lower sideband, which are 1.04 and 1.12, respectively. The relative phase of the s and d radial matrix elements (δ_{ds}) was determined from the experimental values of β_2^{+-} to be:

$$\delta_{ds} = \delta_d - \delta_s \approx 0.75\pi. \tag{5.3}$$

The s and d channels have almost the same contribution in the first sidebands [145] so that the radial matrix elements D_s and D_d are almost the same and therefore, using equation 2.27, similar valuse can be obtained for β_4^{+-} and β_4^{++}. However, the value of β_2^{+-} (Eq.2.26) can change due to the relative phase of the D_s and D_d (δ_{ds}) amplitudes. The slight difference in the values of $\frac{|D_s|}{|D_d|}$ for the two sidebands is coming from different electron energies in the continuum. The theoretical value of δ_{ds} is calculated by applying the Hartree-Fock approximation and is 0.43π. The clear disagreement between this value and the experimental value (Eq.5.3) can be interpreted by additional phases, which appear due to the non-resonant continuum-continuum transition of electrons.

Table 5.1: The asymmetry parameters $\beta_2^{\nu\nu'}$ and $\beta_4^{\nu\nu'}$ measured and calculated for the low energy (SB_{-1}) and high-energy (SB_{+1}) sidebands in two-color photoionization of He at low NIR intensity of $3 \times 10^{11}\, W/cm^2$. Theoretical values are calculated using strong field approximation (SFA) and perturbation theory (PT) [39].

Case	Sideband	β_2			β_4		
		Exp	SFA	PT	Exp	SFA	PT
LL	SB_{+1}	-1.39 ± 0.02	-1.40	-1.43	0.41 ± 0.02	0.40	0.43
	SB_{-1}	-1.37 ± 0.04	-1.33	-1.25	0.38 ± 0.04	0.33	0.35
LR	SB_{+1}	-1.43 ± 0.02	-1.47	-1.30	0.43 ± 0.02	0.47	0.40
	SB_{-1}	-1.39 ± 0.04	-1.41	-1.43	0.40 ± 0.05	0.40	0.43

5.3 PAD in the Photoionization of Dressed He Atoms in High Intensity NIR Fields

In a high intensity NIR dressing field, the probability of the photoabsorption will increase and lead to a higher number of the sidebands. Figure 5.7.a shows the double differential photoelectron yield in the photoionization of helium atoms with co-rotating XUV and NIR fields (LL), where the intensity of the NIR field is $7.2 \times 10^{12}\, W/cm^2$. The experimental measurements for the double differential cross section are in excellent agreement with the theoretical predictions based on the strong field approximation (Fig.5.7.b) [39].

The angular width in the PAD decreases with increasing order of the sidebands. This phenomenon can be seen in the theoretical results as well as the experimental measurements (Fig.5.8). The higher the order of the sidebands, the more strongly the PAD is peaked around the emission angle of 90°. This can be explained by the fact that the electric field vector of the circularly polarized NIR radiation is rotating in the plane perpendicular to the propagation axis of light. Therefore, an electron emitted at 90°, is most strongly affected by the NIR field and, therefore shows the maximal number of sidebands [39]. Hence, the highest order sidebands appear in a narrow region around 90°, while the lower order sidebands can be observed in a broader range of angle [39].

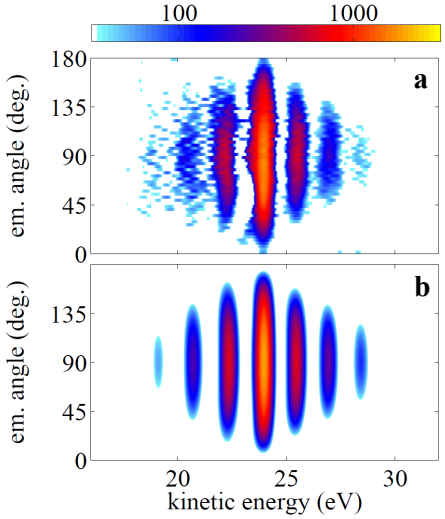

Figure 5.7: 2D plot of experimental angle-resolved spectra at high NIR intensity (a) and the corresponding SFA-simulated double differential cross section with a nonuniform intensity distribution of the NIR beam (b). The helicities of the NIR and XUV pulses are co-rotating. The color scale is logarithmic in arbitrary units [39].

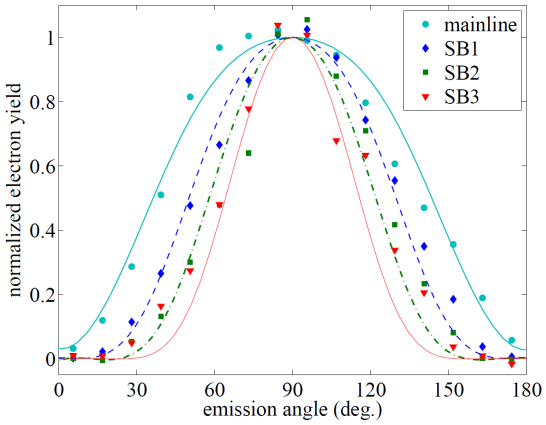

Figure 5.8: Angular distribution from high intensity measurement for: main line (cyan dots and solid bold line), first (blue diamonds and dashed line), second (green squares and dash-dotted line), and third (red triangles and solid thin line) high energy sidebands (SB), when the XUV and NIR radiations are co-rotating with a left handed helicity (LL). Symbols represent experimental data, curves the results of simulations [39].

In the experimental spectra, three sidebands on each side of the main photoline are clearly visible. This number of sidebands is an indication of a multiphoton absorption process with one XUV-photon and at least three NIR-photons. According to the equation 2.15, four asymmetry parameters $\beta_2^{\nu\nu'}$, $\beta_4^{\nu\nu'}$, $\beta_6^{\nu\nu'}$ and $\beta_8^{\nu\nu'}$ should be included in the description of the PAD.

The value of the asymmetry parameters $\beta_{2k}^{\nu\nu'}$ decreases very fast with an increasing number of photons (k). The experimental measurement of the small $\beta_8^{\nu\nu'}$ includes a large error and its value is unreliable. Therefore, the experimental photoelectron angular distributions where analyzed with $\beta_2^{\nu\nu'}$, $\beta_4^{\nu\nu'}$ and $\beta_6^{\nu\nu'}$ [39]. The values of these parameters for both cases of co-rotating and counter-rotating XUV and NIR pulses have been experimentally measured and theoretically simulated. The results are presented in table 5.2. The theoretical and experimental values of the asymmetry parameters for the first two sidebands on both sides of the main line are in a good agreement [39]. However, for the case of the third sideband, the agreement is worse. This could be related to the fact that the determination of the asymmetry parameters for the higher order sidebands is more difficult as the value of higher order β decreases rapidly for these sidebands [39]. The decreasing value of $\beta_{2k}^{\nu\nu'}$ with the increase in the value of k (see table 5.2) could be interpreted by the contribution of large orbital momenta of the electrons in the multi-photon process, which is small at the considered NIR intensities [39].

Comparing the results for the β-parameters of the high-energy and low-energy sidebands of the same order in table 5.2, one can see a difference, which is increasing with the order of the sideband and the order of the β-parameters [39]. This can be explained by the different photoelectron energies, which are also affecting the

Table 5.2: The asymmetry parameters $\beta_2^{\nu\nu'}$, $\beta_4^{\nu\nu'}$ and $\beta_6^{\nu\nu'}$ measured and calculated for the low-energy (SB_{-n}) and high-energy (SB_{+n}) sidebands in two-color photoionization of He at high NIR intensity of $7.2 \times 10^{12}\, W/cm^2$. Theoretical values are the result of simulation using the strong field approximation (SFA) [39].

Case	Sideband	β_2		β_4		β_6	
		Exp	SFA	Exp	SFA	Exp	SFA
LL	SB_{-3}	-0.90 ± 0.09	-1.62	0.29 ± 0.04	0.72	-0.07 ± 0.10	-0.09
	SB_{-2}	-1.19 ± 0.07	-1.38	0.45 ± 0.16	0.34	-0.24 ± 0.20	0.05
	SB_{-1}	-1.15 ± 0.13	-1.09	0.17 ± 0.23	0.08	-0.02 ± 0.10	-1.10^{-5}
	SB_{+1}	-1.17 ± 0.03	-1.17	0.16 ± 0.07	0.06	-0.02 ± 0.07	0.09
	SB_{+2}	-1.41 ± 0.07	-1.44	0.45 ± 0.12	0.39	-0.14 ± 0.10	0.08
	SB_{+3}	-1.46 ± 0.07	-1.68	0.55 ± 0.15	0.83	-0.22 ± 0.20	-0.12
LR	SB_{-3}	-0.81 ± 0.10	-1.72	0.16 ± 0.08	0.89	-0.01 ± 0.20	-0.18
	SB_{-2}	-1.09 ± 0.05	-1.49	0.31 ± 0.12	0.48	-0.17 ± 0.10	0.04
	SB_{-1}	-1.17 ± 0.08	-1.21	0.11 ± 0.11	0.11	-0.00 ± 0.001	0.09
	SB_{+1}	-1.27 ± 0.05	-1.25	0.24 ± 0.06	0.12	-0.00 ± 0.04	0.13
	SB_{+2}	-1.48 ± 0.08	-1.54	0.57 ± 0.11	0.52	-0.16 ± 0.10	0.07
	SB_{+3}	-1.47 ± 0.08	-1.77	0.52 ± 0.14	0.98	-0.05 ± 0.20	-0.20

involved transition matrix elements. The difference between the asymmetry parameters for the co-rotating (LL) and counter-rotating (LR) cases of the XUV and NIR pulses is a clear indication of the existing circular dichroism in the two-color multiphoton ionization process [39].

5.4 NIR Intensity Dependence of PADs

According to the values of β-parameters presented in the tables 5.1 and 5.2, there is a dependence of the value of $\beta_2^{\nu\nu'}$ and $\beta_4^{\nu\nu'}$ to the strength of the NIR field, for different sideband-orders. The intensity dependence of the β-parameters was obtained from the experimental data and was compared to the theoretical calculations based on SFA. As it can be seen in figure 5.9, the β parameters predicted by SFA under the assumption that the NIR intensity is uniformly distributed over the XUV ionization region, show a strong variation. However, the obtained experimental data (dots with error bar) show only a smooth variation, which is due to the non-uniform intensity distribution of the NIR radiation [39]. The bold lines are representing the asymmetry parameters obtained from simulated spectra based on SFA by assuming a realistic intensity distribution, which is more compatible with the experimental data. The values of the asymmetry parameters at zero intensity are calculated values based on the perturbation theory. The $\beta-$parameters are considered to be independent from the atomic model [39]. At the intensities lower than $3 \times 10^{12} W/cm^2$, the absolute value of the asymmetry parameters is increas-

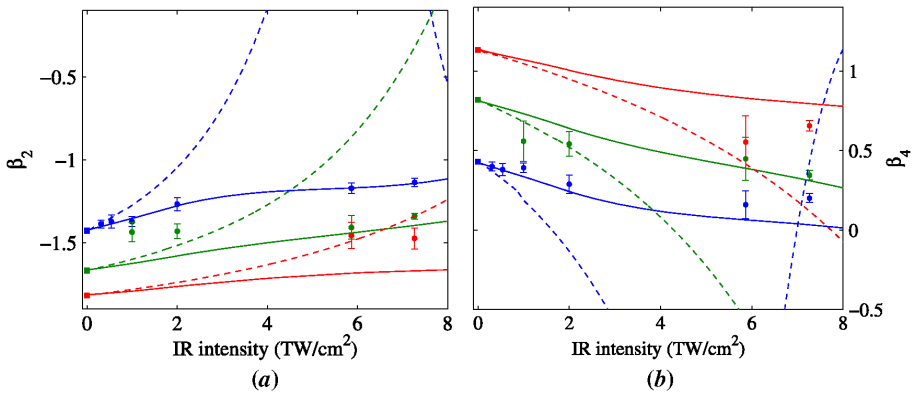

Figure 5.9: NIR intensity dependence of β_2 (a) and β_4 (b) for co-rotating case, and high energy sidebands (blue = first, green = second, red = third). Circles with error bars: experimental values. Solid lines: Strong field approximation calculation with a realistic intensity distribution. Dashed lines: Strong field approximation from uniform intensity. Squares at zero intensity: perturbation theory. Intensity is intended as the peak intensity in the case of a realistic photon distribution [39].

ing with the order of the sidebands. Comparing with the values predicted by the perturbation theory calculations, the increasing values of $\beta_k^{\nu\nu'}$ could be due to the effect of the angular momentum coupling, since the dynamics are not involved in values calculated by the perturbation theory approach [39].

Considering a larger NIR-intensity interval, the simulations based on the strong field approximation with a uniform focal intensity distribution, show an oscillating behavior for parameters $\beta_2^{\nu\nu'}$ and $\beta_4^{\nu\nu'}$ [39]. This behavior can be explained as an interference of photoelectrons partial waves, since the count of photoelectrons with different wave functions increases with the rising number of exchanged photons in the ionization process.

5.5 Circular Dichroism at Different Intensities

In the current experiment, for co- and counter rotating XUV and NIR radiations, a slight difference can be seen in the angle integrated yield of the obtained PAD. This difference determines the circular dichroism (see Eq. 4.2) [39]. As it was predicted in previous theoretical studies [77, 78, 86, 87], the circular dichroism is expected to be different for the low and high intensity regimes of the NIR laser beam. In the following parts of this section, the measured CDAD at an emission angle of 90° for the low- ($3 \times 10^{11} W/cm^2$) and high intensity regimes ($7.2 \times 10^{12} W/cm^2$) are discussed.

5.5.1 Circular Dichroism in Low Intensity NIR Fields

SFA predicts [87] that the largest dichroic effect in the photoelectron intensity appears at an emission angle of $\theta = 90°$. Figure 5.10 shows the CDAD for the low intensity NIR field ($3 \times 10^{11} W/cm^2$), where only one sideband appears on each side of the main photoline. As it was demonstrated by theoretical calculations based on the SFA [87], at a weak NIR peak intensity, the CDAD is expected to be a negative value for both sidebands, whereas for the main photoline this value is predicted to be positive. The same expectation is valid also for the angle-integrated circular dichroism (see Eq.2.17) [39].

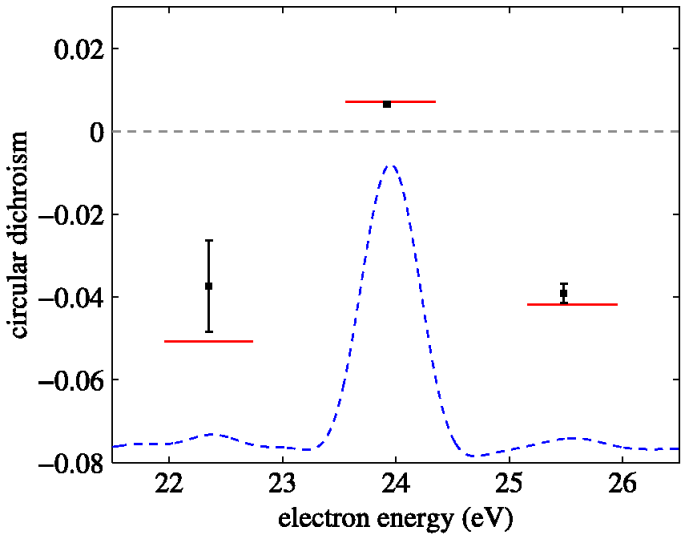

Figure 5.10: Experimentally determined CDADs at 90° emission angle for the central line and the sidebands for low intensity NIR field ($3 \times 10^{11}\, W/cm^2$). Experimental results are shown by dots with error bars. The dashed line represents the experimental photoelectron spectrum (the zero line is shifted for clarity) The CDADs extracted by the simulation are shown from red bars [39].

According to the predictions based on the perturbation theory (PT) (see Eq.2.38), the circular dichroism for high-energy- and low-energy-sidebands could be expected to have opposite signs under the present experimental conditions. This expectation can be inaccurate, as the transition probability for the final $s-$ and $d-$state (wave) for the two sidebands can be different. For the higher sideband (absorption of NIR photon) the transition into the s-state is more probable, whereas for the lower sideband (emission of NIR photon) a final state of a d-wave is favorable[39]. This aspect can be typical for non-resonant transitions into the continuum, when the following three conditions are satisfied [39]:

(a) The value of the continuum-continuum matrix elements is positive and has a monotonic behavior.

(b) Their reverse behavior with increasing and decreasing orbital quantum number.

(c) Small energy gap between two singularities $E' = \omega_{XUV}$ and $E' = E = \omega_{XUV} \pm \omega_{NIR}$ [39].

In the considered case, all of the three conditions are fulfilled. In the last condition (c) the NIR frequency has to be much lower than the XUV frequency ($\omega_{NIR} \ll \omega_{XUV}$). Therefore, by applying the perturbation theory, the sign of the circular dichroism for both higher- and lower-sidebands is negative, counter to the initial expectation [39].

5.5.2 Circular Dichroism in High Intensity NIR Fields

According to the SFA predictions [77, 78] for a strong NIR dressing field, the sign of the circular dichroism for the first higher sideband is positive, whereas, for the first lower sideband this value is expected to be negative. The circular dichroism of the main line is expected to be a small positive value. However, for the higher order

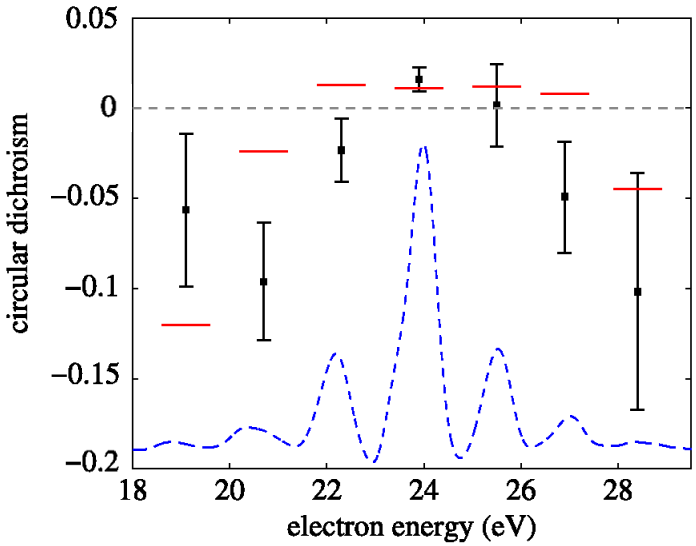

Figure 5.11: Experimentally determined CDADs at 90° emission angle for the central line and the sidebands for high intensity NIR fields ($7.2 \times 10^{12} W/cm^2$). Experimental results are shown by dots with error bars. The dashed line represents the experimental photoelectron spectrum (the zero line is shifted for clarity). The CDADs extracted from the simulation are shown by red bars [39].

sidebands on both sides of the main photoline, the circular dichroism is predicted

to have a negative sign and to increase in absolute value with the order of the sidebands [39].

The experimentally measured circular dichroism for the highly intense NIR field ($7.2 \times 10^{12} W/cm^2$) at an emission angle of 90° is plotted in figure 5.11. In the same figure the photoelectron spectrum for the case of co-rotating beams is displayed by the dashed line. The theoretically calculations for circular dichroism on the basis of SFA is displayed by red lines for each emission line of the photoelectron spectrum. The sign of the theoretically calculated value of the circular dichroism for the first sidebands on both sides of the main line are positive, which is not coinciding with the predictions from [77] and [78]. This is caused by the averaging over the intensity of the NIR field in the theoretical calculations for this experiment [39]. However, for higher order sidebands, which are mainly produced by the strong central part of the NIR radiation, the behavior of the circular dichroism, namely negative and increasing with the order of the sideband, is close to the predicted value by [77] and [78]. In case of the lower sidebands, the poor agreement between the theoretical and experimental values is due to the difficulties in extracting the experimental values for this energy range, as discussed before in this chapter [39].

5.6 Summary

In this chapter, a two-color (XUV and NIR) multi-photon ionization of helium with circularly polarized beams was demonstrated. The PAD was determined for each sideband. The experimentally obtained PADs have been simulated with two different theoretical approaches, namely SFA and PT [39]. Furthermore, it was shown that it is possible to observe the effect of alternating helicity of the NIR radiation (circular dichroism) in the angular distribution of photoelectrons and in the intensity of the sidebands, observed in the above threshold ionization of helium. The dependence of the PAD and the sideband intensities was discussed for two different intensity regimes of the NIR radiation ($3 \times 10^{11} W/cm^2$ and $7.2 \times 10^{12} W/cm^2$).

CHAPTER 6

Multi-photon Ionization of Oriented Helium Ions with Polarization Control

Investigations of the photoionization process with different polarization states of the ionizing radiation provide the possibility to obtain unique information about the interaction of light with the electronic structure of a target. In the previous chapter, the circular dichroism in the angular distribution of photoelectrons in the interaction of circularly polarized FEL pulses with helium atoms dressed by an optical laser was discussed.

The main goal of the experiment explained in this chapter is to develop a sensitive method to investigate the resonant ionization of ions with circularly polarized XUV radiation and NIR pulses. The chapter is based on reference [26]. The relevance of this experiment together with suggestions for future applications will be discussed. In this experiment, the sequential double ionization of helium ions is studied through a resonant two-color multi-photon ionization process. Helium ions created via one-photon ionization are subsequently excited by another XUV photon from the same FEL pulse to the He^+3p state. From there, they are further ionized by four NIR photons (see scheme in Fig. 6.1). This two-color multi-photon process was investigated experimentally and theoretically for different helicity combinations of the XUV and NIR pulses revealing distinct dichroic differences in the photoelectron angular distribution as well as in the respective ionization yields. Moreover, an unexpectedly strong dependency of the circular dichroism in the photoelectron yields on the intensity of the NIR pulses was observed, which is described in the following parts of this chapter.

The experiment was performed at the LDM endstation of the FERMI FEL-1 at Elettra, Italy. The advantage of pulses from the seeded FERMI FEL for this experiment was not only the availability of circular polarization, but also the tunability of the photon energy (19 - 62 eV) and especially the low energy bandwidth (1/500 - 1/1000). The low bandwidth of the radiation facilitates an exact tuning of the photon energy to a resonant electron transition in the target and prevents the undesired population of Rydberg states during the ionization process.

6.1 Excitation Scheme

In the present study, helium atoms are selected as target, since they are a theoretically well studied sample that provides access to well distinguishable processes of light-matter interaction. The helium atoms are ionized by a circularly polarized FEL pulse with a pulse duration of 100 fs $\pm$ 20 fs (FWHM of the intensity) and a photon energy of 48.37 eV (25.63 nm), corresponding to the 10^{th} harmonic of the FERMI seed laser. The average pulse energy of 47 μJ $\pm$ 6 μJ was achieved at 10 Hz repetition rate. The bandwidth of the XUV pulses in this experiment was determined to be about 100 meV. This narrow bandwidth is beneficial to excite helium ions (He^+ $1s$) to the He^+3p state by a second XUV photon. Since the FEL

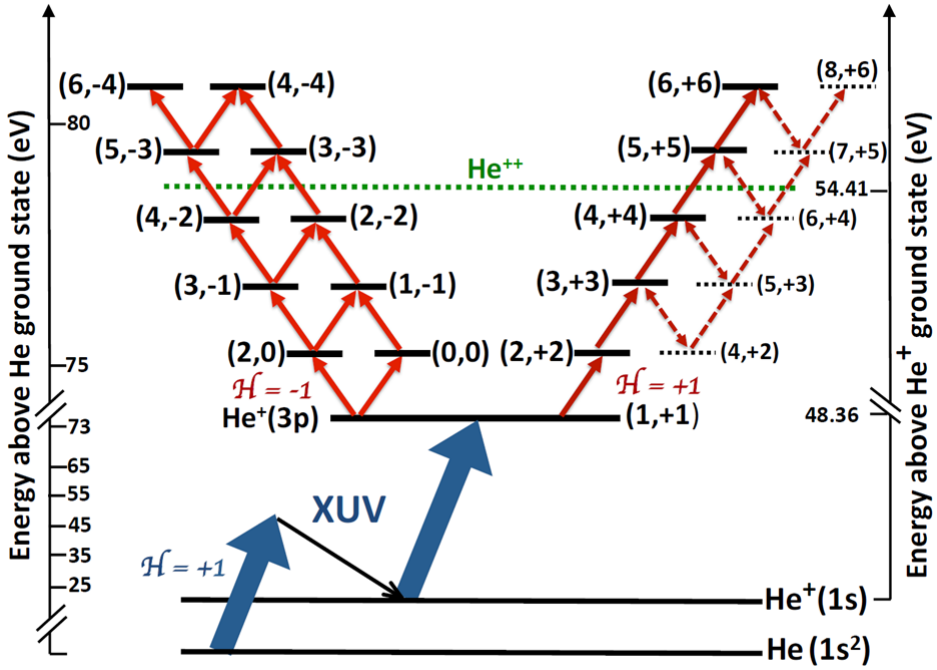

Figure 6.1: Scheme for sequential ionization of the neutral helium target. After the first FEL photon ($h\nu = 48.37\,eV$) creates $He^+(1s)$, the sequential absorption of a second FEL photon produces the oriented $He^+(3p, m = +1)$ state. From here, the energy needed for ionization is provided by an NIR laser with a photon energy of 1.58 eV ($\lambda = 784\,nm$) and changing helicities. The solid lines associated with the optical laser indicate the possible pathways in LOPT. An illustration of higher-order processes is shown as dashed lines on the right side. Only the latter can, in principle, provide more than one possible path for the co-rotating case that predominantly reaches the $(l, m) = (5, +5)$ continuum at the lowest (main) peak and the (6, +6) continuum in the first ATI peak [26].

radiation was set to a right-handed circular polarization state, the electron in the $1s$ ground state of the helium ion is transferred to the $3p, m = +1$ quantum state. The electrons transferred to this state are further ionized in a multiphoton absorption of a spatially overlapped and temporally synchronized NIR pulse. The photon energy of the NIR laser was 1.58 eV (784 nm central wavelength) and the bandwidth of the laser pulses was about 26 meV (13 nm). The laser pulses were either left- or right-polarized with a degree of polarization not less than 99%. The pulse duration of the NIR laser was about 175 fs with an average pulse energy of $604\,\mu\text{J} \pm 1.5\,\mu\text{J}$.

Figure 6.1 shows the experimental scheme with circularly polarized XUV and NIR photons. The He^+3p ion can be ionized in a multi-photon process through different channels depending on the relative helicity of the NIR photons to the XUV radiation (co- or counter-rotating). The most relevant cases within the lowest order perturbation theory are depicted as solid lines in the figure. Higher order pathways are indicated as dashed lines. In order to perform a multiphoton ionization of the excited helium ions ($He^+\,3p$), at least four NIR photons (from the same pulse) are needed to be absorbed, since the ionization threshold of He^+1s is at 54.41 eV. The excitation energy of the He^+3p state is equal to the chosen photon energy, i.e. 48.36 eV.

Since the ionization process in the current case occurs in a multiphoton regime, it is appropriate to theoretically study the process in a perturbation theory approach. In the calculations within the lowest order perturbation theory (LOPT), the absorption of a right-handed circularly polarized NIR photon increases the magnetic quantum number of the transfered electron by one unit, i.e. following the excitation pathway $(1,1) \rightarrow (2,2) \rightarrow (3,3) \rightarrow (4,4) \rightarrow (5,5)$. The intermediate levels are characterized by (l,m) with the angular momentum l and the magnetic quantum number m. In case of a left-handed NIR photon, the magnetic quantum number will decrease by one unit (see Fig.6.1), i.e. pathways such as $(1,1) \rightarrow (0,0)$ and $(1,1) \rightarrow (2,0)$ are possible for the first NIR photon. For a counter-rotating NIR pulse relative to the XUV radiation, there are different channels to transfer the electrons from the $He^+3p, m = +1$ state to continuum. As a result a more complex four-photon ionization scheme describes the process when opposite polarization are used for the XUV and the NIR pulses. This is due to the different orbital angular momenta of the excited electron.

In the current excitation scheme, the absorption of three NIR photons of the unperturbed system would lead to an excitation between the $He^+n = 6$ and $He^+n = 7$ states, with a separation of 0.2 eV from each of the states. Regarding the described experimental conditions with a narrow bandwidth below 100 meV and the later discussed results, it is not expected that these Rydberg states play a role for this particular experiment. However, they will be part of future investigations.

The theoretical calculations of the current experiment are performed in a two step model approach of helium sequential double ionization [26]. Within this approach, the calculations for the subsequent excitation to and ionization from the He^+3p

state were separately considered from the initial ionization process of producing the He^+1s ion. For the treatment of the processes in the ion, the non-relativistic time-dependent Schrödinger equation (TDSE) was solved numerically for an electron of the helium ion in the field of both, the circularly polarized XUV and NIR pulses [26].

Figure 6.2 shows the electron emission spectrum for the two cases of co-rotating (blue curve) and counter-rotating (red curve) circularly polarized NIR and XUV pulses at $1.4 \times 10^{12} W/cm^2$ NIR intensity. In this plot, the first main peak at about 150 meV electron kinetic energy corresponds to the four-NIR-photon ionization of the $He^+(3p)$ state, which was initially excited by the XUV pulse. At about 1.75 eV, another clearly visible peak appears in the photoelectron spectrum. This peak corresponds to the photoelectrons produced by an above threshold ionization with a fifth NIR photon.

As it can be observed in the figure 6.2 , there is a very strong difference (almost 40%) in the intensity of the main peak at 150 meV for the opposite helicities of the NIR pulses. This difference is mainly due to the fact that for the counter-rotating NIR pulses relative to the XUV the individual transition probabilities are much smaller than for the co-rotating pulses (see below). In addition, also for the case of counter-rotating photons, there are more possibilities for the transition of the electron into the continuum than for the co-rotating case, which may lead to interferences between the channels and a decrease of the signal.

The dichroism can also be observed in the angular distribution of the photoelectrons. Figure 6.3 shows the photoelectron angular distribution for the low energy peaks (four-photon absorption of the NIR beam) in a polar system containing the beam propagation axis, which is corresponding to the 0° in the plot. The XUV and NIR pulses are almost co-axially propagating. Therefore, the photoelectron angular distributions are cylindrically symmetric with respect to the beam propagation axis. The angular distributions of the photoelectrons for the co- and counter-rotating case of the NIR photons, are extremely different, as it can be seen in figure 6.3. In the co-rotating case (blue color), the angular distribution has a simple shape including two lobes at 90° and 270° along an axis perpendicular to the propagation direction of the pulses. However, for the counter-rotating NIR pulses (red color), the photoelectron angular distribution shows a more complex shape with four additional lobes about the angles 45°, 135°, 225° and 315°.

The difference in the angular distribution shape of the co- and counter-rotating case can be explained by the LOPT (see Fig.6.1 and section 2.5). For the co-rotating case, there is only one channel, which can produce the low kinetic energy photoelectrons (see Fig.6.3). The corresponding partial wave for the photoelectron with $l = 5$ with $m = +5$ can be characterized by $\mid Y_{5,+5}(\theta, \phi) \mid^2 \sim \sin^{10}\theta$.

In the case of counter-rotating fields, there are at least four different channels to transfer the $3p$, $m = +1$ electron of the helium ion into the continuum, where the corresponding partial waves are $l = 5$ and $l = 3$ both with $m = -3$. The more complex photoelectron angular distribution for this case can be calculated

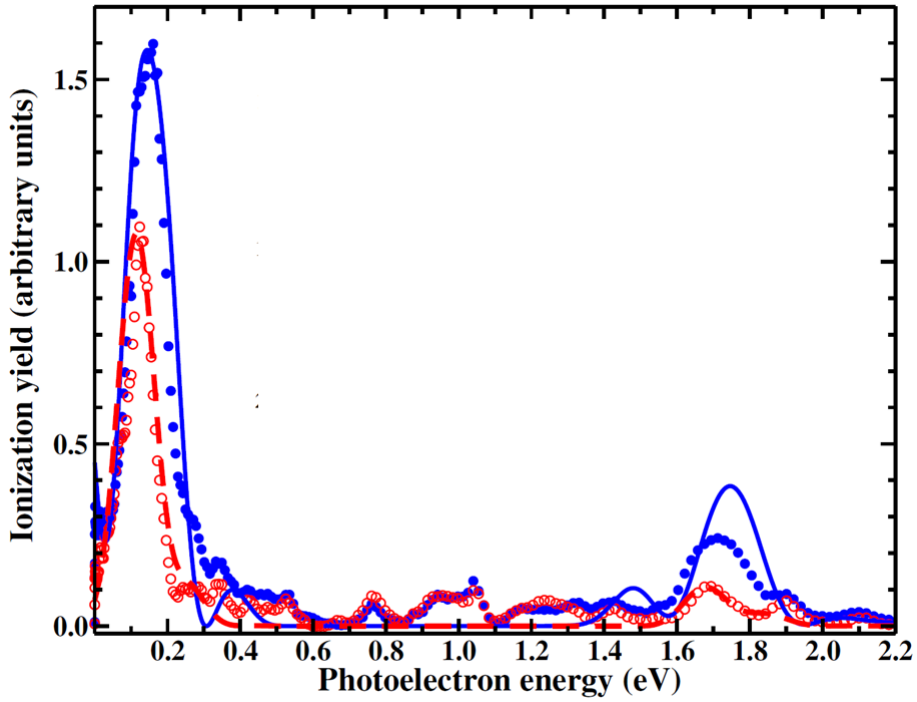

Figure 6.2: Experimental (symbols) and TDSE theoretical (lines) spectra of photoelectrons at an emission angle of 90° ± 5° (large inset) for co-rotating (blue, solid circles and line) and counter-rotating (red, open circles and dashed line) circular polarizations in the lowest peak [26].

by the absolute square superposition of $Y_{5,-3}(\theta,\phi)$ and $Y_{3,-3}(\theta,\phi)$, which includes an interference term [26]. The remaining possible channels for the transition of the electrons to the continuum, as indicated by the dashed lines in figure 1.1., contribute less than 0.1% to the low kinetic energy peak at 150 meV for both co- and counter-rotating pulses in figure 6.2.

6.2 NIR Intensity Dependence of the Circular Dichroism

The angle integrated circular dichroism was determined in the present experiment for two intensities $7.3 \times 10^{11}\,W/cm^2$ and $1.4 \times 10^{12}\,W/cm^2$) of the NIR pulses. This intensity range for the dynamic circular dichroism was additionally explored by theoretical calculations supporting the drastic decrease of the circular dichroism, and even indicating a circular dichroism sign change around $1.5 \times 10^{12}\,W/cm^2$ [26].

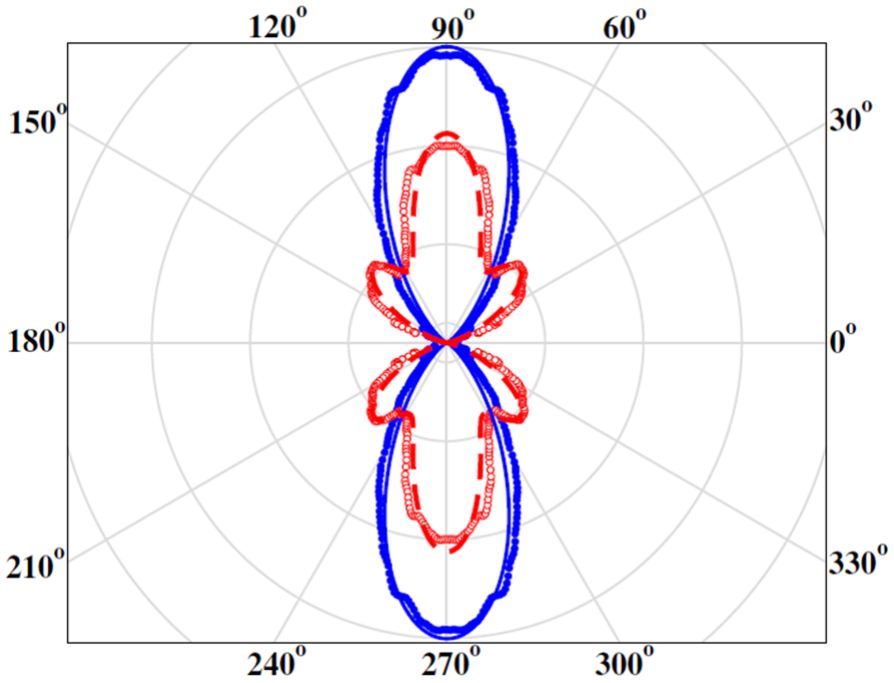

Figure 6.3: Angular distribution for co-rotating (blue) and counter-rotating (red) NIR pulses with the XUV radiation for the four-NIR-photon ionization signal from the $He^+(3p)$ state [26].

6.2.1 Circular Dichroism in the NIR Low Intensity Regime

The angle integrated circular dichroism for the low intensity regime of the NIR radiation at $7.3 \times 10^{11}\, W/cm^2$ was theoretically found to be 0.95, whereas the experimental value for this case is $0.98^{+0.02}_{-0.11}$.

The large positive value, shows that the four-NIR-photon ionization process of the excited helium ion in a low NIR intensity regime is more likely for the case of co-rotating rather than counter-rotating fields (see the right branch of Fig.6.1). This phenomenon can be qualitatively explained in terms of LOPT. For co-rotating fields, there is only one path to transfer the electron to the $l = 5\,, m = +5$ state in the continuum, which occurs through four dipole transitions shown in the right branch of the figure 6.1. These dipole transitions of the type $(l, m = l) \rightarrow (l+1, m = l+1)$ are the most favorable dipole transitions with an increasing l quantum number.

In the case of counter-rotating fields, there are two ionization paths by the absorption of four NIR photons, which end at the continuum states $l = 5\,, m = -3$ and $l = 3\,, m = -3$ (see the left branch of Fig.6.1). The probability of a dipole transition to the $l = 5\,, m = -3$ state was estimated from the angular factors to be about fifty times smaller than the case of co-rotating fields [26].

The electron transitions to the continuum state $l = 3\,, m = -3$ are a more

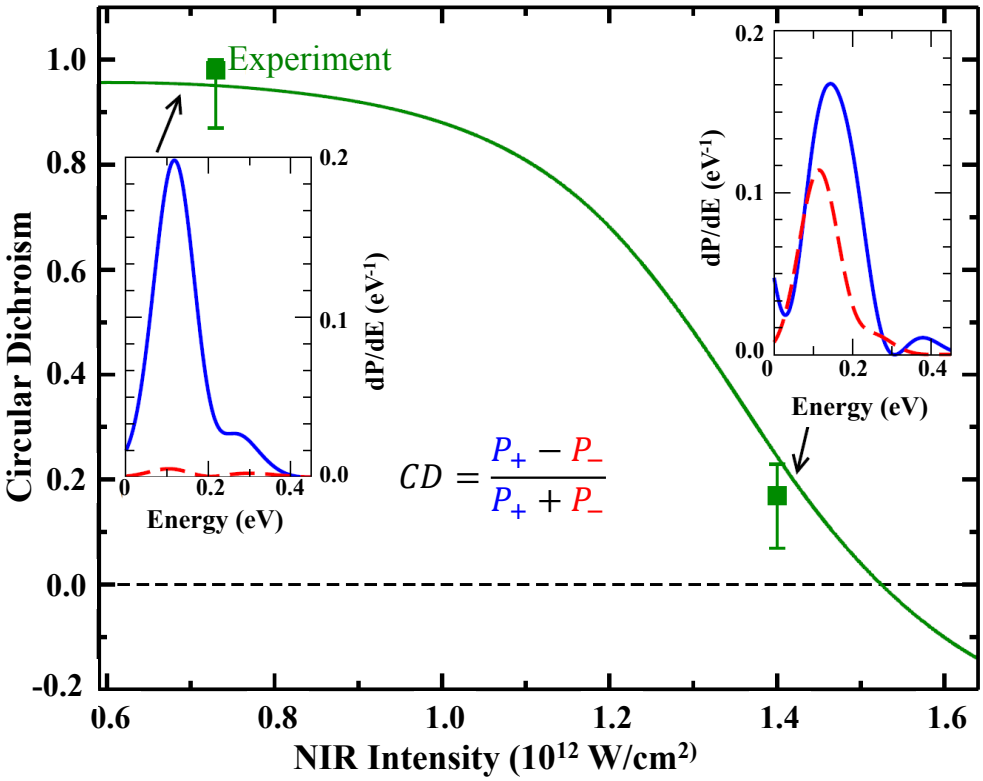

Figure 6.4: Circular dichroism in the peaks at 150 meV as function of the NIR peak intensity for an XUV peak intensity of $1.0 \times 10^{13} W/cm^2$. The two experimental points are compared with predictions from the TDSE theory. The insets show the low-energy spectra obtained in the TDSE model for the two experimental cases. [26].

complicated ionization case, which can be considered in the LOPT by four interfering paths involving different combinations of intermediate states with different angular momentum quantum numbers. Considering the small angular factors for these transitions and the possibility of destructive interference between the amplitudes of these paths, the ionization probability into the $l = 3\,, m = -3$ state is expected to be even slightly smaller than the transitions to $l = 5\,, m = -3$ state.

In the low intensity regime of the NIR radiation ($7.3 \times 10^{11}\, W/cm^2$), the result of theoretical calculations based on TDSE show that the ionization probabilities ($P_{l,m}$)in case of counter-rotating fields are $P_{5,-3} = 2.7 \times 10^{-4}$ and $P_{3,-3} = 2.3 \times 10^{-4}$, wheres for co-rotating this value is $P_{5,+5} = 1.5 \times 10^{-2}$, which is about two order of magnitudes higher than the counter-rotating case.

6.2.2 Intensity Dependent Circular Dichroism

The angle integrated circular dichroism at $1.4 \times 10^{12}\, W/cm^2$ was calculated to be 0.244 in the theory and the result of the experimental measurements for this

parameter was determined to be $0.169^{+0.06}_{-0.10}$.

Figure 6.4 shows the angle integrated circular dichroism as a function of the NIR intensity. Comparing the value of circular dichroism in the high intensity regime of the NIR radiation with the low intensity case, a clear decrease can be observed. Therefore, the question arises how is it possible that a relatively small increase in the NIR intensity can lead to such a large decrease in the value of the circular dichroism in this multiphoton ionization process. From literature concerning a similar case in hydrogen [62], it was expected that such a rapid change of yield between co- and counter-rotating occurs about an order of magnitude higher around $1 \times 10^{13} W/cm^2$. To find a proper explanation for this effect, it is helpful to study the electron population dependence on the NIR intensity in the helium ion ground state and the $He^+(3p, m = +1)$ state.

Figure 6.5 shows the electron population change of the excited $3p$ state with increasing NIR intensity for co- and counter-rotating fields. In case of low NIR intensity, the population of the $3p$ state is very high for both co- and counter-rotating XUV and NIR radiations. A high population means that the second XUV pulse indeed hits the resonance state $He^+(3p, m = +1)$ and transfers population from the $1s$ ground to the $3p$ excited state (see Fig.6.5).

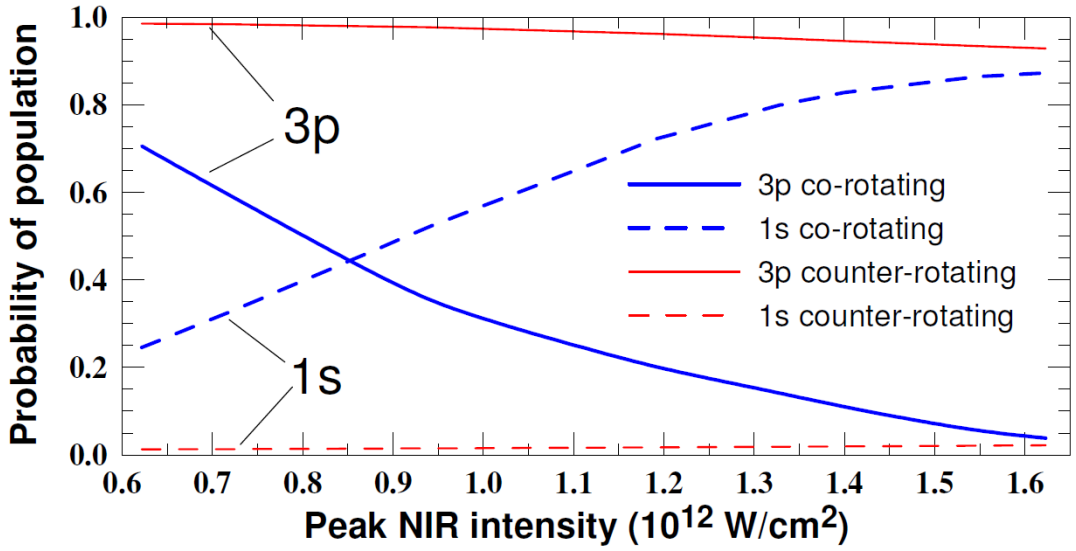

Figure 6.5: TDSE predictions for the populations of $He^+(1s)$ and $He^+(3p, m = +1)$ for the co- and counter-rotating cases at the end of the pulses as a function of the NIR peak intensity. [26].

When the NIR intensity increases, the interaction of the co-rotating light field with the ionic state $He^+3p, m = +1$ leads to a slight shift of its energy level that is associated with an AC Stark shift (Figure 6.2). However, this small shift is enough, so that the XUV pulse is not in resonance with the electron transition from the ionic ground state to the shifted $He^+3p, m = +1$ state and, therefore, the electron population in this state reduces significantly for the co-rotating case of the NIR

and XUV fields (see Fig.6.5). As a consequence, a large part of the helium ions will stay in the ground state $He^+(1s)$ and the ionization by a four-photon process becomes less efficient.

On the other hand, for counter-rotating fields, the population of the $He^+3p, m = +1$ state is almost not affected and therefore, the less favored NIR multiphoton ionization paths to the continuum states $l = 5\,,\, m = -3$ and $l = 3\,,\, m = -3$ become more probable in comparison to the case of co-rotating pulses. As a final result of this difference for both pathways, the change in population leads to a decrease in the circular dichroism and might even lead to a change of sign of the circular dichroism for higher intensities. There might be other mechanisms contributing in this process, however, the above discussed chain of events appears valid and can also be confirmed by the fact that for an increased intensity of the NIR by a factor of two, the ionization probability of the four-NIR-photon process (the area under the curve in the inset of Fig.6.4) for co-rotating fields should increase by a factor of 16 in the case that neglects a population change. However, this increase is compensated by the population decrease of $He^+(3p, m = +1)$ ions and the ionization probability stays almost constant.

6.3 Conclusion and Discussion

In the experiment discussed in this chapter, the electron of the He^+ ground state was transferred by a circularly polarized XUV pulse to the ionic $3p$ state with a magnetic quantum number of $m = +1$, which is an excited and oriented state. In the next step, the $He^+(3p, m = +1)$ ion was ionized by a co- or counter-rotating NIR laser field in a four photon process. Obtaining the circular dichroism of the released electrons provides an unprecedented approach to study electronic orientation in ionic resonances. Moreover, by varying the NIR intensity, the resonant absorption probability can be controlled due to a helicity dependent AC Stark shift.

The dichroic effect with AC Stark shift observed in this experiment has not been taken into account in other studies reported in recent literature, e.g. Bauer et al.[62], Barth and Smirnova [64] and Herath et al. [65]. For the first time, Bauer et al. developed a theoretical method to show the relevance of the sign change of the magnetic quantum number in studies covering the range from the multi-photon to the barrier suppression regime (BSI) in photoionization processes [62] (see chapter 2) without going through the tunneling regime that was studied by Barth and Smirnova for its properties of circular dichroism. This is realized by investigating excited states that are at the peak of the electric field of the laser lying over the potential barrier, therefore being part of the barrier suppression regime and not the tunneling regime. Bauer et al. conclude that excited states can play a non-negligible role even up to the the very high laser intensities of $> 1 \times 10^{14} W/cm^2$. 2.1.2). In the BSI region where the Keldiysh parameter $\gamma < 1$, the ionization rate for co- and counter-rotating electrons becomes almost the same [62, 64]. As it is discussed by Bauer et al., the ratio of the counter-rotating ionization rate to the one

of the co-rotating case was expected to grow practically monotonically by increasing the Keldysh parameter from the barrier suppression regime ($\gamma < 1$) to the multi-photon ionization regime ($\gamma > 1$) [62]. In contrast to these findings, according to previous theoretical studies performed by Popov et al. [61] the ionization rate of an atom and the photoelectron yield in adiabatic tunneling theories, do not even depend on the sign of the magnetic quantum number [62].

The first experiment for the observation of the relation between the sign of the magnetic quantum number and, in that case, strong laser field ionization rate was performed by Herath et al. [65], where the strong-field sequential double ionization yield of argon was measured by two time-delayed near-circularly polarized laser pulses. This experimental result was interpreted by Barth and Smirnova [63] in the tunnel ionization regime [62]. They claim that the counter-rotating electrons in the initial bound state should ionize preferentially over the co-rotating electrons for any Keldysh parameter $\gamma > 0$ [62]. They furthermore claim that excited states should only play a negligible role. However, both findings are in contrast to our findings and those of Bauer et al., respectively. The clarification of the apparent incongruity and a clear distinction between laser induced and general atomic properties will be subject of further investigations.

Turning back to the intriguing question of possible potential sign changes of the circular dichroism and the related findings of Bauer et al., for low laser intensities ($10^{11} - 10^{12} W/cm^2$) the ionization yield (photoelectron yield) in hydrogen atoms for the co-rotating initial state H $2s$ ($l = 1$, $m = +1$) is higher than in the counter-rotating state H $2s$ ($l = 1$, $m = -1$). However, this behavior is predicted to swap when the laser intensity is increased [62]. At the laser intensity of $10^{13}\, W/cm^2$ the ionization probability of the H $2s$ ($l = 1$, $m = -1$) state exceeds the ionization probability of the H $2s$ ($l = 1$, $m = +1$) state (see red circle in Fig.6.6) [62], which corresponds to a sign change of the circular dichroism.

In the work presented in this chapter, this sign change appears to be at about one order of magnitude lower NIR intensity, which we account to the population decrease of the initial resonance as discussed above. Future investigations will reveal if a compensation of the dichroic AC Stark shift by adapted FEL photon energies confirms the picture that Bauer et al. discusses. In any case, it is interesting to note that by relatively small changes of the NIR intensity, the dominance of the left- or right-handed circular polarization can be controlled.

6.3.1 Outlook

Potential future applications could be dichroic switches for resonance control. Another step to further develop this research, is to increase the optical laser intensity in order to confirm the theoretically predicted sign change of the circular dichroism. A further perspective should then experimentally approach the conditions of Bauer et al. by compensating the AC Stark shift by re-centering the FEL photon energy on the resonance, therefore re-establishing a non-perturbed population. In that case it will be possible to observe under which conditions the circular dichro-

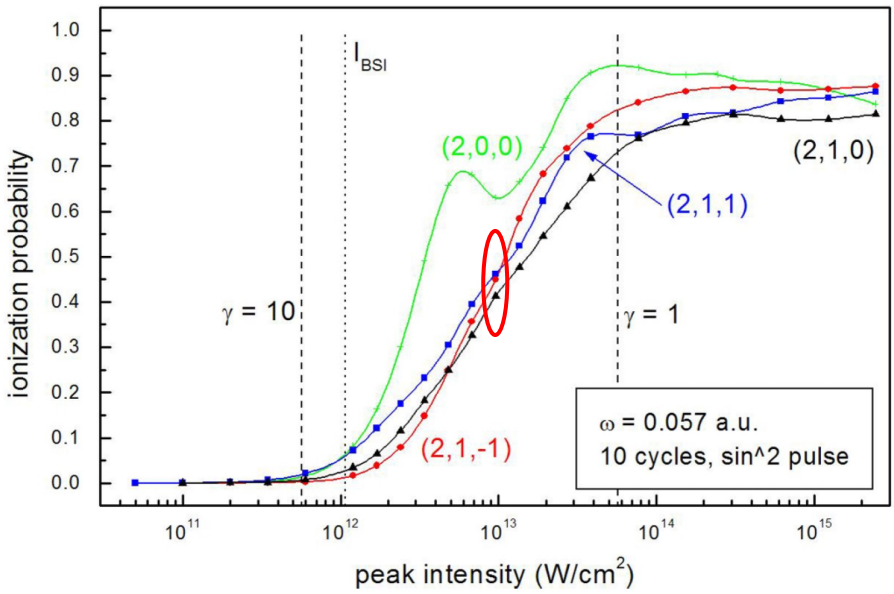

Figure 6.6: Comparison of ionization probabilities for the four initial states of the hydrogen atom as a function of the peak laser intensity. H $2s\,(l = 1, m = -1)$: red line with circles; H $2s\,(l = 1, m = +1)$: blue line with squares; H $2s\,(l = 1, m = 0)$: black line with triangles; H $2s\,(l = 0, m = 0)$: green line with crosses. Two vertical dashed lines correspond to fixed values of the Keldysh parameter γ , namely $\gamma = 10$ and $\gamma = 1$. (γ decreases from left to right.) The vertical dotted line shows $I_{BSI} = 1.1 \times 10^{12}\, W/cm^2$. The red circle marks the region where the sign of the CD changes. The figure and caption were taken from [62].

ism changes its sign with and without AC Stark shift. In order to achieve a full understanding of all underlying effects, it will also be very interesting to investigate the role of Rydberg resonances for the circular dichroism.

CHAPTER 7

Summary and Outlook

The studies in the context of this thesis were dedicated to two-color experiments with ultrashort optical laser pulses and XUV radiation, from different sources (HHG and FELs), for the investigation of electron properties and dynamics in small atomic targets. As a focus, the response of the electronic structure of the target to different helicities of circularly polarized radiation pulses was studied. The discussed topics in different chapters of this thesis are summarized in the following.

Chapter 3:

- The fundamental aspects af generating high order harmonics and the importance of these radiation sources was discussed.
- The setup of the HHG source at European XFEL, which was constructed in the context of this work was described in detail.
- The characterization of the high order harmonic radiation was presented.

As a complementary method to the FEL experiments, this setup is planned to be utilized for two-color pump-probe investigations on the fragmentation of molecules. In future steps, this HHG source is planned to be modified, in order to produce circularly polarized XUV radiation [158] for polarization dependent studies in atomic and molecular systems.

Chapter 4 and 5:

- The two-color photoionization processes of helium was used as tool for the characterization of circularly polarized FERMI FEL radiation.
- The first characterization of highly intense circularly polarized FEL radiation by the investigation of the circular dichroism of NIR-laser generated electron sidebands was performed. The pulse duration of the FERMI FEL as well as the polarization state and the circular polarization degree were obtained.
- The dependence of the photoelectron angular distribution to the intensity of the NIR laser beam was studied.

- The asymmetry parameters (β) have been obtained from the experimental data of the two-photon and multi-photon absorption processes of helium and were compared to the theoretical predictions based on strong field approximation and perturbation theory.

The next step is to investigate similar electron dynamics in a more complex atomic target.

Chapter 6:

- A more complex scheme of two-color multiphoton ionization has been used to study the dichroic properties of magnetic resonances (He^+3p, $m = +1$) and to control them via dichroic energy shifting of the resonance due to an AC Stark shift.
- In the two-color multi-photon ionization of He^+ with circularly polarized FEL and NIR photons, different ionization channels for the two polarization conditions of co- and counter-rotating beams, were studied.
- It was demonstrated that the circular dichroism can drastically change with the increase in the NIR peak intensity.

In future steps of this experimental scheme it is planed to compensate the AC Stark shift, in order to disentangle all underlying effects. In this context, it will also be very interesting to investigate the role of Rydberg resonances for the circular dichroism.

List of Abbreviations

ATI	Above Threshold Ionization
CD	Circular Dichroism
CDAD	Circular Dichroism in Angular Distribution of photoelectrons
CFD	Constant Fraction Discriminator
DESY	Deutsches Elektronen Synchrotron
FEL	Free-Electron laser
HGHG	High-Gain Harmonic-Generation
HHG	High Harmonic Generation
HSB	High Sideband (Higher Energy Sideband)
IAT	Inverse Abel Transformation
LCLS	Linac Coherent Light Source
LDAD	Linear Dichroism in Angular Distribution of photoelectrons
LDM	Low Density Matter
LOPT	Low Order Perturbation Theory
LSB	Low Sideband (Lower Energy Sideband)
MCP	Multi-Channel Plate
ML	Main Line (Main Photoline)
NIR	Near Infrared
OPA	Optical Parametric Amplifier
PAD	Photoelectron Angular Distribution
PSD	Position Sensitive Detector
PT	Perturbation Theory
TDC	Time-to-Digital Converter
TDSE	Time Dependent Schrödinger Equation
TOF	Time of Flight
SASE	Self-Amplified Spontaneous Emission
SB	Sideband
SFA	Strong Field Approximation
UHV	Ultra High Vacuum
UV	Ultraviolet
VMI	Velocity Map Imaging (Spectrometer)
VUV	Vacuum-Ultraviolet
XFEL	X-ray Free-Electron Laser
XUV	Extreme Ultra Violet
YAG	Ytterbium-Aluminum-Grant

Bibliography

[1] M. Schmitt, T. Mayerhöfer, J. Popp, I. Kleppe, and K. Weisshart. Light-matter Interaction. In *Handbook of Biophotonics*, chapter 3, pages 87–261. Wiley-VCH Verlag GmbH & Co. KGaA, **2011**.

[2] G. Günter, A. A. Anappara, J. Hees, A. Sell, G. Biasiol, L. Sorba, S. De Liberato, C. Ciuti, A. Tredicucci, A. Leitenstorfer, and R. Huber. Sub-cycle switch-on of ultrastrong light-matter interaction. *Nature*, 458(7235):178–181, **2009**.

[3] R. Hillenbrand, T. Taubner, and F. Keilmann. Phonon-enhanced light-matter interaction at the nanometre scale. *Nature*, 418(6894):159–162, **2002**.

[4] D. Shafir, Y. Mairesse, D. M. Villeneuve, P. B. Corkum, and N. Dudovich. Atomic wavefunctions probed through strong-field light-matter interaction. *Nature Physics*, 5(6):412–416, **2009**.

[5] A. Einstein. Über einen die erzeugung und verwandlung des lichtes betreffenden heuristischen gesichtspunkt. *Annalen der Physik*, 322(6):132–148, **1905**.

[6] T. Popmintchev, M. C. Chen, D. Popmintchev, P. Arpin, S. Brown, S. Ališauskas, G. Andriukaitis, T. Balciunas, O. D. Mucke, A. Pugzlys, A. Baltuska, B. Shim, S. E. Schrauth, A. Gaeta, C. Hernandez-Garcia, L. Plaja, A. Becker, A. Jaron-Becker, M. M. Murnane, and H. C. Kapteyn. Bright Coherent Ultrahigh Harmonics in the keV X-ray Regime from Mid-Infrared Femtosecond Lasers. *Science*, 336(6086):1287–1291, **2012**.

[7] H. Kapteyn, O. Cohen, I. Christov, and M. Murnane. Harnessing Attosecond Science in the Quest for Coherent X-rays. *Science*, 317(5839):775–778, **2007**.

[8] I. Christov, M. Murnane, and H. Kapteyn. High-Harmonic Generation of Attosecond Pulses in the "Single-Cycle" Regime. *Physical Review Letters*, 78(7):1251–1254, **1997**.

[9] P. M. Paul, E. S. Toma, P. Breger, G. Mullot, F. Augé, Ph. Balcou, H. G. Muller, and P. Agostini. Observation of a train of attosecond pulses from high harmonic generation. *Science*, 292(5522):1689–1692, **2001**.

[10] M. Drescher, M. Hentschel, R. Kienberger, M. Uiberacker, V. Yakovlev, A. Scrinzi, Th. Westerwalbesloh, U. Kleineberg, U. Heinzmann, and F. Krausz. Time-resolved atomic inner-shell spectroscopy. *Nature*, 419(6909):803–807, **2002**.

[11] F. R. Elder, A. M. Gurewitsch, R. V. Langmuir, and H. C. Pollock. Radiation from electrons in a synchrotron. *Physical Review*, 71(11):829–830, **1947**.

[12] P. Schmüser, M. Dohlus, and J. Rossbach. *Ultraviolet and Soft X-Ray Free-Electron Lasers*, volume 229. Springer-Verlag Berlin Heidelberg, **2008**.

[13] P. Willmott. *An introduction to synchrotron radiation*. John Wiley and Sons, Ltd, West Sussex, United Kingdom, **2011**.

[14] J. Als-Nielsen and D. Mc Morrow. *Elements of Modern X-Ray Physics*. John Wiley & Sons, Ltd, West Sussex, United Kingdom, **2001**.

[15] T. A. Assefa. *Tracking Chemical Reactions with Ultrafast X-ray Spectroscopic Techniques*. PhD thesis, Universität Hamburg, Von-Melle-Park 3, 20146 Hamburg, **2017**.

[16] M. J. Schmitt and C. J. Elliott. Even-harmonic generation in free-electron lasers. *Physical Review A*, 34:4843–4850, **1986**.

[17] Deutsches Elektronen Synchrotron (DESY). FLASH FEL. photon-science.desy.de/facilities/flash. (**accessed 14.02.2017**).

[18] A. A. Zholents. Method of an enhanced self-amplified spontaneous emission for x-ray free electron lasers. *Physical Review Accelerators and Beams*, 8:040701, **2005**.

[19] E. Allaria, B. Diviacco, C. Callegari, P. Finetti, B. Mahieu, J. Viefhaus, M. Zangrando, G. De Ninno, G. Lambert, E. Ferrari, J. Buck, M. Ilchen, B. Vodungbo, N. Mahne, C. Svetina, C. Spezzani, S. Di Mitri, G. Penco, M. Trovó, W. M. Fawley, P. R. Rebernik, D. Gauthier, C. Grazioli, M. Coreno, B. Ressel, A. Kivimäki, T. Mazza, L. Glaser, F. Scholz, J. Seltmann, P. Gessler, J. Grünert, A. De Fanis, M. Meyer, A. Knie, S. P. Moeller, L. Raimondi, F. Capotondi, E. Pedersoli, O. Plekan, M. B. Danailov, A. Demidovich, I. Nikolov, A. Abrami, J. Gautier, J. Lüning, P. Zeitoun, and L. Giannessi. Control of the polarization of a vacuum-ultraviolet, high-gain, free-electron laser. *Physical Review X*, 4(4):1–15, **2014**.

[20] Z. Zhao, D. Wang, J. Chen, Z. H. Chen, H. Deng, J. G. Ding, Ch. Feng, Q. Gu, M. M. Huang, T. Lan, Y. Leng, D. G. Li, G. Q. Lin, B. Liu, E. Prat, X. Wang, Z. S. Wang, K. R. Ye, L. Y. Yu, H. O. Zhang, J. Q. Zhang, M. Zhang, Mi. Zhang, T. Zhang, S. P. Zhong, and Q. G. Zhou. First lasing of an echo-enabled harmonic generation free-electron laser. *Nature Photonics*, 6(6):360–363, **2012**.

[21] A. Lindbald, S. Svensson, and K. Tiedtke. *A compandium on beam transport and beam diagnostic methods for Free Electron Lasers*. Deutsches Elektronen-Synchrotron DESY, Hamburg, Germany, **2011**.

[22] European XFEL. www.xfel.eu/overview/in_comparison. (**accessed 14.02.2017**).

[23] W. Ackermann et al. Operation of a free-electron laser from the extreme ultraviolet to the water window. *Nature Photonics*, 1(6):336–342, **2007**.

[24] N. J. Greenfield. Using circular dichroism spectra to estimate protein secondary structure. *Nature Protocols*, 1(6):2876–2890, **2007**.

[25] C. Von Korff Schmising, B. Pfau, M. Schneider, C. M. Günther, M. Giovannella, J. Perron, B. Vodungbo, L. Müller, F. Capotondi, E. Pedersoli, N. Mahne, J. Lüning, and S. Eisebitt. Imaging ultrafast demagnetization dynamics after a spatially localized optical excitation. *Physical Review Letters*, 112:217203, **2014**.

[26] M. Ilchen, N. Douguet, T. Mazza, **A. J. Rafipoor**, C. Callegari, P. Finetti, O. Plekan, K. C. Prince, A. Demidovich, C. Grazioli, L. Avaldi, P. Bolognesi, M. Coreno, M. Di Fraia, M. Devetta, Y. Ovcharenko, S. Düsterer, K. Ueda, K. Bartschat, A. N. Grum-Grzhimailo, A. V. Bozhevolnov, A. K. Kazansky, N. M. Kabachnik, and M. Meyer. Circular dichroism in multiphoton ionization of resonantly excited He^+ ions. *Physical Review Letters*, 118:013002, **2017**.

[27] E. Allaria et al. Highly coherent and stable pulses from the fermi seeded free-electron laser in the extreme ultraviolet. *Nature Photonics*, 6:699 – 704, **2012**.

[28] A. A. Lutman, J. P. MacArthur, M. Ilchen, A. O. Lindahl, J. Buck, R. N. Coffee, G. L. Dakovski, L. Dammann, Y. Ding, H. A. Dürr, L. Glaser, J. Grünert, G. Hartmann, N. Hartmann, D. Higley, K. Hirsch, Y. I. Levashov, A. Marinelli, T. Maxwell, A. Mitra, S. Moeller, T. Osipov, F. Peters, M. Planas, I. Shevchuk, W. F. Schlotter, F. Scholz, J. Seltmann, J. Viefhaus, P. Walter, Z. R. Wolf, Z. Huang, and H. D. Nuhn. Polarization control in an X-ray free-electron laser. *Nature Photonics*, 10:1–5, **2016**.

[29] G. Hartmann, A. O. Lindahl, A. Knie, N. Hartmann, A. A. Lutman, J. P. MacArthur, I. Shevchuk, J. Buck, A. Galler, J. M. Glownia, W. Helml, Z. Huang, N. M. Kabachnik, A. K. Kazansky, J. Liu, A. Marinelli, T. Mazza, H. D. Nuhn, P. Walter, J. Viefhaus, M. Meyer, S. Moeller, R. N. Coffee, and M. Ilchen. Circular dichroism measurements at an x-ray free-electron laser with polarization control. *Review Scientific Instruments*, 87(8), **2016**.

[30] A. Assion, M. Geisler, J. Helbing, V. Seyfried, and T. Baumert. Femtosecond pump-probe photoelectron spectroscopy: Mapping of vibrational wave-packet motion. *Physical Review A*, 54(6):R4605–R4608, **1996**.

[31] B. Wolfseder, L. Seidner, W. Domcke, G. Stock, M. Seel, S. Engleitner, and W. Zinth. Vibrational coherence in ultrafast electron-transfer dynamics of oxazine 1 in N,N-dimethylaniline: simulation of a femtosecond pump-probe experiment. *Chemical Physics*, 233(2-3):323–334, **1998**.

[32] A. A. Lutman, R. Coffee, Y. Ding, Z. Huang, J. Krzywinski, T. Maxwell, M. Messerschmidt, and H. D. Nuhn. Experimental demonstration of femtosecond two-color x-ray free-electron lasers. *Physical Review Letters*, 110:134801, **2013**.

[33] E. Ferrari, C. Spezzani, F. Fortuna, R. Delaunay, F. Vidal, I. Nikolov, P. Cinquegrana, B. Diviacco, D. Gauthier, G. Penco, P. R. Ribič, E. Roussel, M. Trovò, J. B. Moussy, T. Pincelli, L. Lounis, M. Manfredda, E. Pedersoli, F. Capotondi, C. Svetina, N. Mahne, M. Zangrando, L. Raimondi, A. Demidovich, L. Giannessi, G. De Ninno, M. B. Danailov, E. Allaria, and M. Sacchi. Widely tunable two-colour seeded free-electron laser source for resonant-pump resonant-probe magnetic scattering. *Nature Communications*, 7:10343, **2016**.

[34] T. Mazza, A. Karamatskou, M. Ilchen, S. Bakhtiarzadeh, **A.J. Rafipoor**, P. O'Keeffe, T. J. Kelly, N. Walsh, J. T. Costello, M. Meyer, and R. Santra. Sensitivity of nonlinear photoionization to resonance substructure in collective excitation. *Nature communications*, 6:6799, **2015**.

[35] N. Berrah, J. Bozek, J. T. Costello, S. Düsterer, L. Fang, J. Feldhaus, H. Fukuzawa, M. Hoener, Y. H. Jiang, P. Johnsson, E. T. Kennedy, M. Meyer, R. Moshammer, P. Radcliffe, M. Richter, A. Rouzée, A. Rudenko, A. A. Sorokin, K. Tiedtke, K. Ueda, J. Ullrich, and M. J. J. Vrakking. Non-linear processes in the interaction of atoms and molecules with intense EUV and X-ray fields from SASE free electron lasers (FELs). *Journal of Modern Optics*, 57(12):1015–1040, **2010**.

[36] A. A. Sorokin, S. V. Bobashev, T. Feigl, K. Tiedtke, H. Wabnitz, and M. Richter. Photoelectric effect at ultrahigh intensities. *Physical Review Letters*, 99(21):1–4, **2007**.

[37] M. Göppert-Mayer. Elementary processes with two quantum transitions. *Annalen der Physik*, 9:273–294, **1931**.

[38] W. Kaiser and C. Garrett. Two-Photon Excitation in CaF_2:Eu^{2+}. *Physical Review Letters*, 7(6):229–231, **1961**.

[39] T. Mazza, M. Ilchen, **A. J. Rafipoor**, C. Callegari, P. Finetti, O. Plekan, K. C. Prince, R. Richter, A. Demidovich, C. Grazioli, L. Avaldi, P. Bolognesi, M. Coreno, P. O'Keeffe, M. Di Fraia, M. Devetta, Y. Ovcharenko, V. Lyamayev, S. Düsterer, K. Ueda, J. T. Costello, E. V. Gryzlova, S. I. Strakhova, A. N. Grum-Grzhimailo, A. V. Bozhevolnov, A. K. Kazansky, N. M. Kabachnik, and M. Meyer. Angular distribution and circular dichroism in the two-colour XUV + NIR above-threshold ionization of helium. *Journal of Modern Optics*, 63(4):367–382, **2016**.

[40] M. Meyer, J. T. Costello, S. Düsterer, W. B. Li, and P. Radcliffe. Two-colour experiments in the gas phase. *Journal of Physics B: Atomic, Molecular and Optical Physics*, 43(19):194006, **2010**.

[41] M. Krikunova, Th. Maltezopoulos, A. Azima, M. Schlie, U. Frühling, H. Redlin, R. Kalms, S. Cunovic, N. M. Kabachnik, M. Wieland, and M. Drescher. Time-resolved ion spectrometry on xenon with the jitter-compensated soft x-ray pulses of a free-electron laser. *New Journal of Physics*, 11(12):123019, **2009**.

[42] M. Meyer, D. Cubaynes, V. Richardson, J. T. Costello, P. Radcliffe, W. B. Li, S. Düsterer, S. Fritzsche, A. Mihelic, K. G. Papamihail, and P. Lambropoulos. Two-photon excitation and relaxation of the $3d{-}4d$ resonance in atomic kr. *Physical Review Letters*, 104:213001, **2010**.

[43] V. Richardson, J. T. Costello, D. Cubaynes, S. Düsterer, J. Feldhaus, H. W. van der Hart, P. Juranić, W. B. Li, M. Meyer, M. Richter, A. A. Sorokin, and K. Tiedke. Two-photon inner-shell ionization in the extreme ultraviolet. *Physical Review Letters*, 105:013001, **2010**.

[44] L. Young, E. P. Kanter, B. Krässig, Y. Li, A. M. March, S. T. Pratt, R. Santra, S. H. Southworth, N. Rohringer, L. F. DiMauro, G. Doumy, C. A. Roedig, N. Berrah, L. Fang, M. Hoener, P. H. Bucksbaum, J. P. Cryan, S. Ghimire, J. M. Glownia, D. A. Reis, J. D. Bozek, C. Bostedt, and M. Messerschmidt. Femtosecond electronic response of atoms to ultra-intense X-rays. *Nature*, 466(7302):56–61, **2010**.

[45] G. A. Garcia, L. Nahon, S. Daly, and I. Powis. Vibrationally induced inversion of photoelectron forward-backward asymmetry in chiral molecule photoionization by circularly polarized light. *Nature communications*, 4:2132, **2013**.

[46] M. Pitzer, M. Kunitski, A. S. Johnson, T. Jahnke, H. Sann, F. Sturm, L. Ph. H. Schmidt, H. Schmidt-Böcking, R. Dörner, J. Stohner, J. Kiedrowski, M. Reggelin, S. Marquardt, A. Schießer, R. Berger, and M. S. Schöffler. Direct determination of absolute molecular stereochemistry in gas phase by coulomb explosion imaging. *Science*, 341(6150):1096–1100, **2013**.

[47] T. Mazza, M. Ilchen, **A. J. Rafipoor**, C. Callegari, P. Finetti, O. Plekan, Kevin C. Prince, R. Richter, M. B. Danailov, A. Demidovich, G. De Ninno, C. Grazioli, R. Ivanov, N. Mahne, L. Raimondi, C. Svetina, L. Avaldi, P. Bolognesi, M. Coreno, P. O'Keeffe, M. Di Fraia, M. Devetta, Y. Ovcharenko, Th. Möller, V. Lyamayev, F. Stienkemeier, S. Düsterer, K. Ueda, J. T. Costello, A. K. Kazansky, N. M. Kabachnik, and M. Meyer. Determining the polarization state of an extreme ultraviolet free-electron laser beam using atomic circular dichroism. *Nature communications*, 5:3648, **2014**.

[48] V. Schmidt. *Electron Spectroscopy of Atoms using Synchrotron Radiation*. Cambridge University Press, New York, **1997**.

[49] U. Becker and D. A. Shirley. *VUV and Soft X-Ray Photoionization*. Plenum Press, New York and London, **1996**.

[50] E. Fermi. Quantum theory of radiation. *Review Modern Physics*, 4:87–132, **1932**.

[51] J. W. Cooper. Photoionization from outer atomic subshells. a model study. *Physical Review*, 128:681–693, **1962**.

[52] S. Manson. Atomic photoelectron spectroscopy. *Advances in Electronics and Electron Physics*, 41:73–111, **1976**.

[53] J. W. Cooper. pages 31–48. Springer US, Boston, MA, **1976**.

[54] L. V. Keldysh. Ionization in the field of a string electromagnetic wave. *Journal of Experimental and Theoretical Physics*, 20(5):1307–1314, **1965**.

[55] C. Rullière. Attosecond Pulses. In *Femtosecond Laser Pulses: Principles and Experiments*, chapter 12, pages 1 – 428. Springer Science+Business Media, Inc., 233 Spring Street, New York, NY 10013, USA, **2005**.

[56] M. Protopapas, C. H. Keitel, and P. L. Knight. Atomic physics with super-high intensity lasers. *Reports on Progress in Physics*, 60(4):389–486, **1997**.

[57] F. X. Kärtner. Ultrafast Optical Physics II. 17(2003):1–17, **2013**.

[58] J. Parker and C. W. Clark. Study of a plane-wave final-state theory of above-threshold ionization and harmonic generation. *Journal of the Optical Society of America*, 13(2):371–379, **1996**.

[59] E. Cormier and P. Lambropoulos. Optimal gauge and gauge invariance in non-perturbative time-dependent calculation of above-threshold ionization. *Journal of Physics B: Atomic, Molecular and Optical Physics*, 29(9):1667–1680, **1999**.

[60] P. B. Corkum. Plasma perspective on strong field multiphoton ionization. *Physical Review Letters*, 71:1994–1997, **1993**.

[61] V. S. Popov. Tunnel and multiphoton ionization of atoms and ions in a strong laser field (keldysh theory). *Physics-Uspekhi*, 47(9):855, **2004**.

[62] J. H. Bauer, F. Mota-Furtado, P. F. O'Mahony, B. Piraux, and K. Warda. Ionization and excitation of the excited hydrogen atom in strong circularly polarized laser fields. *Physical Review A - Atomic, Molecular, and Optical Physics*, 90(6):2–7, **2014**.

[63] I. Barth and O. Smirnova. Nonadiabatic tunneling in circularly polarized laser fields. II. Derivation of formulas. *Physical Review A - Atomic, Molecular, and Optical Physics*, 87(1):1–16, **2013**.

[64] I. Barth and O. Smirnova. Nonadiabatic tunneling in circularly polarized laser fields: Physical picture and calculations. *Physical Review A - Atomic, Molecular, and Optical Physics*, 84(6):1–5, **2011**.

[65] Th. Herath, L. Yan, S. K. Lee, and W. Li. Strong-field ionization rate depends on the sign of the magnetic quantum number. *Physical Review Letters*, 109(4):1–5, **2012**.

[66] M. Ilchen, T. Mazza, E. T. Karamatskos, D. Markellos, S. Bakhtiarzadeh, **A. J. Rafipoor**, T. J. Kelly, N. Walsh, J. T. Costello, P. O'Keeffe, N. Gerken, M. Martins, P. Lambropoulos, and M. Meyer. Two-electron processes in multiple ionization under strong soft-x-ray radiation. *Physical Review A - Atomic, Molecular, and Optical Physics*, 94(1):1–6, **2016**.

[67] V. P. Krainov and N. B. Delone. AC Stark shift of atomic energy levels. *Physics-Uspekhi*, 42(7):669, **1999**.

[68] O. Hemmers. *Korrelationseffekte in kleinen Molekülen*. PhD thesis, Technischen Universität Berlin, **1993**.

[69] C. N. Yang. On the angular distribution in nuclear reactions and coincidence measurements. *Physical Review*, 74:764–772, **1948**.

[70] J. Cooper and R. N. Zare. Angular distribution of photoelectrons. *The Journal of Chemical Physics*, 48(2), **1968**.

[71] J. A. R. Samson and A. F. Starace. Effect of elliptically polarized light on the angular distribution of photoelectrons. *Journal of Physics B: Atomic and Molecular Physics*, 8(11):1806–1809, **1975**.

[72] V. Schmidt. Angular distribution of photoelectrons after photoionization by elliptically polarized light. *Physics Letters A*, 45(1):63–64, **1973**.

[73] A. N. Grum-Grzhimailo and M. Meyer. Magnetic dichroism in atomic core level photoemission. *European Physical Journal: Special Topics*, 169(1):43–50, **2009**.

[74] K. Starke. *Magnetic Dichroism in Core-Level Photoemission*. Springer Tracts in Modern Physics. Springer Berlin Heidelberg, **2013**.

[75] I. Powis. Photoelectron circular dichroism of the randomly oriented chiral molecules glyceraldehyde and lactic acid. *The Journal of Chemical Physics*, 112(1), **2000**.

[76] C. E. Graves et al. Nanoscale spin reversal by non-local angular momentum transfer following ultrafast laser excitation in ferrimagnetic GdFeCo. *Nature Materials*, 12(4):293–8, **2013**.

[77] A. K. Kazansky, A. V. Grigorieva, and N. M. Kabachnik. Circular dichroism in laser-assisted short-pulse photoionization. *Physical Review Letters*, 107(25):1–5, **2011**.

[78] A. K. Kazansky, A. V. Grigorieva, and N. M. Kabachnik. Dichroism in short-pulse two-color xuv plus ir multiphoton ionization of atoms. *Physical Review A*, 85:053409, **2012**.

[79] N. L. Manakov, A. Maquet, S. I. Marmo, V. Veniard, and G. Ferrante. Elliptic dichroism and angular distribution of electrons in two-photon ionization of atoms. *Journal of Physics B: Atomic, Molecular and Optical Physics*, 32(15):3747–3767, **1999**.

[80] H. Kleinpoppen, B. Lohmann, and A. N. Grum-Grzhimailo. *Perfect/Complete Scattering Experiments Probing Quantum Mechanics on Atomic and Molecular Collisions and Coincidences*, volume 75. Springer-Verlag Berlin Heidelberg, **2013**.

[81] D. M. Wolkow. Über eine klasse von lösungen der diracschen gleichung. *Zeitschrift für Physik*, 94(3-4):250–260, **1935**.

[82] A. N. Grum-Grzhimailo and E. V. Gryzlova. Nondipole effects in the angular distribution of photoelectrons in two-photon two-color above-threshold atomic ionization. *Physical Review A*, 89:043424, **2014**.

[83] P. Radcliffe, S. Düsterer, A. Azima, H. Redlin, J. Feldhaus, J. Dardis, K. Kavanagh, H. Luna, J. Pedregosa Gutierrez, P. Yeates, E. T. Kennedy, J. T. Costello, A. Delserieys, C. L. S. Lewis, R. Taïeb, A. Maquet, D. Cubaynes, and M. Meyer. Single-shot characterization of independent femtosecond extreme ultraviolet free electron and infrared laser pulses. *Applied Physics Letters*, 90(13):–, **2007**.

[84] P. Lambropoulos. Effect of light polarization on multiphoton ionization of atoms. *Physical Review Letters*, 28(10):585–587, **1972**.

[85] Th. Mercouris, Y. Komninos, S. Dionissopoulou, and C. A. Nicolaides. Computation of strong-field multiphoton processes in polyelectronic atoms: State-specific method and applications to H and Li^-. *Phys. Rev. A*, 50:4109–4121, **1994**.

[86] A. N. Grum-Grzhimailo and E. V. Gryzlova. Nondipole effects in the angular distribution of photoelectrons in two-photon two-color above-threshold atomic ionization. *Physical Review A - Atomic, Molecular, and Optical Physics*, 89(4):1–12, **2014**.

[87] A. K. Kazansky, A. V. Bozhevolnov, I. P. Sazhina, and N. M. Kabachnik. Circular dichroism in XUV + IR multiphoton ionization of atoms. *Journal of Physics B: Atomic, Molecular and Optical Physics*, 47(6):65602, **2014**.

[88] M. Hoener et al. Ultraintense x-ray induced ionization, dissociation, and frustrated absorption in molecular nitrogen. *Physical Review Letters*, 104(25):1–5, **2010**.

[89] D. Hochstuhl and M. Bonitz. Time-dependent restricted-active-space configuration-interaction method for the photoionization of many-electron atoms. *Physical Review A - Atomic, Molecular, and Optical Physics*, 86(5):1–12, **2012**.

[90] N. Dhenadhayalan and C. Selvaraju. Photoinduced electron transfer reaction of coumarin 307 with aromatic amines in soft matter : Role of photoionization on the dynamics and mechanism of electron transfer. *The Journal of Physical Chemistry*, 8:4908–4920, **2012**.

[91] J. Zhou, J. Peatross, M. Murnane, H. Kapteyn, and I. Christov. Enhanced High-Harmonic Generation Using 25 fs Laser Pulses. *Phyical Review Letters*, 76(5):752–755, **1996**.

[92] S. Kim, J. Jin, Y. J. Kim, I. Y. Park, Y. Kim, and S. W. Kim. High-harmonic generation by resonant plasmon field enhancement. *Nature*, 453(7196):757–60, **2008**.

[93] B. K. McFarland, J. P. Farrell, P. H. Bucksbaum, and M. Gühr. High harmonic generation from multiple orbitals in N2. *Science (New York, N.Y.)*, 322(5905):1232–1235, **2008**.

[94] P. A. Franken, A. E. Hill, C. W. Peters, and G. Weinreich. Generation of optical harmonics. *Physical Review Letters*, 7(4):118–119, **1961**.

[95] J. F. Ward and G. H. C. New. Optical third harmonic generation in gases. *Physical Review Letters*, 19(10):556, **1967**.

[96] J. L. Krause, K. J. Schafer, and K. C. Kulander. High-order harmonic generation from atoms and ions in the high intensity regime. *Physical Review Letters*, 68:3535–3538, **1992**.

[97] A. Averchi, D. Faccio, R. Berlasso, M. Kolesik, J. V. Moloney, A. Couairon, and P. Di Trapani. Phase matching with pulsed Bessel beams for high-order harmonic generation. *Physical Review A - Atomic, Molecular, and Optical Physics*, 77(2):4–7, **2008**.

[98] A. McPherson, G. Gibson, H. Jara, U. Johann, T. S. Luk, I. A. McIntyre, K. Boyer, and C. K. Rhodes. Studies of multiphoton production of vacuum-ultraviolet radiation in the rare gases. *Journal of the Optical Society of America B*, 4(4):595, **1987**.

[99] M. Ivanov, T. Brabec, and N. Burnett. Coulomb corrections and polarization effects in high-intensity high-harmonic emission. *Physical Review A*, 54(1):742–745, **1996**.

[100] M. Lewenstein, Ph. Balcou, M. Yu. Ivanov, A. L'Huillier, and P. B. Corkum. Theory of high-harmonic generation by low-frequency laser fields. *Physical Review A*, 49(3):2117–2132, **1994**.

[101] R. Santra and A. Gordon. Three-step model for high-harmonic generation in many-electron systems. *Physical Review Letters*, 96(7):1–4, **2006**.

[102] Lebow company. www.lebowcompany.com/. (**accessed 14.09.2016**).

[103] Amsterdam piezovalve company. www.amsterdampiezovalve.com/. (**accessed 14.02.2017**).

[104] Beam Dynamics Inc. Beam dynamics inc. www.beamdynamicsinc.com/. (**accessed 14.02.2017**).

[105] O. Hemmers, S. B. Whitfield, P. Glans, H. Wang, D. W. Lindle, R. Wehlitz, and I. A. Sellin. High-resolution electron time-of-flight apparatus for the soft x-ray region. *Review of Scientific Instruments*, 69(11):3809–3817, **1998**.

[106] A. Paulus, C. Winterfeldt, T. Pfeifer, D. Walter, G. Gerber, and C. Spielmann. Novel time-of-flight electron spectrometer optimized for time-resolved soft-x-ray photoelectron spectroscopy. *Review of Scientific Instruments*, 77(4), **2006**.

[107] W. E. Stephens. A pulsed mass spectrometer with time dispersion. *Physical Review*, 69(11-1):691–691, **1946**.

[108] P. Kruit and F. H. Read. Magnetic field paralleliser for 2π electron-spectrometer and electron-image magnifier. *Journal of Physics E: Scientific Instruments*, 16(4):313, **1983**.

[109] H. Wollnik, U. Grüner, and G. Li. *Time-of-Flight Mass Spectrometers*, pages 117–131. Springer Netherlands, Dordrecht, **1992**.

[110] Stefan kaesdorf. www.stefankaesdorf.de,(**accessed 14.02.2017**).

[111] W. C. Wiley and I. H. McLaren. Time-of-flight mass spectrometer with improved resolution. *Review of Scientific Instruments*, 26(12):1150–1157, **1955**.

[112] RoentDek Handels. MCP Delay Line Detector Manual (11.0.1601.1). www.roentdek.com/manuals,(**accessed 25.03.2017**).

[113] M. J. J. Vrakking. An iterative procedure for the inversion of two-dimensional ion/photoelectron imaging experiments. *Review of Scientific Instruments*, 72(11):4084, **2001**.

[114] P. OKeeffe, P. Bolognesi, M. Coreno, A. Moise, R. Richter, G. Cautero, L. Stebel, R. Sergo, L. Pravica, Y. Ovcharenko, and L. Avaldi. A photoelectron velocity map imaging spectrometer for experiments combining synchrotron and laser radiations. *Review of Scientific Instruments*, 82(3):0–8, **2011**.

[115] P. O'Keeffe, V. Feyer, P. Bolognesi, M. Coreno, C. Callegari, G. Cautero, A. Moise, K. C. Prince, R. Richter, R. Sergo, M. Alagia, M. De Simone, A. Kivimaeki, M. Devetta, T. Mazza, P. Piseri, V. Lyamayev, R. Katzy, F. Stienkemeier, Y. Ovcharenko, T. Möller, and L. Avaldi. A velocity map imaging apparatus for gas phase studies at FERMI@Elettra. *Nuclear Instruments and Methods in Physics Research, Section B: Beam Interactions with Materials and Atoms*, 284:69–73, **2012**.

[116] G. A. Garcia, H. Soldi-Lose, and L. Nahon. A versatile electron-ion coincidence spectrometer for photoelectron momentum imaging and threshold spectroscopy on mass selected ions using synchrotron radiation. *Review of Scientific Instruments*, 80(2):023102, **2009**.

[117] D. H. Parker and A. T. J. B. Eppink. Photoelectron and photofragment velocity map imaging of state-selected molecular oxygen dissociation/ionization dynamics. *Journal of Chemical Physics*, 107(7):2357, **1997**.

[118] M. Lavollée. A new detector for measuring three-dimensional momenta of charged particles in coincidence. *Review Scientific Instruments*, 70(7):2968–2974, **1999**.

[119] I. Ali, R. Dörner, O. Jagutzki, S. Nüttgens, V. Mergel, L. Spielberger, Kh. Khayyat, T. Vogt, H. Bräuning, K. Ullmann, R. Moshammer, J. Ullrich, S. Hagmann, K. O. Groeneveld, C. L. Cocke, and H. Schmidt-Böcking. Multi-hit detector system for complete momentum balance in spectroscopy

in molecular fragmentation processes. *Nuclear Instruments and Methods in Physics Research Section B: Beam Interactions with Materials and Atoms*, 149(4):490–500, **1999**.

[120] G. Cautero, R. Sergo, L. Stebel, P. Lacovig, P. Pittana, M. Predonzani, and S. Carrato. A two-dimensional detector for pump-and-probe and time resolved experiments. *Nuclear Instruments and Methods in Physics Research, Section A: Accelerators, Spectrometers, Detectors and Associated Equipment*, 595(2):447–459, **2008**.

[121] O. Ghafur, W. Siu, P. Johnsson, M. F. Kling, M. Drescher, and M. J. J. Vrakking. A velocity map imaging detector with an integrated gas injection system. *Review of Scientific Instruments*, 80(3), **2009**.

[122] P. Johnsson, A. Rouzee, W. Siu, Y. Huismans, F. Lepine, T. Marchenko, S. Duesterer, F. Tavella, N. Stojanovic, A. Azima, R. Treusch, M. F. Kling, and M. J. J. Vrakking. Field-free molecular alignment probed by the free electron laser in Hamburg (FLASH). *Journal of Physics B: Atomic, Molecular and Optical Physics*, 42:134017, **2009**.

[123] M. Yu. Kuchiev and V. N. Ostrovsky. Multiphoton radiative recombination of electron assisted by a laser field. *Physical Review A*, 61:033414, **2000**.

[124] K. Midorikawa. Ultrafast dynamic imaging. *Nature Photonics*, 5(11):640–641, **2011**.

[125] W. Becker, S. Long, and J. K. McIver. Modeling harmonic generation by a zero-range potential. *Physical Review A*, 50(2):1540–1560, **1994**.

[126] P. Antoine, A. L'Huillier, M. Lewenstein, P. Salières, and B. Carré. Theory of high-order harmonic generation by an elliptically polarized laser field. *Physical Review A*, 53(3):1725–1745, **1996**.

[127] N. H. Burnett, C. Kan, and P. B. Corkum. Ellipticity and polarization effects in harmonic generation in ionizing neon. *Physical Review A*, 51(5):3418–3421, **1995**.

[128] D. Schulze, M. Dörr, G. Sommerer, J. Ludwig, P. V. Nickles, T. Schlegel, W. Sandner, M. Drescher, U. Kleineberg, and U. Heinzmann. Polarization of the 61st harmonic from 1053-nm laser radiation in neon. *Physical Review A*, 57:3003–3007, **1998**.

[129] P. Jaeglé. *Coherent sources of XUV radiation : soft X-ray lasers and high-order harmonic generation*, volume 106. **2006**.

[130] X. F. Li, A. Lhuillier, M. Ferray, L. A. Lompré, and G. Mainfray. Multiple-harmonic generation in rare gases at high laser intensity. *Physical Review A*, 39(11):5751–5761, **1989**.

[131] P. W. Milonni and J. H. Eberly. *Laser Physics*, volume 53. John Wiley and Sons, Inc., Hoboken, New Jersey, **2010**.

[132] A. A. Zozulya, D. Z. Anderson, and M. Saffman. Control of mutual spatial coherence of temporal features by reflexive photorefractive coupling. *Journal of the Optical Society of America B-Optical Physics*, 13(1):41–49, **1996**.

[133] C. Winterfeldt, Ch. Spielmann, and G. Gerber. Colloquium: Optimal control of high-harmonic generation. *Reviews of Modern Physics*, 80(1):117–140, **2008**.

[134] A. E. Siegman. *Lasers*. University Science Books Sausalito, California, 55D Gate Five Road Sausalito, CA 94965, **1986**.

[135] C. Delfin, C. Altucci, F. De Filippo, C. De Lisio, M. B. Gaarde, A. L'Huillier, L. Roos, and C. G. Wahlström. Influence of the medium length on high-order harmonic generation. *Journal of Physics B: Atomic, Molecular and Optical Physics*, 32(22):5397–5409, **1999**.

[136] A. L. Lytle. *Phase Matching and Coherence of High-Order Harmonic Generation in Hollow Waveguides*. PhD thesis, University of Colorado, Department Physics, Duane Physics E1B32, 2000 Colorado Ave, Boulder, **2008**.

[137] EQ photonics. UV-photodiodes. www.eqphotonics.de,(**accessed 22.03.2017**).

[138] **.**

[139] T. Leitner. *Ultrafast processes in molecules visualized with femtosecond pump-probe photoelectron spectroscopy*. PhD thesis, Technischen Universität Berlin, Helmholtz-Zentrum Berlin für Materialien und Energie, Hahn-Meitner-Platz 1, 14109 Berlin, **2012**.

[140] T. E. Glover, R. W. Schoenlein, A. H. Chin, and C. V. Shank. Observation of laser assisted photoelectric effect and femtosecond high order harmonic radiation. *Physical Review Letters*, 76:2468–2471, **1996**.

[141] E. S. Toma, H. G. Muller, P. M. Paul, P. Breger, M. Cheret, P. Agostini, C. Le Blanc, G. Mullot, and G. Cheriaux. Ponderomotive streaking of the ionization potential as a method for measuring pulse durations in the xuv domain with fs resolution. *Physical Review A*, 62:061801, **2000**.

[142] M. Meyer, D. Cubaynes, P. O'Keeffe, H. Luna, P. Yeates, E. T. Kennedy, J. T. Costello, P. Orr, R. Taïeb, A. Maquet, S. Düsterer, P. Radcliffe, H. Redlin, A. Azima, E. Plönjes, and J. Feldhaus. Two-color photoionization in xuv free-electron and visible laser fields. *Physical Review A*, 74:011401, **2006**.

[143] J. Mauritsson, P. Johnsson, R. López-Martens, K. Varjú, W. Kornelis, J. Biegert, U. Keller, M. B. Gaarde, K. J. Schafer, and A. L'Huillier. Measurement and control of the frequency chirp rate of high-order harmonic pulses. *Physical Review A*, 70:021801, **2004**.

[144] P. O'Keeffe, R. López-Martens, J. Mauritsson, A. Johansson, A. L'Huillier, V. Véniard, R. Taïeb, A. Maquet, and M. Meyer. Polarization effects in two-photon nonresonant ionization of argon with extreme-ultraviolet and infrared femtosecond pulses. *Physical Review A - Atomic, Molecular, and Optical Physics*, 69(5 A):051401–1, **2004**.

[145] M. Meyer, D. Cubaynes, D. Glijer, J. Dardis, P. Hayden, P. Hough, V. Richardson, E. T. Kennedy, J. T. Costello, P. Radcliffe, S. Düsterer, A. Azima, W. B. Li, H. Redlin, J. Feldhaus, R. Taïeb, A. Maquet, A. N. Grum-Grzhimailo, E. V. Gryzlova, and S. I. Strakhova. Polarization control in two-color above-threshold ionization of atomic helium. *Physical Review Letters*, 101:193002, **2008**.

[146] V. Véniard, R. Taïeb, and A. Maquet. Two-color multiphoton ionization of atoms using high-order harmonic radiation. *Physical Review Letters*, 74:4161–4164, **1995**.

[147] V. Véniard, R. Taïeb, and A. Maquet. Phase dependence of (N +1)-color (N >1) ir-uv photoionization of atoms with higher harmonics. *Physical Review A*, 54:721–728, **1996**.

[148] A. Cionga, V. Florescu, A. Maquet, and R. Taïeb. Target dressing effects in laser-assisted x-ray photoionization. *Physical Review A*, 47:1830–1840, **1993**.

[149] P. Lambropoulos. Multiphoton ionization of one-electron atoms with circularly polarized light. *Physical Review Letters*, 29(8):453–455, **1972**.

[150] R. Taïeb, V. Véniard, A. Maquet, N. L. Manakov, and S. I. Marmo. Circular dichroism from unpolarized atoms in multiphoton multicolor ionization. *Physical Review A*, 62:013402, **2000**.

[151] Elletra. FERMI FEL. www.elettra.eu/lightsources/fermi/, (**accessed 22.03.2017**).

[152] FERMI FEL. LDM beamline. www.elettra.trieste.it/lightsources/fermi/fermi-beamlines/ldm/ldmhome-page.html,(**accessed 22.03.2017**).

[153] V. Lyamayev et al. A modular end-station for atomic, molecular, and cluster science at the low density matter beamline of fermi@elettra. *Journal of Physics B: Atomic, Molecular and Optical Physics*, 46(16):164007, **2013**.

[154] M. Zitnik, A. Stanic, K. Bucar, J.G. Lambourne, F. Penent, R. I. Hall, and P. Lablanquie. Lifetimes of n 1 P states in helium. *Journal of Physics B: Atomic, Molecular and Optical Physics*, 36(20):4175–4189, **2003**.

[155] P. Cinquegrana, S. Cleva, A. Demidovich, G. Gaio, R. Ivanov, G. Kurdi, I. Nikolov, P. Sigalotti, and M. B. Danailov. Optical beam transport to a remote location for low jitter pump-probe experiments with a free electron laser. *Physical Review Special Topics - Accelerators and Beams*, 17(4):1–8, **2014**.

[156] K. Kim. Circular polarization with crossed-planar undulators in. *Nuclear Instruments and Methods in Physics Research*, 445:329–332, **2000**.

[157] E. Ferrari et al. Single Shot Polarization Characterization of XUV FEL Pulses from Crossed Polarized Undulators. *Scientific Reports*, 5:13531, **2015**.

[158] O. Kfir, P. Grychtol, E. Turgut, R. Knut, D. Zusin, D. Popmintchev, T. Popmintchev, H. Nembach, J. M. Shaw, A. Fleischer, H. Kapteyn, M. Murnane, and O. Cohen. Generation of bright circularly-polarized extreme ultraviolet high harmonics for magnetic circular dichroism spectroscopy. *Nature Photonics*, 9:99–105, **2015**.

List of Publications

1. T. Mazza, M. Ilchen, **A. J. Rafipoor**, C. Callegari, P. Finetti, O. Plekan, Kevin C. Prince, R. Richter, M. B. Danailov, A. Demidovich, G. De Ninno, C. Grazioli, R. Ivanov, N. Mahne, L. Raimondi, C. Svetina, L. Avaldi, P. Bolognesi, M. Coreno, P. O'Keeffe, M. Di Fraia, M. Devetta, Y. Ovcharenko, Th. Möller, V. Lyamayev, F. Stienkemeier, S. Düsterer, K. Ueda, J. T. Costello, A. K. Kazansky, N. M. Kabachnik, and M. Meyer. Determining the polarization state of an extreme ultraviolet free-electron laser beam using atomic circular dichroism. *Nature communications*, 5:3648, **2014**.

2. T. Mazza, A. Karamatskou, M. Ilchen, S. Bakhtiarzadeh, **A.J. Rafipoor**, P. O'Keeffe, T. J. Kelly, N. Walsh, J. T. Costello, M. Meyer, and R. Santra. Sensitivity of nonlinear photoionization to resonance substructure in collective excitation. *Nature communications*, 6:6799, **2015**.

3. T. Mazza, M. Ilchen, **A. J. Rafipoor**, C. Callegari, P. Finetti, O. Plekan, K. C. Prince, R. Richter, A. Demidovich, C. Grazioli, L. Avaldi, P. Bolognesi, M. Coreno, P. O'Keeffe, M. Di Fraia, M. Devetta, Y. Ovcharenko, V. Lyamayev, S. Düsterer, K. Ueda, J. T. Costello, E. V. Gryzlova, S. I. Strakhova, A. N. Grum-Grzhimailo, A. V. Bozhevolnov, A. K. Kazansky, N. M. Kabachnik, and M. Meyer. Angular distribution and circular dichroism in the twocolour XUV + NIR above-threshold ionization of helium. *Journal of Modern Optics*, 63(4):367-382, **2016**.

4. M. Ilchen, T. Mazza, E. T. Karamatskos, D. Markellos, S. Bakhtiarzadeh, **A. J. Rafipoor**, T. J. Kelly, N. Walsh, J. T. Costello, P. O'Keeffe, N. Gerken, M. Martins, P. Lambropoulos, and M. Meyer. Two-electron processes in multiple ionization under strong soft-x-ray radiation. *Physical Review A - Atomic, Molecular, and Optical Physics*, 94(1):1-6, **2016**.

5. M. Ilchen, N. Douguet, T. Mazza, A. J. Rafipoor, C. Callegari, P. Finetti, O. Plekan, K. C. Prince, A. Demidovich, C. Grazioli, L. Avaldi, P. Bolognesi, M. Coreno, M. Di Fraia, M. Devetta, Y. Ovcharenko, S. Düsterer, K. Ueda, K. Bartschat, A. N. Grum-Grzhimailo, A. V. Bozhevolnov, A. K. Kazansky, N. M. Kabachnik, and M. Meyer.Circular Dichroism in Multiphoton Ionization of Resonantly Excited He^+ Ions. *Physical Review Letters*, 118:013002,,**2017**.

6. H. Duncker, O. Hellmig, A. Wenzlawski, A. Grote, **A. J. Rafipoor**, M. Rafipoor, K. Sengstock and P. Windpassinger. Ultrastable, Zerodur-based optical benches for quantum gas experiments. *Applied Optics*, 53(20):4468-4474, **2014**.

7. **A. J. Rafipoor**, S. Bakhtiarzadeh, M. Meyer, D. Cubaynes, E. Heinecke, S. Kröger, R. Müller and P. Zimmermann. Magnetic dichroism in photoemission across atomic autoionizing resonance. (To be submitted).

Acknowldegments

First and for most, I want to thank my supervisor and my boss, Dr. Michael Meyer, for giving me the invaluable opportunity to expand my knowledge and capabilities by working in the SQS-group at European XFEL GmbH. I would like to thank Dr. Michael Meyer for teaching me and guiding me through the great field of atomic and molecular physics and being always available for all kind questions and sharing his outstanding expertise. I am very lucky and grateful for all opportunities he presented to me. I am proud of having been his PhD student. I would like to thank Prof. Dr. Klaus Sengstock for agreeing to be my University supervisor. I am exceedingly grateful for the generous time given to discuss my research activities and for the insightful comments and advice.

A special thanks goes to Dr. Markus Ilchen for his advice both at the scientific as well as the personal level. I'm grateful for the time he spent helping me to discuss my thesis, even during his busy time. He was always available for answering all my questions. I would like to thank Dr. Tommaso Mazza for his strong support during my PhD education. I am grateful for his advice, discussion and all things he taught me. I also want to thank Dr. Alberto De Fanis for the time he spent to answer my questions, especially during the beamtimes.

I would like to thank the SFB 925 graduate school program for funding the PhD project I was involved in and for providing me with the necessary travel support, which has allowed me to participate in the various X-ray experiments. The financial support has allowed me to stay in Germany and enjoy the german culture. I also would like to thank Mrs. Janina Dahms for the support and for organising all the workshops and conferences within the SFB 925 program.

I want to express my gratitude to my friends and colleagues Dr. Pouneh Saffari, Alexander Achner, Masoud Mehrjoo, Tadesse Abebaw Assefa, Sadegh Bakhtiarzadeh, Michael Diez for helping me during my studies and for the nice time we spend together.

On the personal side, I have been greatly supported by my parents, brothers and my sister always having an open ear for me and always taking so much care. I am deeply thankful for having them. Finally, I would like to thank my great teacher Dr. Hojabr and also my best friends Farbod, Andre, Naily and Stefan for their continuous support in private life and off course my girlfriend Shirin for her patience when the time was little.

Eidesstattliche Erklärung

Hiermit erkläre ich an Eides statt, dass ich die vorliegende Dissertationsschrift selbst verfasst und keine anderen als die angegebenen Quellen und Hilfsmittel benutzt habe. Teile dieser Arbeit wurden in den Referenzen [26,39,47] veröffentlicht.

_____

Ort, Datum

_____

Amir Jones Rafipoor